January 2020

Modeling and Control of Renewable Energy in Grids and Microgrids

Yin Li
University of South Florida

Modeling and Control of Renewable Energy in Grids and Microgrids

by

Yin Li

A dissertation submitted in partial fulfillment
of the requirements for the degree of
Doctor of Philosophy
Department of Electrical Engineering
College of Engineering
University of South Florida

Major Professor: Lingling Fan, Ph.D.
Zhixin Miao, Ph.D.
Elias Stefanakos, Ph.D.
Kaiqi Xiong, Ph.D.
Qiong Zhang, Ph.D.

Date of Approval:
December 4, 2019

Keywords: Stability Analysis, Coordinate Control, EMT Simulations, Hardware Testbed, CHIL Testbeds

Dedication

To my wife and my parents.

Acknowledgments

First of all, I would like to express my deepest gratitude to my advisor Dr. Lingling Fan for her help, guidance, and support during my Ph.D. studies. Dr. Fan did not only guide me on research but also gave me advice on teaching. She used her meticulous help and support to shape me to become a qualified Ph.D. candidate.

I would also like to appreciate Dr. Zhixin Miao who gave me a good opportunity to teach an undergraduate-level course. This experience improved my teaching skills significantly. He also provided an excellent working environment which includes kinds of research devices and applications to practice my hands-on skills.

Secondly, I appreciate the rest of my committee members: Dr. Lee Stefanakos, Dr. Kaiqi Xiong and Dr. Qiong Zhang for their encouragement and helpful comments.

I would like to thank my recent and former colleagues from the smart grid power system lab, in particular: Dr. Lakshan Piyasinghe, Dr. Javad Khazaei, Dr. Hossein Ghassempour, Dr. Anas Almunif, Yangkun Xu, Minyue Ma, Yi Zhou, Ibrahim Alsaleh, Rabi Kar, Li Bao, Miao Zhang, Zhengyu Wang, Abdullah Alassaf for all the discussions, help, and enjoyable time I spent with them.

Last but not least, I want to thank my father, my mother, and my wife for all encouragement, support, and love they provided from the beginning.

Table of Contents

List of Tables

List of Figures

Abstract

To save the non-renewable resources and reduce pollution emissions, the integration of renewable energy sources (RES) into the main grid is increasing very fast. However, power systems experience more stability issues that are caused by the higher penetration of RES. The main objectives of this dissertation are to 1-investigate these stability issues using linear analysis, EMT simulation results, and experiment results; 2-provide the suitable solutions with the evaluations. The research results will be presented into two parts based on two modeling approaches. In the first part, RES units are normally modeled as an aggregated power source for the investigation because they are installed in the same farm and have the same structure and parameters. Hence, the investigations in this part are based on the single-inverter aggregated modeling of RES. In the second part, RES units and/or battery energy storage system (BESS) units are integrated into the same microgrid but they can be different types and have different parameters. Hence, each unit needs to be modeled individually. In other words, multi-inverter based modeling is used to investigate the stability issues in microgrids. In each part, both analytical model and testbed are built using the same corresponding modeling approach. Analytical models are built in dq frame to produce the linear analysis while the testbeds are built using EMT software or hardware to provide more practical results for validations.

The first part of this dissertation investigates stability issues that happened in wind farms connected to the conventional grid using the single-inverter aggregating modeling. Due to the different reasons, the stability issues in this part are also divided into two categories, weak grid, and series compensated networks. The investigations on stability issues in the weak grid are started by two real-world events. In 2016, a subsynchronous oscillation (SSO) was observed in Type-4 wind farms connected to the weak grid in Northwestern China. This subsynchronous oscillation (SSO) also caused the torsional interaction between wind farms and remote thermal power plants. However,

the previous instability events in the Type-4 wind farms were normally reported with the low-frequency oscillations such as the event in Texas in 2012. To explore the critical factor behind this difference, a single-inverter aggregated analytical model is built based on Type-4 wind connected to the weak grid. According to the linear analysis, this difference in the oscillation frequency is caused by the dynamics of phase-locked-loop (PLL). This finding is validated using an EMT testbed which is built in MATLAB/SimPowerSystems. Meanwhile, the torsional interaction with the remote synchronous generator is demonstrated using this testbed. To solve the stability issues caused by the weak grid, stability control with two strategies is implemented in two aggregated analytical models. The eigenvalue analysis is used to evaluate its performance. Then, a Type-3 EMT testbed and a Type-4 EMT testbed are built to validate the analytical results. Furthermore, the stability control is also implemented in an FPGA-based hardware testbed. The experiment results show the excellent enhancement of stability.

In the series compensated networks, stability issues are investigated by replicating three real-world subsynchronous resonance (SSR) events. From August to October 2017, the Electric Reliability Council of Texas (ERCOT) reported three SSR events in the same transmission system which consists of six Type-3 wind plants and a series compensated line. These events were excited by the line outage but they had different consequences. To provide a reasonable explanation, this dissertation replicates these three SSR events using the EMT testbed built based on the real system. The challenge of replication is the limited information of system parameters. The fragmented information is collected and combined from different public project reports and websites. To estimate some parameters which are not found such as the number of online wind turbines and wind speed, the sensitivity analysis is conducted using both simulation results and analytical results. Note that these results are generated based on the single-inverter aggregated modeling of Type-3 wind. Finally, improved SSR control was implemented in the EMT testbed to mitigate SSR.

The second part of this dissertation discusses the stability issues in microgrids. Different than the conventional grid, the investigations on microgrid need to consider not only the characteristics of each distributed generation resource (DER) but also the coordinate control among DERs. In this part, two coordinate controls, voltage-current (V-I) droop and consensus control, will be

investigated under both grid-connected mode and autonomous mode. V-I droop control was proposed in 2015 to enhance the accuracy of reactive power sharing in the microgrid. However, our simulation results showed that the oscillation issues happened in a microgrid with V-I droop when small values were selected for droop coefficients. To investigate the effects of droop coefficients, a two-inverter based analytical model is derived with the multi-input multi-output (MIMO) matrix of transmission networks. The linear analysis is carried out to identify the root causes of oscillations under both grid-connected mode and autonomous mode. Analytical results are validated using the detailed testbed which is built in MATLAB/SimPowerSystems. In the testbed, two DERs are modeled separately as well. As the second coordinate control investigated in this dissertation, the consensus control can maximize the efficiency of a microgrid by synchronizing performances of all parallel BESS. Meanwhile, it only requires each BESS to share the limited information with its neighboring BESS. To evaluate the performance of the consensus control, a multi-inverter based analytical model is derived based on the grid-connected microgrid with three BESS. Furthermore, a controller-hardware-in-the-loop (CHIL) testbed is built to emulate the microgrid which has three BESS and is integrated into the IEEE 9-bus system. The entire circuit is simulated by a real-time simulator while three BESS are controlled by three external FPGA-based controllers. This CHIL testbed provides a more realistic environment to evaluate the consensus control because of the full dynamics of microgrid and the large-scale power system.

This dissertation has led to four published journal papers and one working paper.

Chapter 1: Overview

1.1 General Introduction

When they bring benefits to our life, RES also bring more challenges to our power systems because of their less inertia and remote locations. Compared with the conventional electrical energy sources such as the synchronous generators, RES have much less or no rotational inertia. It causes that the power system is more sensitive to perturbations when the penetration of renewable energy becomes higher. The second challenge is from remote locations. RES units are normally installed in remote areas to maximize efficiency so they have to deliver the energy through the long transmission line which is one reason to cause the weak grid. Although stability issues in RES connected to the conventional grid have been studied for a long time, the number of reported instability events in the real world is even increased instead of reduced. Furthermore, some new phenomena in recent events cannot be explained by the existing studies. Hence, more stability analysis need to be conducted to provide suitable explanations.

RES and BESS are also widely used in the microgrid. Compared with the conventional grid, the microgrid does not need to face the challenge of the weak grid. However, investigations on microgrid have to consider the stability issues under two operating modes, grid-connected mode, and autonomous mode. Due to less system inertia, the stability issues in the microgrid are normally caused by perturbations of power or voltage. On the other hand, they also can be caused by the poor design of coordinate control which is used to collaborate DERs [1]. To improve the reliability and efficiency of microgrids, more advanced coordinate controls are proposed so more evaluations on their performances need to be conducted to avoid poor design.

In the following sections, a more detailed background, literature review, and contributions of this dissertation will be introduced for both conventional grid and microgrids.

1.2 Single-inverter Aggregated Modeling of RES

Because of the same structure and operating condition, RES units in the same farm can be aggregated as one. This technology is widely used by majority papers to investigate the dynamics of RES units in the same farm connected to the grid [2–5]. Although the different locations of RES units in the same farm may have different effects on the whole system dynamics, these different effects are normally slight and ignored. [6] already used the simulation results to prove that the simplified aggregated model has similar dynamic characteristics as a complex detailed model. Therefore, the investigations on the farms of RES in the weak grid and the series compensated networks will be conducted using the technology of single-inverter aggregated modeling.

1.2.1 Modeling and Control of RES in Weak Grid

The farms of RES are normally located in remote areas so the long transmission lines are required to transfer the power to the main grid. Based on $SCR = \frac{1}{X_g P}$, both high penetration P and lone transmission line X_g can cause the weak grid. SCR is the acronym of the short-circuit ratio. The value of SCR determines the strength of the grid. When $SCR < 3$, the grid can be considered as the weak grid. Hence, when they have to transfer the power to the grid with $SCR < 3$, RES may experience instabilities which are caused by the weak grid.

1.2.1.1 Stability Issues in Weak Grid

In previous reports and existing studies [7–10], the low-frequency oscillations (less than 10 Hz) were normally observed in the instability events which were caused by Type-4 wind connected to the weak grid. For example, EROCT reported a $3-4$ Hz oscillation in Texas Type-4 wind farms which were connected to the weak grid [7]. Fig. 1.1 from [7] shows the topology of the transmission systems in Texas and the recorded voltage dynamics with the low-frequency oscillation.

However, in 2014, a sub-synchronous oscillation was observed in Type-4 wind connected to the weak grid [5]. It happened in Northwestern China and the related transmission system is shown in Fig. 1.2.

Figure: Competitive Renewable Energy Zone (CREZ) transmission system

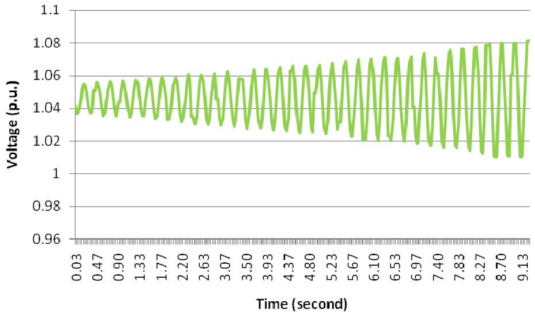

Figure: Recorded voltage oscillations

Figure 1.1: Low-frequency oscillation was observed in Texas transmission system. Two figures are from [7]. Permission is included in Appendix A.

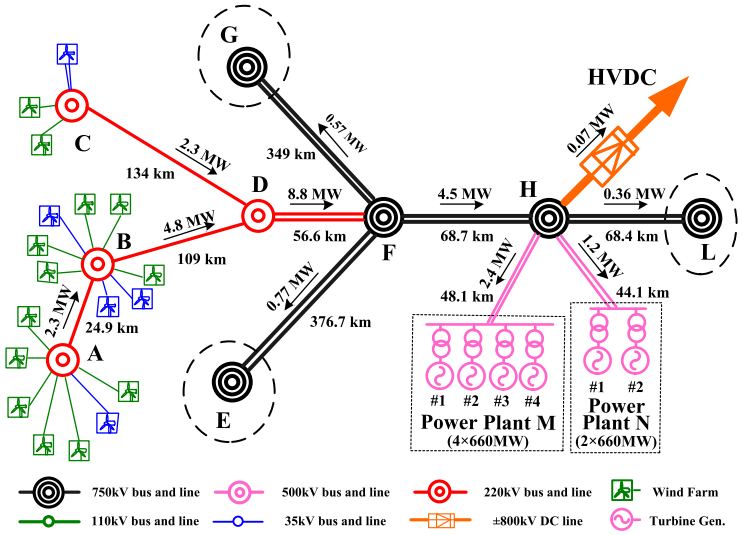

Figure 1.2: The practical system suffered from unstable SSO in China. This figure is from [5]. Permission is included in Appendix A.

In the real system, multiple 1.5 MW direct-drive PMSG-based wind turbines are installed at Bus **A** and **B**. Because the wind farms are far away from the main grid, the long transmission lines are used to transfer the power. At the end of 2014, the installed wind power reached 31% of the short-circuit capacities such that these wind farms suffered a very weak grid ($SCR = 1.3$) [5]. Consequently, a subsynchronous oscillation (SSO) event happened on July 1st, 2015. The frequency of SSO varied from 27 Hz to 33 Hz shown in Fig. 1.3. Moreover, this SSO caused the torsional

interactions with the remote thermal power plants **M** and **N** because its frequency matched one torsional mode of the synchronous machine in those thermal power plants shown in Fig. 1.4. It was the first time to observe the SSO in Type-4 wind connected to the weak grid.

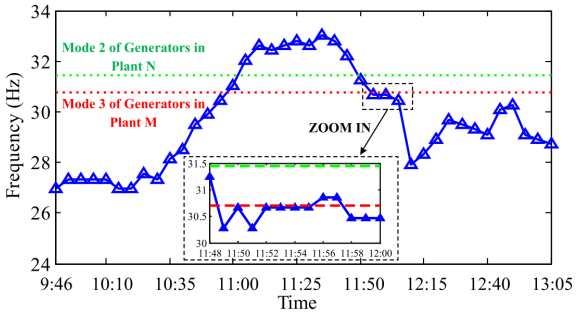

Figure 1.3: Variation of the SSI frequency and associated torsional frequencies. This figure is from [5]. Permission is included in Appendix A.

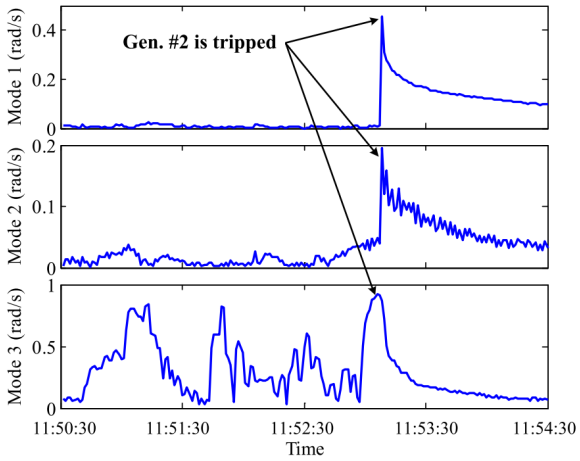

Figure 1.4: Torsional speed of models 1-3 of unit #2 in Plant M. This figure is from [5]. Permission is included in Appendix A.

1.2.1.2 Motivation and Existing Studies

Inspired by those real-world events in Type-4 wind, this dissertation will figure out the critical factor which causes different oscillation frequencies. Many papers already studied the effects of control modes of Type-4 wind on the dynamics of oscillation frequency [4, 5, 8, 11, 12]. In the literature, there are two control modes which are normally employed by Type-4 wind, power control

mode and dc-link voltage control mode. The control mode is determined by the controlled variable on the d-axis of the outer loop in the grid-side converter (GSC). If the controlled variable is real power, the control mode is named as the power control mode. If the dc-link voltage of GSC is controlled, it is named as the dc-link voltage control mode. When either the active power or the dc-link voltage is controlled by GSC, another one is controlled by the machine-side converter (MSC) in Type-4 wind.

In [8, 11, 12], research results only show the low-frequency oscillation in Type-4 wind with the power control mode. However, [4, 5] show the subsynchronous oscillation in Type-4 wind under the dc-link voltage control mode. [4] adopts frequency-domain analysis and demonstrates subsynchronous frequency mode that can cause torsional interaction with a synchronous generator. [5] carries out impedance-frequency curves to identify an unstable subsynchronous-frequency mode at 30.76 Hz. Then, the participation factor analysis indicates that the subsynchronous-frequency mode is related to the dc-link capacitor dynamics. Based on the eigenvalue analysis in this dissertation, Type-4 wind with either control mode has both oscillation modes but which oscillation mode is dominant depends on the dynamics of a phase-locked loop (PLL). Both control modes will be investigated using single-inverter aggregated models. However, the dc-link voltage control mode is employed by Type-4 wind in that China SSR event [5] so the models with dc-link voltage control mode will be focused on to analyze the effect of PLL dynamics on oscillation modes of Type-4 wind in the weak grid.

PLL is always a necessary part of inverter-based resources (IBRs) such as Type-4 wind, Type-3 wind, PV, and BESS. With eigenvalue analysis, [13] shows that the bandwidth of PLL has a significant effect on the oscillation mode of Type-4 wind. The lower bandwidth makes the low-frequency mode dominant while the higher bandwidth makes the subsynchronous-frequency mode dominant. The PLL adopted in [13] is a synchronous reference frame based PLL (SRF-PLL). As the second-order application, SRF-PLL is most popularly adopted by many recent papers to investigate the dynamics of RES and grid integration networks [8, 9, 14–16].

On the other hand, PLL has many different structures. In 2001, [17] used a lead/lag controller to replace the PI controller in SRF-PLL to provide better filtering performance. In 2003, [18] proposed

a PLL that controls the voltage magnitude, phase angle, and frequency by three different blocks respectively. It generates the second harmonics to cancel the harmonics of the voltage. In 2006, [19] used the quadrature-signal generator (QSG) in a double second-order generalized integrator PLL (DSOGI-PLL) to filter the second order harmonics. [20] used a decoupling network in PLL to cancel the voltage harmonics. It is named as the decoupled double synchronous reference frame (DDSRF-PLL). In 2007, [21] utilized two band-pass filters in a software-based PLL to filter the high-order harmonics without sacrificing the detecting speed. Although all the above PLLs have more advanced structures, they have similar dynamics with SRF-PLL because they are designed based on it. Therefore, my studies on the dynamics of PLL mainly focus on SRF-PLL. For comparison, the lead/lag PLL is also modeled and investigated.

Although [13] already proved that the bandwidth of PLL could influence the oscillation modes, this dissertation extends that work by providing more detailed linear analysis, validation of EMT testbeds, and demonstration of torsional interactions. Besides the eigenvalue loci, the linear analysis also employs the participation factor to determine which state is most related to the dominant mode. The EMT testbed is built based on Type-4 wind connected to the weak grid and a synchronous generator integrated at the grid side. Hence, it is not only used to validate the analytical results but also used to demonstrate the torsional interaction. Furthermore, because different values are selected for the damping of PLL, it is also identified that the damping of PLL plays an important role in the oscillation modes as well.

1.2.1.3 Stability Control

As one objective of this dissertation, a suitable solution is provided to improve the stability in RES in the weak grid. In the literature, kinds of strategies have been proposed and they can be classified into four categories. The first category is the physical device such as the shunt reactive power compensation [22]. The second category deals with the control mode of inverters of RES. As aforementioned, Type-4 wind has two kinds of control modes, power control mode and dc-link voltage control mode. According to studies on the grid dynamics [23, 24], the large size Type-4 wind usually uses the power control model to improve the stability. The third category is to design

the inverter control to emulate a synchronous generator by abandoning the vector control and PLL [25, 26].

The fourth category enhances the structure of vector control in RES [27,28]. [27] found that the deviation of the converter current on the $d-$axis is linear with the angle error while the deviation of the current on $q-$axis is linear with the deviation of PCC voltage. The angle error is between the measured PCC voltage and the PLL output. Hence, [27] adds two compensated modules to modulate the PLL angle and PCC voltage respectively. The inputs are the deviations of the converter currents on the $d-$axis and $q-$axis. The system with the modified vector control can operate at SCR = 1 when power reaches 60% of the nominal level. [28] found that the instability in VSC is caused by the outer control loop because of nonlinearity. Hence, [28] added a decoupling part in the outer loop to overcome this nonlinearity. The gain scheduling technique is used in the addition part. Gains need to be calculated for different operating conditions. This method can achieve maximum power output at 89% of the nominal level when $SCR = 1$.

As the fourth category, stability control is proposed to solve the stability issues in the weak grid. [29] shows that the instability in the weak grid is caused by the coupling between output power and PCC voltage. Hence, the stability control is designed to suppress this coupling relation using two approaches, voltage-based and current-based. Each approach is evaluated using two single-inverter aggregated analytical models which are with power control mode and dc-link voltage control mode respectively. Compared with methods in [27, 28], the stability control does not only have the simple control strategy but also enhances VSC to transfer more power when $SCR = 1$. Based on the analytical results, 1.0 pu of power can be delivered for SCR = 1 when the stability control is implemented in a VSC under the power control mode. Under dc-link voltage control mode, 0.97 pu power can be delivered by VSCs .

To validate the linear analysis, a Type-3 wind testbed and a Type-4 wind testbed are built in MATLAB/SimPowerSystems. In Type-3 wind testbed, the majority of power is delivered by rotor-side-converter (RSC) which employs the power control mode so the stability control in power control mode is applied to Type-3 wind. The Type-4 wind is dependent on the GSC which uses dc-link voltage control mode so the stability control in dc-link voltage control mode is applied to the

Type-4 wind. Furthermore, an FPGA-based hardware testbed is built up to test stability control. Its excellent performance is validated by the experimental results as well.

1.2.2 Modeling and Control of RES in Series Compensated Networks

Due to the SCR equation, the large reactance of the transmission line is the main factor to cause the weak grid. The reactance can be reduced effectively by adding a capacitor to the transmission line in series. The transmission system with this line is named as the series compensated network. This method is widely used in real-world systems to improve the strength of the grid.

However, the series compensated line also brings another type of stability issue which is caused by the LC resonance. Although the recent publication [30] proves that Type-4 wind is not immune to the series compensated networks, this type of stability issue in Type-3 wind is mostly reported and widely studied [31–35].

1.2.2.1 Stability Issues in Series Compensated Networks

Stability issues in series compensated networks are normally represented by the subsynchronous resonance (SSR). For example, three SSR events were recorded in Texas by the Electric Reliability Council of Texas (ERCOT) from August to October in 2017. Descriptions and records of these events were reported in [36]. These three events happened in the same 345 kV transmission system. Six wind plants are integrated at three substations: Cenizo, Del Sol, and Pomelo. A series compensation line is employed to connect the Cenizo substation and Del Sol substation. Two end substations, San Miguel and N Edinburg, are connected to the main grid. The voltage and current of each event were recorded and presented in [36].

According to the report [36], these Type-3 wind farms were identified with SSR risk previously. Indeed, the SSR events did not occur at the beginning. However, with more wind turbines online, SSR happened more easily after transmission line outages. In each event, SSR was excited by Type-3 wind farms radially connected to the series compensated line after one transmission line tripped. The tripping sequence in each event is listed as follows. On August 24th, Del Sol - Pomelo line was tripped in Event 1. This line outage left Plants 3 & 4 being radially connected to the Cenizo-Del

Sol series compensated line. 25.6 Hz SSR was observed in instantaneous currents in *abc*-frame until Plants 3 and 4 were tripped by the protection devices. The currents and the corresponding frequency spectrum are shown in Fig. 3.13a. On September 27th, Lobo - Cenizo line was tripped in Event 2. This line outage left Plants 1 & 2 being radially connected to the Cenizo-Del Sol series compensated line. 22.5 Hz SSR was observed which led to the tripping of wind plants 1 & 2. The currents and the corresponding frequency spectrum are shown in Fig. 3.13b. On October 27th, Del Sol - Pomelo line was tripped in Event 3. 26.5 Hz SSR was observed. This event did not trigger the protection device and Plants 3 &4 were not tripped. The currents and the corresponding frequency spectrum are shown in Fig. 3.13c.

After the line tripped, SSR with three different frequencies happened in these three events respectively. On the other hand, SSR in Event 1 and Event 2 were severe enough being detected by the protection device while SSR in Event 3 was too slight to trigger the protection device. It is also noticed that in Event 3, more wind power was generated compared to that in another two events.

1.2.2.2 Motivation and Existing Studies

These three events were caused by the same reason (line tripped) but they had the difference consequences (SSR magnitude and frequency). It is understandable that for Event 1 and Event 2, the difference in SSR frequency was because of the different equivalent compensation networks of resulting systems. However, Event 1 and Event 3 also had different SSR frequencies even if they had the same equivalent compensation network after the same line tripped. Furthermore, there was more power transferred through the series compensated line in Event 3 but there was no wind plant tripped.

As aforementioned, SSR events in Type-3 wind have been studied by many publications [33–35, 37–43]. They already found that the dynamics of SSR can be affected by different critical factors such as the compensation level, grid strength, torsional interaction, wind speed, and control systems. However, a reasonable explanation of the different consequences in these three events could not be carried out even if the public report, *South Texas SSR*, had been posted by ERCOT

for eight months. To provide a reasonable explanation, this dissertation will investigate these three SSR events by replicating them.

Building a detailed EMT testbed is a widely approach to investigate the real SSR events in Type-3 wind. However, the testbeds built by existing publications cannot be used to replicate above SSR events because the detailed information of those testbeds is not given. For example, [37, 39–41, 43] investigated SSCI in Type-3 wind plants using the EMT simulations but they did not give the detailed information such as topologies of corresponding real systems, line impedance, and parameters of wind turbines. Meanwhile, none of those testbeds are built based on the region of the real ERCOT system studied in [36]. For example, [42] gave the impedance of transmission lines and transformers but it focused on the different portions of the ERCOT transmission system than the portion in [36]; [38] compared the real records and EMT simulation results but it used a simple and non-proprietary testbed. Hence, a new and particular EMT testbed with the accurate information needs to be built up to replicate above three recent SSR events.

1.2.2.3 Challenges on Replication

The challenges for the replication are the limited information of the transmission system and the operating conditions of three SSR events. That report from ERCOT [36] provided the topology of the system but it did not provide other related information such as the parameters. Based on the topology of the real system, it can be determined that the testbed should focus on the part of the ERCOT system from the San Miguel to N. Edinburg and the six integrated wind plants. The system topology can be found in [36]. Other parts of ERCOT system are simplified as voltage sources behind San Miguel 345 kV substation and behind N. Ediburg 345 kV substation.

After the system structure is determined, the accurate parameters of the real system need to be found out to configure the testbed. The fragmented information about this real system is collected from different public project reports and websites. By combining the collected information, lengths of transmission lines, compensation level, and the names of wind farms are determined. Then, the type of wind turbines and the capacity of the wind plants are found by searching their names in the public database. The detailed information of wind turbines such as the control system and

parameters is confidential to wind manufacturers so the 1.5 MW doubly-fed induction generator (DFIG) demo in MATLAB/Simpowersystem is adopted in the EMT testbed.

Although parameters have been found, the operating conditions such as the number of online wind turbines and the wind speed are still unknown. In this dissertation, these two factors are determined by fine-tuning based on their sensitivity analysis. The sensitivity analysis is conducted using eigenvalue analysis and EMT simulation results. Using the EMT testbed with accurate information, the replication results are generated and match the real records in [36] very well. It is also found that wind speed plays the most important role in the differences among three SSR events.

1.2.2.4 SSR Control

To mitigate SSR in the above events, a practical solution, SSR control, is provided. In the literature, there are two categories of existing methods to solve the stability issues which are caused by series compensation networks. The first category is installing additional FACTS devices at PCC bus to regulate PCC voltage [44, 45] while the second category is improving control strategies of RSC or GSC in Type-3 wind [46, 47]. Compared with the former one, the latter category saves more costs and time on infrastructure.

SSR control belongs to the second category and was proposed in 2012 [46]. It is a kind of supplementary control and should be implemented in GSC of Type-3 wind. In this dissertation, SSR control is improved and implemented in the above replication testbed to mitigate SSR. The improved SSR control utilizes the current through the series compensated line to mitigate SSR. This current signal is a more practical approach for the real-world compared with the voltage dropped on the series capacitor. All of the research results on the replication and SSR mitigation will be presented in Chapter 3.

1.3 Multi-inverter Modeling of RES and BESS in Microgrid

RES are also widely used in the microgrid. Compared with the conventional grid, the microgrid has a smaller size such as a lower voltage level and lower power level. The voltage level of the

microgrid is typically from 400 V to 69 kV [48] and the power level normally varies from hundreds of kilowatts to tens of Megawatts [49]. Furthermore, microgrid has higher uncertainty because there are more uncertain events or disturbances that happened in the microgrid [50]. Meanwhile, microgrid has less capability to handle the disturbance because it has less system inertia. A small disturbance in the microgrid can lead to the relatively large deviation of the voltage and frequency [1]. To increase the reliability and efficiency of microgrid, an upper-level control (coordinate control) is normally utilized to collaborate DERs. To analyze the dynamics of coordinate controls, DERs in microgrid cannot be modeled as an aggregated voltage source even if they have the same structure and parameters. Hence, this dissertation will use the technology of multi-inverter modeling to investigate microgrids with two coordinate controls, V-I droop and consensus control.

1.3.1 Stability Issues in Microgrid

The recently published survey paper [1] claims that stability issues in the microgrid are different than the conventional grid. It also classifies the stability issues in microgrids into two categories. The first category is related to the power supply and balance. The stability of microgrid requires to maintain the balance between the generated power and demand power. When the balance is terminated by loss of DER, hitting limits of DER, ineffective power sharing, and large load tripping, the microgrid will suffer the instability [51]. The second category is related to the control systems of the equipments such as the inadequate control schemes and/or the poor tuning of the controllers [1]. This dissertation will focus on the second category of stability issues in a microgrid with droop control.

1.3.2 Existing Studies and V-I Droop

As a decentralized control scheme, the droop control is widely used to collaborate multiple DERs in microgrids without the intercommunication among DERs [52]. Based on the different droop relations, droop controls provide different approaches to achieve power sharing among DERs. Based on the analysis, many published papers [52–57] already proved that the poor selection of the droop coefficient is the challenge to the stability of microgrid with droop control.

However, the stability issue in a microgrid with V-I droop has not been identified and studied. As a relative new droop control, V-I droop was proposed in [53] in 2015. It has fast dynamics and accurate power sharing. Different than the conventional droop control using $\Delta P - \Delta f$ and $\Delta Q - \Delta V$, V-I droop utilizes droop relations between voltages and currents on dq-axis to adjust the output voltage references of DER. Relations can be expressed by the following equations, $E_d^* = E_0 - mi_{Ld}$ and $E_q^* = 0 - ni_{Lq}$. In a microgrid with V-I droops, the PLL is not required for each DER. The real and reactive power sharing is inversely proportional to the ratio of droop coefficients. Although [53] mentioned that small droop coefficients may lead to inaccurate power sharing, the oscillation issue is not observed and investigated yet. In this dissertation, the stability issues in the microgrid with V-I droops will be investigated. First, the eigenvalue analysis is carried out from the derived analytical model which is designed based on the microgrid with V-I droops. Note that eigenvalue analysis is a popular method used to investigate the stability issues in the microgrid with multiple DERs [52, 54–56, 58, 59]. Then, the analytical results are validated by the simulation results from the detailed testbed which is built in MATLAB/SimPowerSystems.

1.3.3 Consensus Control for BESS

As another kind of DER, the battery energy storage system (BESS) provides the user with dispatch capability of the RES such as PV and wind [60]. To balance the power and energy in microgrids, BESS stores energy when the generation is higher than the demand. On the other hand, it supports the system when the demand is higher than the generation. BESS also can improve the reliability of microgrid on the sudden disturbances [60, 61]. However, the disadvantage of BESS is its high costs on the device, maintenance, and depreciation [60]. Compared with the innovations of the materials, the advanced control strategy can be achieved more easily to reduce the cost of depreciation.

The depreciation of the battery is mainly related to its state of health (SoH) while SoH is influenced by the times of charging and discharging. [62] provided a consensus control to synchronize the power and energy of multiple BESS in the microgrid. It minimizes the times of charging or discharging of any individual battery. The consensus control does not only reduce the depreciation

rate of batteries effectively but also makes the microgrid maintain the high efficiency [62]. To evaluate the performance of the consensus control, a multi-inverter based analytical model is derived based on the grid-connected microgrid with three BESS. In addition, a controller-hardware-in-the-loop (CHIL) testbed is built to test the consensus control in a more practical and complex system. In the current CHIL testbed, a microgrid with three BESS is integrated at Bus 9 of the IEEE 9-bus system. Besides the simulation results, the detailed configuration of the CHIL testbed will be introduced in Chapter 4.

1.4 Tools for Stability Analysis of RES and BESS

As an important tool, the analytical model is widely used to study the dynamics of RES and BESS in the conventional grid and microgrids [8,63–67]. In such models, inverters are considered as the voltage sources with the dynamics of vector controls but the switching dynamics are omitted. They are derived in the dq frame and the flat run is required to generate the linear analysis. In this dissertation, the corresponding analytical models are derived to investigate specific stability issues. Analytical models for Type-4 wind and Type-3 wind are proposed in [8, 63] while [68] provides the derived procedures and flat run for Type-4 wind. Analytical models for microgrids with multiple DERs are derived in Chapter 4. Based on analytical models, the eigenvalue analysis can be generated to analyze the dynamics of systems under different conditions. However, the analytical model is a simplified model and only includes the essential dynamics of the studied system. Hence, these analytical results need to be validated by more practical models including full dynamics.

EMT testbed is another tool to investigate the stability issues of RES. Compared with the analytical model, the EMT testbed includes full dynamics such as electromechanical dynamics, dynamics of controllers for the machine, limits for the protection, and natural factors like wind speed and irradiance. Hence, the EMT testbed is not only used to validate the analytical results but also used to demonstrate more complex events and replicate the real-world events. The popular simulation applications for EMT testbeds are MATLAB/SimPowerSystems and PSCAD. Many examples of EMT testbeds with realistic parameters can be found from their database. In

this dissertation, EMT testbeds are built in MATLAB/SimPowerSystems and developed from its examples, especially wind modules. After each part of linear analysis, the EMT simulation results will be plotted for validations and demonstrations.

The third tool is the testbed which is built with laboratory-size devices. The objectives behind the hardware testbeds are not only to validate the analytical results but also to provide a more practical approach to test the proposed controls in the Mega Watt (MW) systems at a mini-scale. This is also a standard process to investigate the high power transmission and distribution systems. In this dissertation, there are two types of hardware testbeds configured, the pure laboratory-size hardware testbed and the controller-hardware-in-the-loop (CHIL) testbed. The pure hardware testbed is built based on the FPGA-based controller from National Instrument (NI) and employs the laboratory-size devices. Compared with the pure hardware testbed, the CHIL testbed provides a safer and more flexible testbed [69, 70]. It consists of a real-time simulator (RT-LAB) and multiple FPGA-based controllers. The pure hardware testbed is used to test stability control in RES connected to the weak grid while the CHIL testbed is used to test consensus control in the microgrid with three BESS.

1.5 Outline of Dissertation

After the introduction, the rest of this dissertation is organized as follows.

Chapter 2 focuses on the stability issues in RES connected to the weak grid. First, the single-inverter aggregated analytical model is used to analyze the effect of PLL dynamics on the oscillation frequency of Type-4 wind in the weak grid. Then, the stability control is proposed and implemented in analytical models to solve the stability issues. Its performance is evaluated using the eigenvalue analysis. Next, the corresponding EMT testbeds are built to validate all of the analytical results. Finally, a hardware testbed is built to test the stability control using experimental results.

Chapter 3 replicated three real-world SSR events in Type-3 wind connected to the series compensated network. To configure an EMT testbed, this chapter introduces how to collect the accurate parameters and generates sensitivity analysis on two unknown factors. Then, the EMT simulation

results are plotted to match the real-world records. Finally, a practical SSR control is implemented in this EMT testbed to mitigate SSR.

Chapter 4 discusses two coordinate controls for the microgrid with multiple DERs. First, a two-inverter analytical model is derived to analyze the effects of droop coefficients on the stability of microgrid with V-I droops. The linear analysis is validated by an EMT testbed which is a grid-connected microgrid with two DERs. After V-I droop, the consensus control is evaluated using a three-BESS analytical model and a CHIL testbed. Both model and testbed have the same structure of microgrid but they have different grids. The grid in the analytical model is modeled as an ideal voltage source while the grid in CHIL testbed is IEEE 9-bus system.

Chapter 5 concludes all my research results for RES in the conventional grid and microgrids. It also presents the future work of my research topics.

Chapter 2: Single-inverter Aggregated Modeling of RES in Weak Grid

2.1 Introduction

This chapter [1] presents the modeling and stability analysis on the farm of RES connected to the weak grid. Due to the same characteristics, these RES units in the same farm are usually modeled as an aggregated single inverter for analysis. In other words, the stability of the entire RES farm in the weak grid is based on the interactions between the single RES unit with the grid.

My research results on this topic focus on the weak grid instability events in China and Texas. Two control modes of Type-4 wind will be introduced first. Then, the dynamics of PLL are analyzed on the different types and different bandwidth. Both eigenvalue loci and participation factors are conducted to confirm the finding that the oscillation mode of Type-4 wind in the weak grid is mainly dependent on the dynamics of PLL in [13]. Next, both control modes will be evaluated with the stability control using the analytical models. Furthermore, several EMT testbeds and an FPGA-based hardware testbed are built to validate the corresponding analytical results.

2.2 Control Modes of Type-4 Wind

2.2.1 Topology of Type-4 Wind

The full topology of the SG-based wind turbine is shown in Fig. 2.1. Although there are actually more than one wind turbines in the same wind farm, they can be aggregated as one wind turbine with the same per-unit values and control parameters. In Type-4 wind, there are two back-to-back voltage-source converters (VSCs) employed. One is named as the grid-side converter (GSC) which is connected to the point of common coupling (PCC) bus directly. Another one is named as

[1] The majority of this chapter was published in IEEE Transactions on Power Systems [68] and IEEE Transactions on Sustainable Energy [71], 2019. Permissions are included in Appendix A. Section 2.6 was submitted to IEEE Transactions on Sustainable Energy [72], 2019

the rotor-side converter (RSC) or machine-side converter (MSC) which is connected to the wind turbine. Between two converters, there is a DC-link capacitor which is used to regulate the DC voltage. L_1 and R_1, and C_1 are the components of the filter to filter the high-frequency harmonics in output voltages and currents from GSC. R_g and L_g represent the aggregated resistance and inductance of the transformers and transmission lines. The per-unit analysis is required for the aggregated analytical model. Hence, the per-unit values are calculated based on the parameters of the EMT testbed and listed in Table 2.1. The parameters of the EMT testbed are shown in Table 2.7.

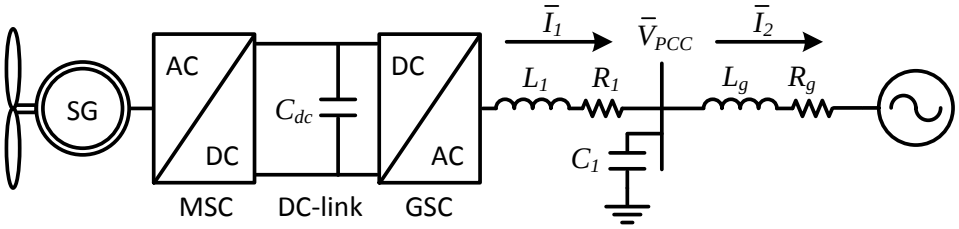

Figure 2.1: The topology of the detailed SG-based wind turbine (Type-4).

Table 2.1: Parameters of Simulink model

Parameters	Values (in pu if not specified)
Power level	$P = 0.9$
Nominal frequency	$\omega_0 = 377$ rad/s
Converter filter	$X_1 = 0.15$, $R_1 = 0.003$, $y_{c_1} = 0.25$
Transformer (T1)	$X_{T1} = 0.02$, $R_{T1} = 0.002$
Transformer (T2)	$X_{T1} = 0.03$, $R_{T1} = 0.003$
Long transmission line	$X_2 = 0.3$ to 0.7 , $R_2 = 0.03$ to 0.07
Short transmission line	$X_3 = 0.01$, $R_3 = 0.001$
DC time constant	$\tau = 0.0272$ s
Current control	$K_{pi} = 0.4758$, $K_{ii} = 3.28$
Power control	$K_{pp} = 1.1$, $K_{ip} = 137.5$
Voltage control	$K_{pv} = 0.25$, $K_{iv} = 25$
PLL (13 Hz)	$K_{p\text{PLL}} = 60$, $K_{i\text{PLL}} = 1400$
PLL (34 Hz)	$K_{p\text{PLL}} = 60$, $K_{i\text{PLL}} = 18200$
PLL (30 Hz)	$K_{p\text{PLL}} = 100$, $K_{i\text{PLL}} = 10000$
PLL (60 Hz)	$K_{p\text{PLL}} = 314$, $K_{i\text{PLL}} = 24700$

2.2.2 Analytical Models

Although the EMT testbeds can be used for the validation, demonstration, and replication, the analytical models are required to generate the linear analysis to help us understand the dynamic relations in the systems. The analytical model for Type-4 wind is proposed in [8]. It is known that the on-grid dynamics of Type-4 wind are mainly dependent on the control features of its GSC [5]. In addition, Type-4 wind turbines can be aggregated as one. Hence, the analytical model for Type-4 wind only considers the dynamics of GSC with vector control, PLL, the filter, the grid, and the transmission line. Two analytical models are shown in Fig. 2.2 and Fig. 2.3 for power control mode and dc-link voltage control mode respectively.

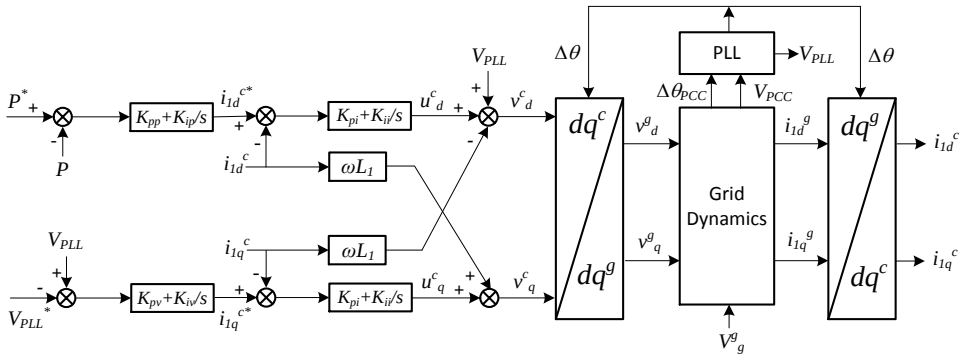

Figure 2.2: Analytical model for the Type-4 wind with power control mode.

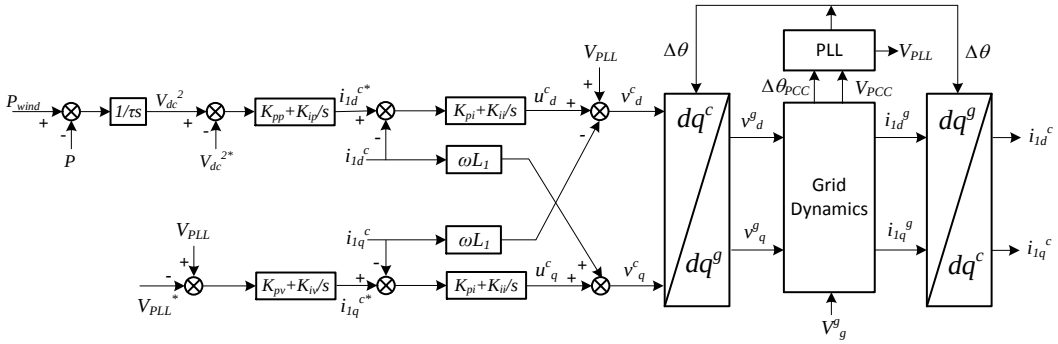

Figure 2.3: Analytical model for the Type-4 wind with dc-link voltage control mode.

In the analytical models, the vector control loops are modeled in detail while GSC is considered as the voltage source. In dc-lin voltage control mode, the integration of the power deviation

$(P_{wind} - P)$ is considered as the square of the measured dc-link voltage [13]. P_{wind} is the power generated by the wind turbine while P is the power generated by the GSC. τ is related to the dc-link capacitor. To generate the linear analysis such as the eigenvalues, the analytical models need to be linearized with the flat run. How to build the analytical model and linearize the model are presented by our previous publications [8, 68, 71] so they will not be presented in this dissertation.

2.3 Dynamics of PLL on Stability Issues

PLL is necessarily used to synchronize the converter with the grid. As mentioned in Chapter 1, kinds of advanced PLLs have been proposed in recent years but the SRF-PLL is still the most widely used and studied for three-phase applications [8, 14–16, 73].

2.3.1 SRF-PLL

SRF-PLL is the second-order application and it is modeled in analytical models. It uses the PCC bus three-phase voltages as inputs and it outputs the PCC bus voltage magnitude, frequency, and a reference angle which is used for park transformations. The topologies of the SRF-PLL in *abc* frame and *dq* frame are shown in Fig. 2.4.

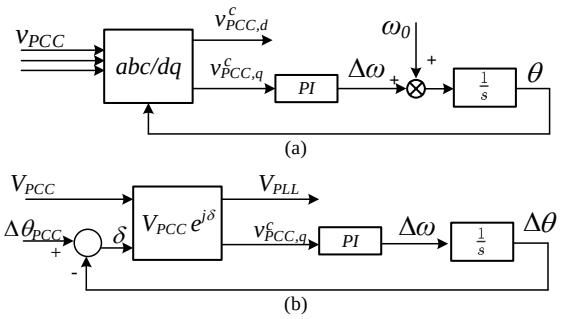

Figure 2.4: Block diagrams of the SRF-PLL. (a) Original PLL; (b) PLL in *dq*-frames.

The effect of its bandwidth has been studied by many papers [16, 74, 75]. The higher bandwidth leads to the faster detection of the voltage angle while the lower bandwidth can filter the high-order harmonics in the utility voltage. Four SRF-PLLs with different control gains are selected to

examine their effects on the oscillation modes. Four sets of controller gains are listed in Table 2.1. Their dynamics can be indicated by Fig. 2.5.

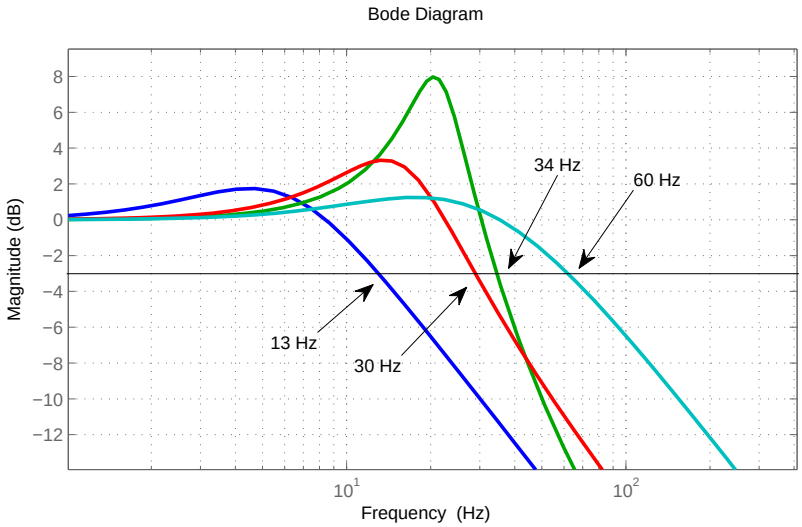

Figure 2.5: PLLs with four different bandwidth: 13 Hz, 30 Hz, 34 Hz and 60 Hz.

2.3.1.1 Eigenvalue Analysis

These four SRF-PLLs are implemented in the analytical model with the dc-link voltage control mode. After the linearization, their eigenvalue analysis related to the grid strength is generated in Table 2.2 and Fig. 2.6.

Table 2.2 lists the eigenvalues for the 13 Hz and 34 Hz SRF-PLLs under their own margin conditions. $X_2 = 0.60$ for the 13 Hz SRF-PLL while $X_2 = 0.46$ for the 34 Hz SRF-PLL. X_2 is the reactance of the transmission line. The dominant modes are bold for each case. With 13 Hz SRF-PLL, $\lambda_{8,9}$ are the dominant modes with low-frequency oscillation at 5.02 Hz. With 34 Hz SRF-PLL, the dominant modes are $\lambda_{6,7}$ and their oscillation frequency is 23.8 Hz. It is found that the bandwidth of PLL can determine the oscillation frequency of the system.

To analyze the effect of SCR on system stability, X_2 is increased until the system becomes unstable. Each increment on X_2 is 0.02 pu. Fig. 2.6 presents four eigenvalue loci for four SRF-PLLs respectively. In all four eigenvalue loci, there are two oscillation modes that are more sensitive

Table 2.2: Modes for different bandwidth of PLL under marginal conditions

Mode	13 Hz PLL	34 Hz PLL
λ_1	-1174	-1172
$\lambda_{2,3}$	-507.6±j2π×337.6	-477.8±j2π×347.4
$\lambda_{4,5}$	-52.5±j2π×151.2	-52.9±j2π×167.0
$\lambda_{6,7}$	-49.2±j2π×22.28	$\mathbf{-0.4 \pm j2\pi \times 23.8}$
$\lambda_{8,9}$	$\mathbf{-0.3 \pm j2\pi \times 5.02}$	-8.0±j2π×9.44
λ_{10}	-97.3	-224.3
$\lambda_{11,12}$	-17.4±j2π×1.10	-34.3±j2π×0.08
λ_{13}	-34.5	-16.7

to grid strength. One belongs to the low-frequency oscillation (less than 10 Hz) while another one belongs to the subsynchronous oscillation (above 20 Hz).

Although both modes move to the right half-plane (RHP) with the reduction of grid strength, which mode becomes dominant is different in four eigenvalue loci. The low-frequency oscillation mode is dominant with 13 Hz SRF-PLL while the subsynchronous-frequency mode is dominant with 60 Hz SRF-PLL. Furthermore, a lower PLL bandwidth is better for stability after comparing their margin conditions shown in Fig. 2.6a and Fig. 2.6d. The marginal X_2 is 0.60 pu for an SRF-PLL with lower bandwidth while X_2 is 0.56 pu for a faster SRF-PLL.

Besides the bandwidth, the damping of SRF-PLL affects system stability as well. Based on Fig. 2.5, 34 Hz SRF-PLL and 30 Hz SRF-PLL have similar bandwidth while having different damping. In Fig. 2.6b, the subsynchronous-frequency mode is dominant with the 34 Hz PLL which has less damping. On the other hand, the 30 Hz PLL with more damping makes the low-frequency oscillation mode dominant as shown in Fig. 2.6c.

2.3.1.2 Participation Factors

The participation factor is the method to determine which states are most relevant to a specific mode. Table 2.3 lists the participation factors for the subsynchronous mode $\lambda_{6,7}$ and the low-frequency mode $\lambda_{8,9}$ because they are the dominant modes in their own cases. The high participation factors indicate the most relevant relations and are marked as bold in the table. It is found that the subsynchronous mode $\lambda_{6,7}$ is related to dc-link dynamics, dc-link voltage con-

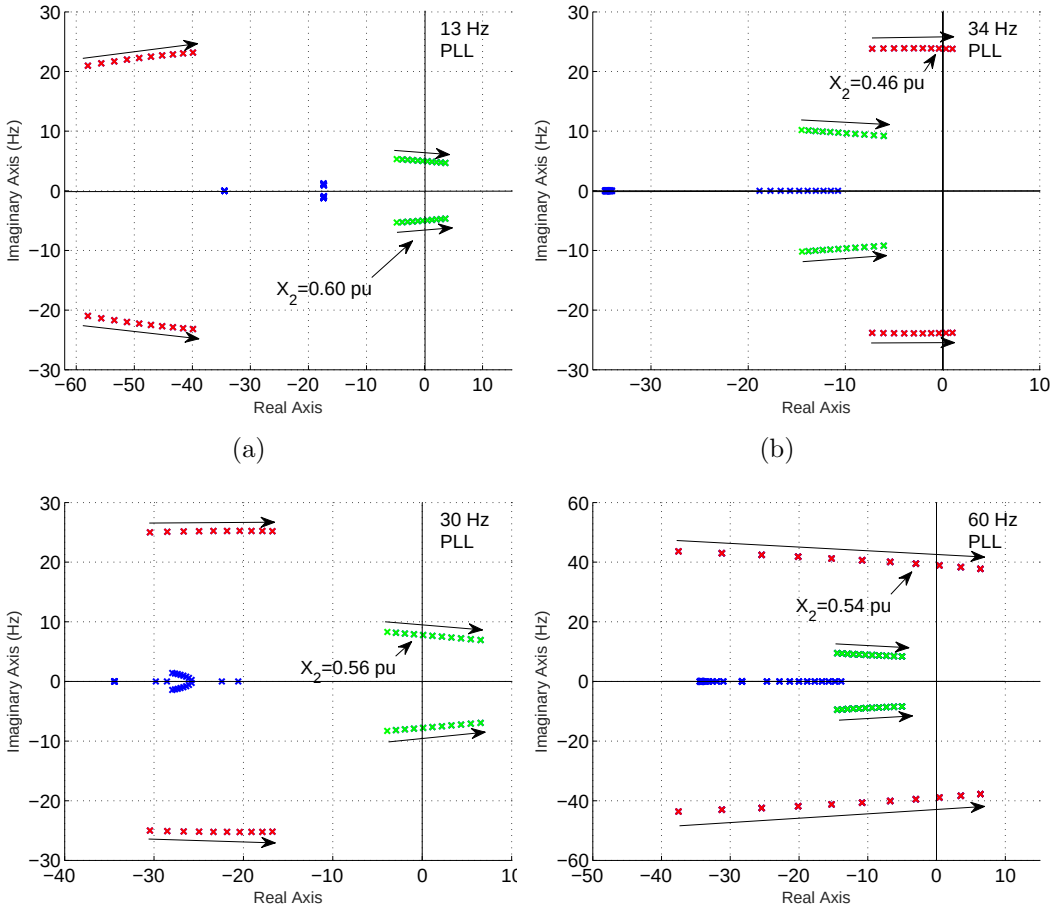

Figure 2.6: Eigenvalue loci for the SRF-PLL with different bandwidth. For each PLL, ten operating conditions are presented. (2.6a) (2.6c): X_2 changes from 0.5 to 0.7. (2.6b) X_2 changes from 0.3 to 0.5. (2.6d) X_2 changes from 0.4 to 0.6. Green ones notate low-frequency mode while red ones notate subsynchronous-frequency mode.

trol, and PLL. With lower bandwidth of PLL, only low-frequency oscillation mode $\lambda_{8,9}$ is related to PLL and the ac voltage control (x_2). With higher bandwidth of PLL, both low-frequency and subsynchronous-frequency modes are related to dc-link dynamics, dc-link voltage control, and PLL.

2.3.2 Lead/lag PLL

The aforementioned papers focus on improving the performance of SRF-PLLs under the distorted grid conditions. However, the analysis and simulation of the PLL in this study are based

Table 2.3: Participation factors under marginal conditions

	13 Hz PLL		34 Hz PLL	
States	$\lambda_{6,7}$	$\lambda_{8,9}$	$\lambda_{6,7}$	$\lambda_{8,9}$
V_{dc}^2	**0.3427**	0.0926	**0.1934**	**0.4157**
i_{1d}^g	0.1031	0.0006	0.0457	0.0077
i_{1q}^g	0.0404	0.0077	0.0360	0.0106
i_{2d}^g	0.1145	0.0039	0.0653	0.0349
i_{2q}^g	**0.2350**	0.0345	**0.2217**	0.0223
$v_{\text{PCC},d}^g$	0.0406	0.0053	0.0276	0.0017
$v_{pcc,q}^g$	0.0229	0.0017	0.0101	0.0046
θ	**0.2297**	**0.3464**	**0.3979**	**0.1463**
$\Delta\omega$	0.0377	**0.2072**	**0.3571**	**0.1474**
x_1	**0.2692**	0.0900	**0.1240**	**0.3963**
x_2	0.0479	**0.2129**	0.0165	0.0501
x_3	0.0119	0.0012	0.0059	0.0095
x_4	0.0948	0.1446	0.0320	0.0450

on the ideal utility voltage. Meanwhile, all the above PLLs are based on the SRF-PLL so they have the dynamic characteristics of the SRF-PLL. Except for the lead/lag PLL, others need to be modeled with the $\alpha\beta$ frame. The analytical model cannot be linearized with the flat run if the $\alpha\beta$ frame is modeled in. Hence, the lead/lag PLL is modeled in the analytical model to compare with SRF-PLL. Lead/lag PLL is proposed in 2003 to provide better filtering performance using a lead/lag controller to replace the PI controller in SRF-PLL [17]. Its topology is shown in Fig. 2.7. The lead/lag PLLs are designed to match the bandwidth of SRF-PLLs, 13 Hz and 34 Hz. Its parameters are listed in Table 2.4. The bandwidth comparison is shown in Fig. 2.8.

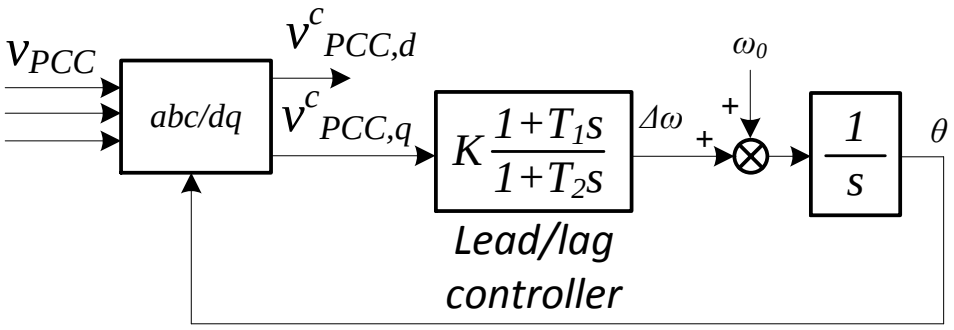

Figure 2.7: Topology of lead/lag PLL.

Table 2.4: Parameters of lead/lag PLLs

13.5 Hz	34 Hz
$T_1 = 0.0037$	$T_1 = 0.0013$
$T_2 = 0.0232$	$T_1 = 0.0232$
$K = 91$	$K = 457$

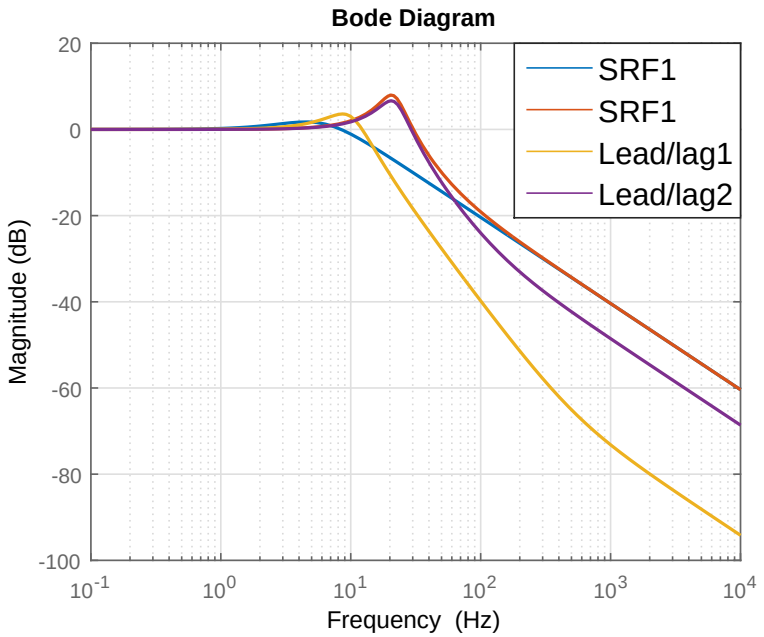

Figure 2.8: Bandwidth comparison between SRF-PLL and lead/lag PLL.

2.3.2.1 Eigenvalue Analysis

The eigenvalue loci for the lead/lag PLL with two different bandwidth are generated to compare with SRF-PLL. They are shown in Fig. 2.9b and Fig. 2.9d. The corresponding eigenvalue loci of SRF-PLLs in Fig. 2.6a and Fig. 2.6b are copied in Fig. 2.9a and Fig. 2.9c for the comparison. It is found that lead/lag PLL makes the system have higher margin conditions for both bandwidth. In other words, lead/lag PLL can improve the system stability. However, as same as SRF-PLL, lead/lag PLL with the higher bandwidth also makes the subsynchronous oscillation mode as the dominant one. Hence, for both types of PLLs, their dynamics can influence the oscillation mode in Type-4 wind connected to the weak grid.

2.4 Stability Control

Stability control is designed based on the mechanism behind instability on wind farms connected to the weak grid. This mechanism has been introduced in [29]. The principles of the stability control based on this mechanism is presented in [71]. Hence, this section will provide a brief of principles but it will focus on the evaluation of stability control using analytical results.

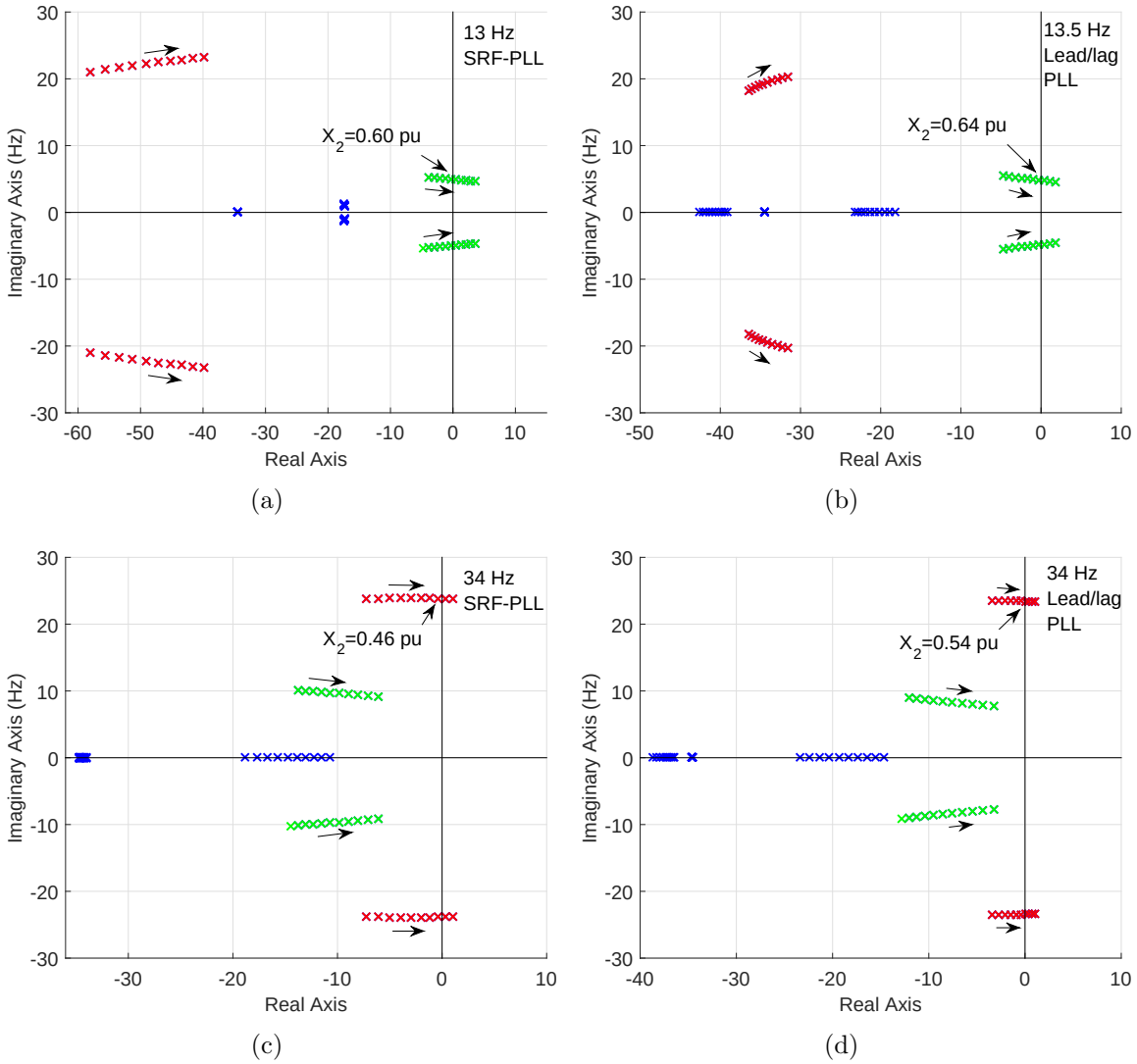

Figure 2.9: Eigenvalue loci for the SRF-PLL and lead/lag PLL with two different bandwidth. (2.9a) 13 Hz SRF-PLL: X_2 changes from 0.5 to 0.7. (2.9a) 34 Hz SRF-PLL: X_2 changes from 0.3 to 0.5. (2.9b) 13.5 Hz lead/lag PLL: X_2 changes from 0.5 to 0.7. (2.9d) 34 Hz lead/lag PLL: X_2 changes from 0.4 to 0.6.

2.4.1 Principles

Fig. 2.10 presents an aggregated Type-4 wind connected to the grid. The grid strength can be represented by the line reactance X_g. For Type-3 wind, there should be an additional shunt admittance to represent double-fed induction generator's circuit components.

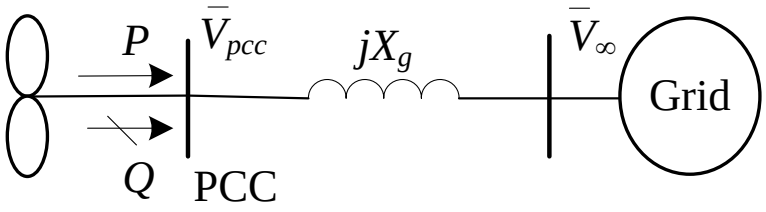

Figure 2.10: A wind farm and grid integration system.

After the linearization, the simple circuit in Fig. 2.10 can be represented by the block diagrams shown in Fig. 2.11. The detailed linearization process is provided in [71]. Based on Fig. 2.11, an increment in output power ΔP will lead the d-axis current Δi_d increased and the increased Δi_d will lead to a reduction in the PCC voltage ΔV_{pcc} because of negative c [71]. However, the reduced ΔV_{pcc} will lead to a reduction in ΔP. Hence, the principle of stability control is to solve this conflict situation by reducing the coupling relation between ΔP and ΔV_{pcc}.

Two feedback control strategies are proposed to suppress the effect of ΔV_{PCC} on real power ΔP and they are marked by the dark blue in Fig. 2.11a and Fig. 2.11b respectively. The first approach is to add a positive feedback of Δi_d on the power through a proportional gain K_{id}. The second strategy is to add a negative feedback of ΔV_{pcc} on the power through another proportional gain K_{vpll}. Which strategy will have the better performance can be evaluated using eigenvalue loci which are generated from the analytical models.

2.4.2 Eigenvalue Analysis

The mechanism analysis in the above subsection does not include the dynamics of PLL and simplifies the inner loop as a low-pass filter. However, in [8, 68], it is proved that PLL dynamics have a significant effect on the stability of RES in the weak grid. Therefore, the stability control

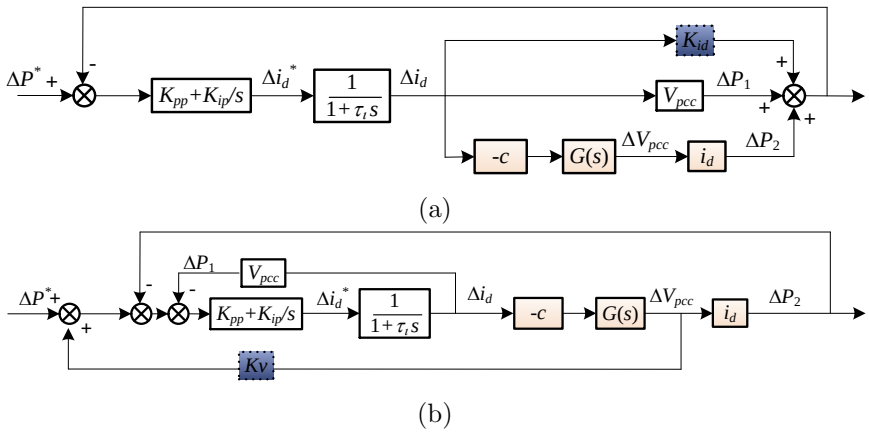

Figure 2.11: Linear block diagrams for two feedback controls. (2.11a): Δi_d as input signal. (2.11b): ΔV_{PCC} as input signal.

strategies need to be implemented in the analytical models shown in Fig. 2.2 and Fig. 2.3 to analyze the performance. Two analytical models with the stability control strategies are shown in Fig. 2.12. Model 1 shown in Fig. 2.12a indicates the wind with the active power control mode in GSC while Model 2 in Fig. 2.12b is the aggregated single-inverter wind with dc-link voltage control mode in GSC. The stability controls in two analytical models will be analyzed separately.

2.4.2.1 Power Control Mode

As aforementioned, two strategies of stability control are using two kinds of feedback signals, ΔV_{pll} and Δi_{1d}. In Fig. 2.12a, both feedback signals are used to modulate the real power through two different proportional gains, K_{id} and K_{vpll}. The output of the proportional control with ΔV_{pll} as the input signal is added to the power order. The output of the control with Δi_{1d} as input is subtracted from the power order. Which strategy is activated will be dependent on the values of K_{id} and K_{vpll}. If their values are zero, the stability control is deactivated. Otherwise, it is activated. In this dissertation, both control strategies will be activated to evaluate which control strategy has better performance.

The eigenvalue loci are generated to analyze the performance of each stability control strategy. Table 2.5 lists the parameters used in the EMT testbeds and their per-unit values which are used in the analytical model. The system operates at 0.9 pu power and the PCC voltage is at 1 pu. Fig.

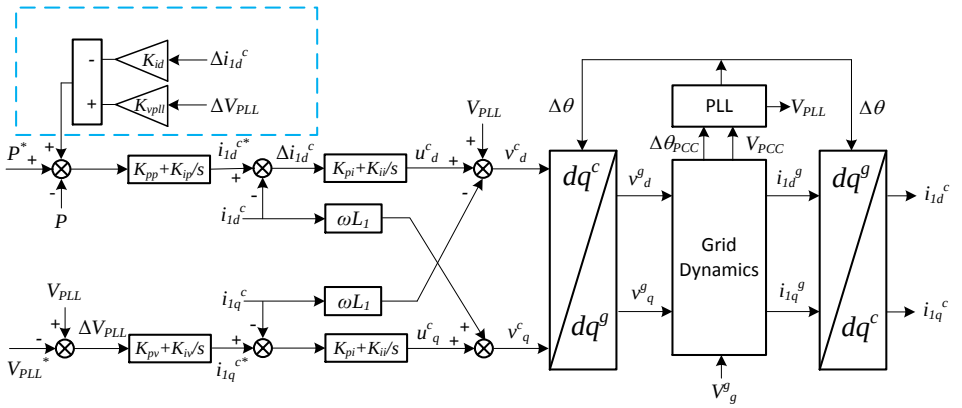

(a)

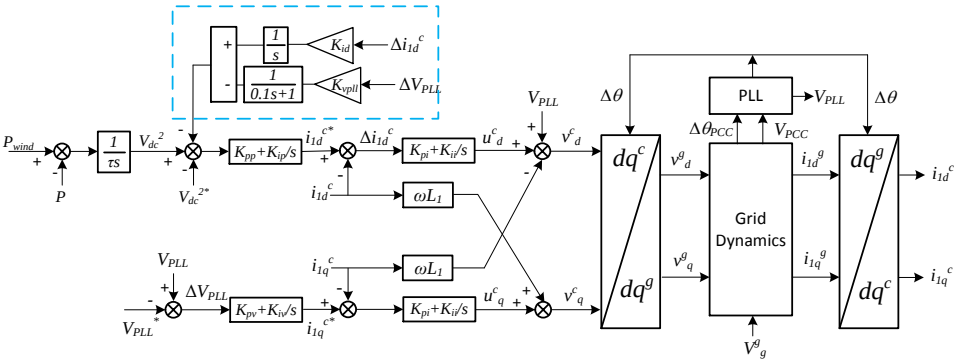

(b)

Figure 2.12: Feedback controls are implemented in Model 1 (2.12a) and Model 2 (2.12b).

2.13 shows the eigenvalue loci of the analytical model in Fig. 2.12a with the change of transmission line (or grid strength) X_g. As noted but not plotted, the marginal stable condition for the system without stability control is $X_g = 0.86$ pu. Hence, a marginal unstable $X_g = 0.88$ pu is selected as the initial condition to test how the different values of K_{id} or K_{vpll} affect the system stability. Based on Fig. 2.13a and Fig. 2.13b, it is found that 10 is large enough for K_{id} to make the system stable. For K_{vpll}, 0.9 is the best value because there is a tradeoff between two oscillation modes.

With either of the fixed $K_{id} = 10$ and $K_{vpll} = 0.9$, Fig. 2.13c and Fig. 2.13d show that the eigenvalues move to the right half-plane (RHP) corresponding to the increment of X_g. Although both control strategies make the system stable even if $X_g = 1.1$ pu ($SCR = 1$), the voltage-based stability control is preferred over the current-based stability control. The reason is that the current-

Table 2.5: Parameters of Model 1 and Type-3 wind testbed

Parameter	Value (SI)	Per-unit (pu)
# of WT	60	
Rated power	1.5 MW	0.9
DC-link voltage	1150 V	
Rated voltage	575 V	1
Nominal freq.	60 Hz	1
$L_{ls}(X_{ls}), R_s$	94.5 μH, 5.6 mΩ	0.18, 0.023
$L'_{lr}(X'_{lr}), R'_r$	84.0 μH, 3.9 mΩ	0.16, 0.016
$L_m(X_m)$	1.5 mH	2.9
Inertial, poles	8.03 J, 6	
Friction factor	0.01	
C_{dc}	10 mF	
$L_c(X_c), R_c$	0.16 mH, 0.59 mΩ	0.3, 0.03
$C_1(B_1)$	2.9 mF	0.267
$L_{T1}(X_{T1}), R_{T1}$	0.165 mH, 6.25 mΩ	0.02, 0.002
$L_{T2}(X_{T2}), R_{T2}$	19.25 mH, 725 mΩ	0.03, 0.003
$L_2(X_2)$	$0.58 \rightarrow 1.35$ H	$0.45 \rightarrow 1.05$
R_2	$21.78 \rightarrow 50.82$ Ω	$0.045 \rightarrow 0.105$
Current control	$K_{pi} = 0.6$, $K_{ii} = 8$, pu	
Power control	$K_{pp} = 0.4$, $K_{ip} = 40$, pu	
Voltage control	$K_{pv} = 0.25$, $K_{iv} = 25$, pu	
PLL	$K_{p\text{PLL}} = 60$,$K_{i\text{PLL}} = 1400$, pu	

based stability control requires a much larger gain based on Fig. 2.13a but the large gain may lead the overcurrent or overpower to hit limitations in the practical control loop.

Fig. 2.14 presents the time-domain responses from the analytical model with a small disturbance (0.001 pu increment in the power order) at $t = 2$ s. With the PCC voltage-based control, the wind farm can transfer 1 pu power to the very weak grid (SCR = 1).

2.4.2.2 Dc-link Voltage Control Mode

The dc-link voltage control mode has the different stability control structure. In dc-link voltage control mode, the dc-link capacitor dynamics is modeled to calculate the dc-link voltage from the power. To achieve a similar effect of modulating the power order using feedback signals, the integrator is added in the stability control. However, the time simulation results show that modulating the dc-link voltage reference with the output from an integrator control with PCC

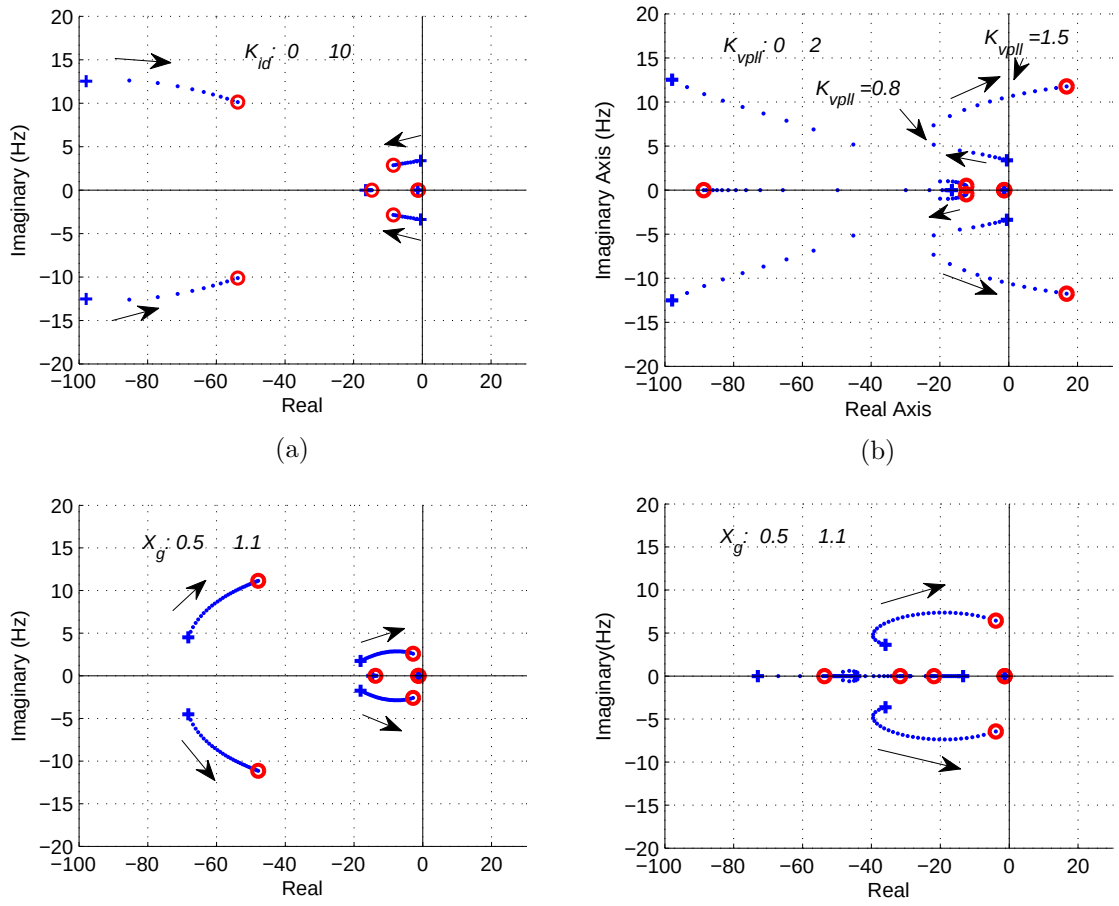

Figure 2.13: Eigenvalue loci for the power control. $P = 0.9$, $V_{\text{PCC}} = 1$. (2.13a): increase K_{id} from 0 to 10 with $X_g = 0.88$ pu. (2.13b) increase K_{vpll} from 0 to 2 with $X_g = 0.88$ pu. (2.13c): increase X_g with $K_{id} = 10$. (2.16d) increase X_g with $K_{vpll} = 0.9$.

voltage input may lead to an increase or reduction of the dc-link voltage at steady-state. To keep the dc-link voltage at its reference, a high-pass filter (HPF) ($\frac{s}{0.1s+1}$) is added after the integrator to filter out the dc component. The combination of $1/s$ and the HPF leads to a low-pass filter (LPF) ($\frac{1}{0.1s+1}$). The time simulation results are shown in Fig. 2.15 to compares the different dynamic responses of the system: without voltage-based stability control, with an integrator-based voltage feedback control, and with an additional HPF. The plotted responses include the output power, dc-link voltage, ΔV_{pll}, and the output of the stability control or compensation on V_{DC}. Based on Fig. 2.15, although the integrator-based feedback control of ΔV_{pll} can improve the stability, a dc

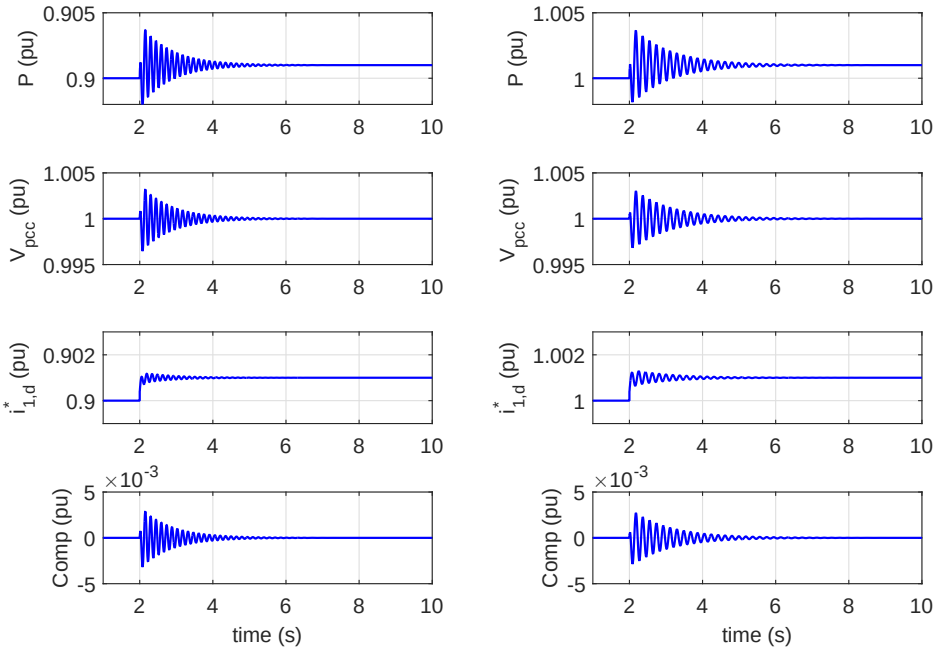

(a) (b)

Figure 2.14: Time-domain results with $K_{vpll} = 0.9$: (2.14a): $X_g = 1.1$ pu, $P = 0.9$ pu; (2.14b): $X_g = 1.0$ pu and $P = 1.0$ pu.

component is added to the dc-link voltage order at steady-state. With the HPF, the dc component can be eliminated.

Fig. 2.16 plots the eigenvalue loci for the system shown in Fig. 2.12b. The parameters for the analytical model with the dc-link voltage control mode are the same as Table 2.1. As noted but plotted, this system with the dc-link voltage control mode has the marginal stable condition at $X_g = 0.6$ pu. Fig. 2.16a and Fig. 2.16b demonstrate the movements of eigenvalues corresponding to the increments of K_{id} and K_{vpll} when the system is under condition of $X_g = 0.61$ pu. Both control strategies can enhance the system stability. The current-based stability control requires a very large gain while the voltage-based stability control can be set as $K_{vpll} = 2$ due to the tradeoff of two modes.

Fig. 2.16c and Fig. 2.16d present the eigenvalues loci based on a varying X_g with the fixed controller gain, $K_{id} = 4000$ or $K_{vpll} = 2$. $K_{id} = 4000$ makes the system stable under all of conditions

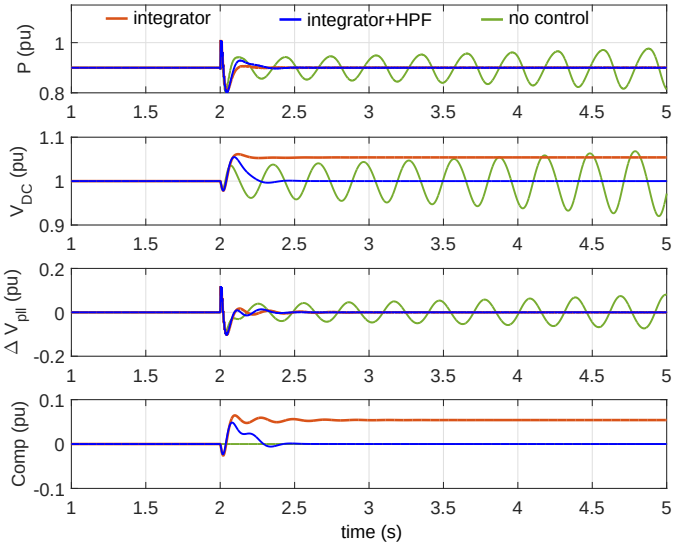

Figure 2.15: Comparison of dynamic responses with and without the HPF. $X_g : 0.5 \rightarrow 0.61$.

from $X_g = 0.5$ to $X_g = 1.1$ pu while $K_{vpll} = 2$ increases the marginal stable condition to $X_g = 1$ pu. As aforementioned, the feedback gain should not be too large so the voltage-based stability control is also preferred in dc-link voltage control mode.

Fig. 2.17 presents the time-domain responses from the analytical model with a small disturbance (0.01 pu reduction in ac voltage order) at $t = 2$ s. With the PCC voltage-based stability control, the wind farm can transfer more than 0.9 pu power to a very weak grid (SCR = 1). It can be seen when $P = 0.97$ and $X_g = 1$, the system has two oscillation frequencies, one at 7 Hz and the other at 2 Hz. The time-domain simulation results corroborate with the eigenvalue analysis in Fig. 2.16d where two modes, one at 7 Hz and the other at 2 Hz, move towards the RHP when the grid becomes weaker.

2.5 Case Studies using EMT Testbeds

To validate the analytical results, several EMT testbeds are built in MATLAB/SimPowerSystems. Hence, this section does not only validate the analysis of PLL dynamics on the system stability but also demonstrates the torsional interactions between Type-4 wind and synchronous

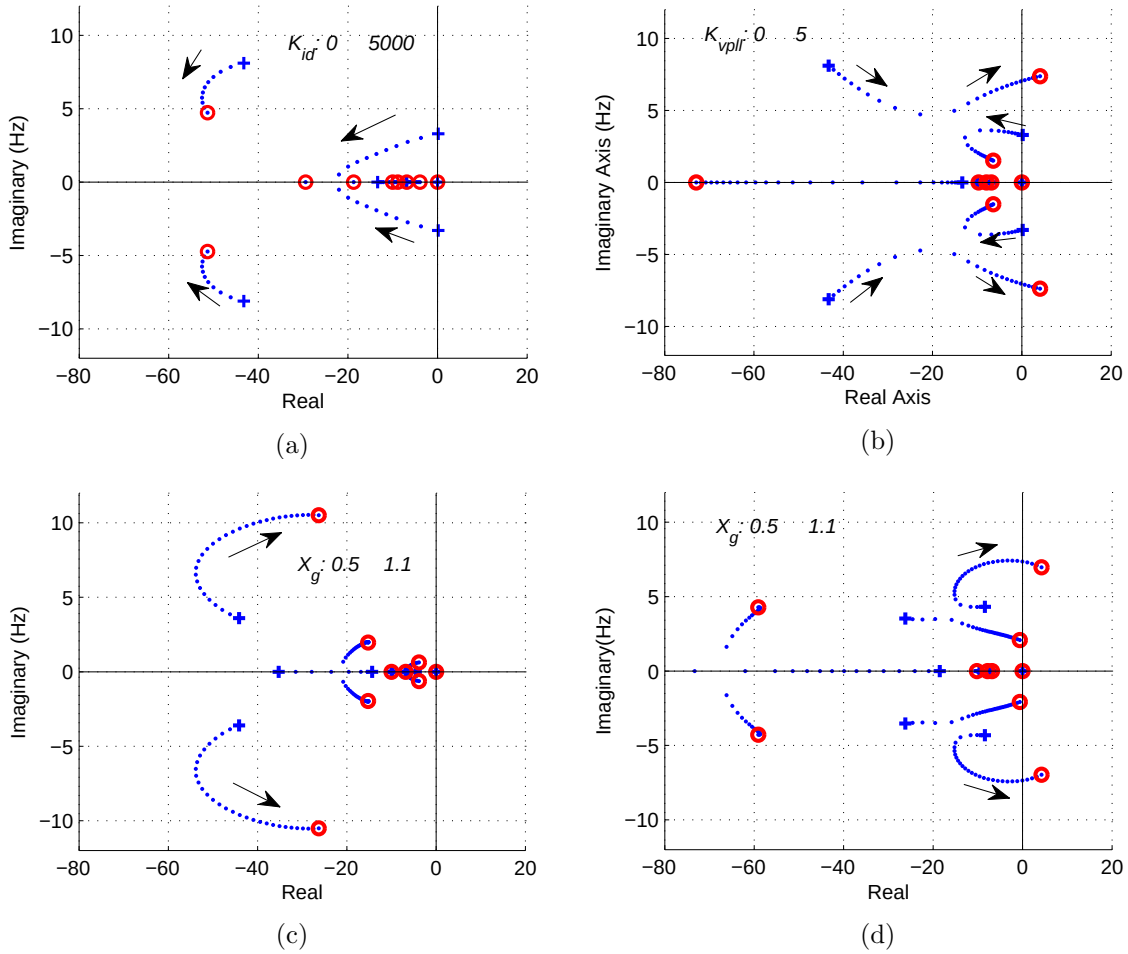

Figure 2.16: Eigenvalue loci for the dc-link control. (2.16a): increase K_{id} from 0 to 5000 with $X_g = 0.61$ pu. (2.16b) increase K_{vpll} from 0 to 5 with $X_g = 0.61$ pu. (2.16c): increase X_g with $K_{id} = 4000$. (2.16d) increase X_g with $K_{vpll} = 2$.

generator. Furthermore, the performance of stability control in Type-3 and Type-4 wind is also evaluated by the corresponding EMT testbeds.

2.5.1 Validation of Stability Analysis Related to PLL

In the above sections, it is claimed that the dynamics of PLL can affect the oscillation mode of Type-4 wind in the weak grid. To verify it, an EMT testbed is built in MATLAB/SimPowerSystems. It is developed from the demo of MATLAB named as *Wind Farm - Synchronous Generator and Full Scale Converter (Type 4) Average Model*. Type-4 wind block is built based on the General Electric (GE) Type-4 wind turbine generic model [76]. That Type-4 block is an aggregated model

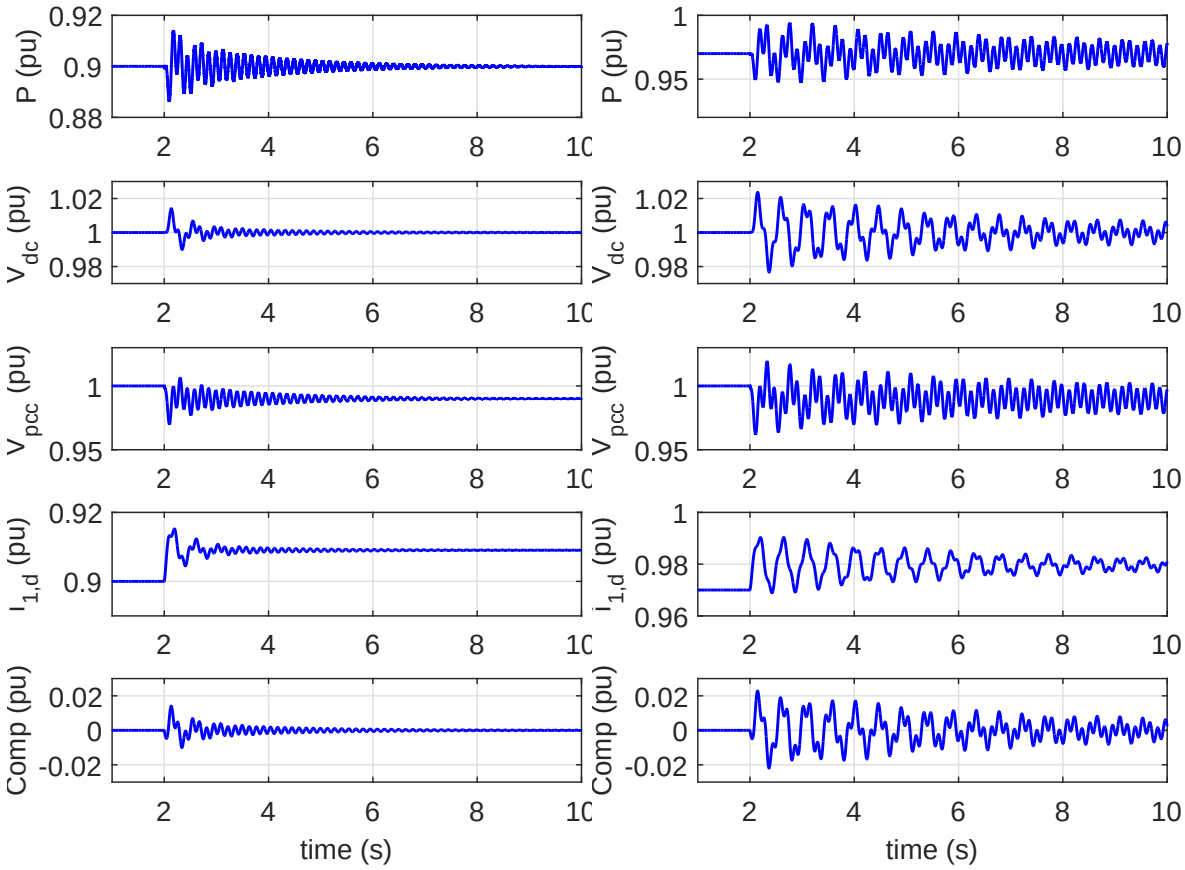

(a) (b)

Figure 2.17: Time-domain results with $K_{vpll} = 2$: (2.17a): $X_g = 1.01$ pu, $P = 0.9$ pu; (2.17b): $X_g = 1$ pu and $P = 0.97$ pu.

of multiple 2 MW wind turbines. The parameters of the synchronous generator used in Type-4 wind are listed in Table 2.8. The wind farm is represented by this Type-4 block and its size can be determined by the number of Type-4 wind turbines. The parameters of the wind farm are listed in Table 2.7. In this case study, a 100 MW Type-4 wind farm consisting of fifty 2 MW Type-4 wind turbines is connected to a 220 kV grid through a long transmission line. Two transformers, 0.575 : 25 kV and 25 : 220 kV, are used to boost the voltage level. To demonstrate the torsional interactions, a remote 600 MW synchronous generator is delivering power to the same grid as well. The details of the steam plant and torsional interactions will be presented in the next subsection. The topology of the entire testbed is shown in Fig. 2.18.

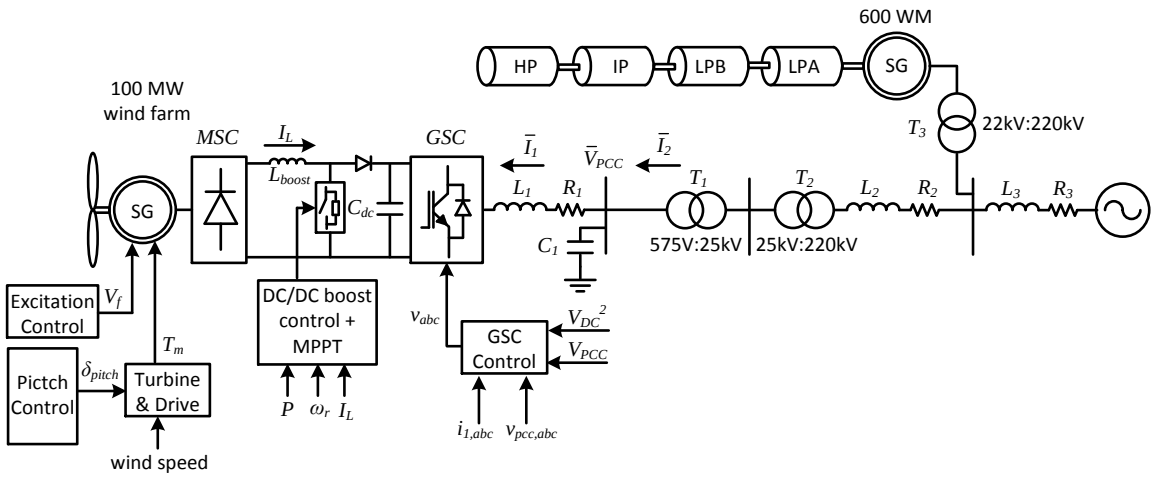

Figure 2.18: MATLAB/SimPowerSystems Testbed: a 100 MW Type-4 wind farm is connected to a grid through a long transmission line. A 600 MW steam turbine generator is also connected to the grid.

Table 2.6: Parameters of Type-4 wind turbine

Parameter	Value (SI)
Rated real power	2 MW
DC-link voltage	1100 V
Rated voltage	575 V
Nominal frequency	60 Hz
$X_d, X_d^{'}, X_d^{''}$	313 mΩ, 71.0 mΩ, 60.5 mΩ
$X_q^{'}, X_q^{''}$	114 mΩ, 58.3 mΩ
R_s,X_l	1.44 mΩ, 40.8 mΩ
$T_{do}^{'}, T_{do}^{''}$	4.49 s, 0.0681 s
$T_{qo}^{''}$	0.0513 s
Inertial, friction factor	0.62 s, 0.01
poles	2
L_{boost}	1.2 mH
C_{dc}	90 mF
L_1, R_1, C_1	0.06 mH, 0.45 mΩ, 3.6 mF

The dynamic events are designed using the transmission line tripping. It is assumed that $R_2 + jX_2$ is the equivalent impedance of two parallel transmission lines. If one parallel transmission line is tripped, the line impedance $R_2 + jX_2$ will be increased to reduce the grid strength. 13 Hz SRF-PLL and 34 SRF-PLL were implemented in the EMT testbeds for the validation. Lead/lag PLLs were not testbed because they have very similar dynamics of SRF-PLL. Each SRF-PLL

was examined by three different cases, stable condition, marginal stable condition, and marginal unstable condition. Hence, there were six cases studied totally and they are listed as follows.

Table 2.7: Parameters of Type-4 wind farm

Parameter	Value (SI)
Number of WT	50
Rated power	100 MW
Nominal frequency	60 Hz
L_{T1}, R_{T1}	0.30 mH, 11.3 mΩ
Rated voltage	220 kV
L_{T2}, R_{T2}	23.1 mH, 0.87 Ω
L_2, R_2	462 to 705 mH, 17.4 to 26.6 Ω
L_3, R_3	11.6 mH, 0.44 Ω

The initial value of X_2 is 0.4 pu. In Case 1 (13 Hz PLL), X_2 is increased to 0.46 pu. In Case 2 (13 Hz PLL), X_2 is increased to 0.58 pu. In Case 3 (13 Hz PLL), X_2 is increased to 0.61 pu. In Case 4 (34 Hz PLL), X_2 is increased to 0.44 pu. In Case 5 (34 Hz PLL), X_2 is increased to 0.46 pu. In Case 6 (34 Hz PLL), X_2 is increased to 0.48 pu.

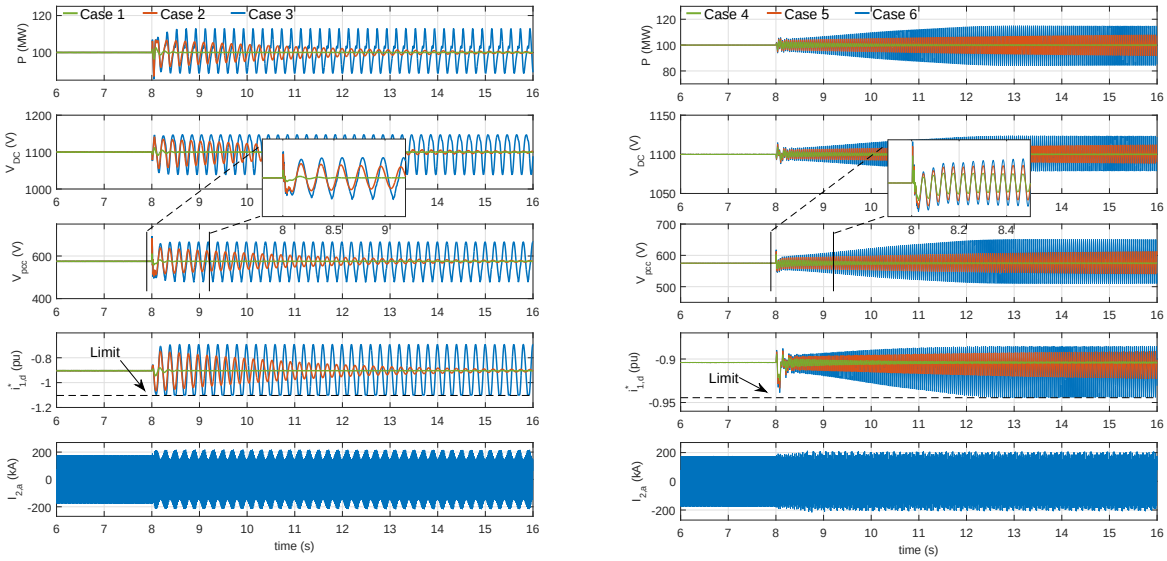

(a) (b)

Figure 2.19: The dynamic responses of Type-4 wind farm. (a)13 Hz PLL; (b) 34 Hz PLL.

Fig. 2.19 presents the dynamic responses of Type-4 wind including the generated power, dc-link voltage, PCC voltage, d-axis current order, and instantaneous grid current on phase a. The dynamic events happened at 8 sec. Fig. 2.19a shows the dynamic responses of Type-4 wind with 13 Hz SRF-PLL while Fig. 2.19b shows them corresponding to the 34 Hz SRF-PLL. Fig. 2.20 presents the fast Fourier transformation (FFT) results for the wind power, phase-a current, and the speed deviation of HP based on a time window of data from 9 seconds to 16 seconds.

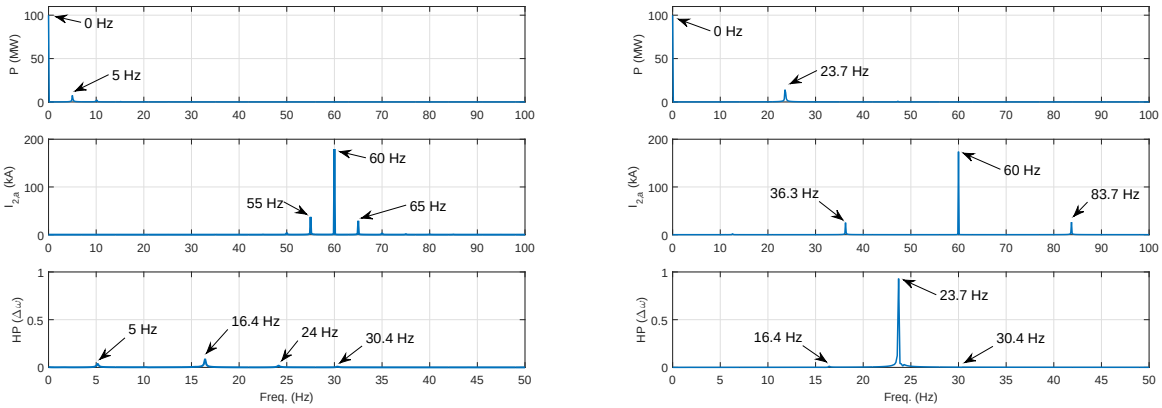

(a) (b)

Figure 2.20: FFT analysis for wind power P, AC current $I_{2,a}$, and $\Delta\omega$ of high-pressure rotor. (a) 13 Hz PLL, Case 3; (b) 34 Hz PLL, Case 6.

Based on Fig. 2.19a, a low-frequency oscillation was observed in the dynamic responses after 8 sec. FFT results in Fig. 2.20a pointed out that the wind power had a 5 Hz oscillation. This 5 Hz is in dq frame so a 55 Hz and a 65 Hz harmonics appeared in the phase-a current. Based on Fig. 2.19b, a subsynchronous oscillation occurred in the dynamic responses after the line tripped. Fig. 2.20b indicates that the oscillation frequency in the wind power was 23.7 Hz. In the phase-a current, the harmonics were 36.3 Hz and 86.7 Hz.

2.5.2 Demonstration of Torsional Interaction

In the testbed shown in Fig. 2.18, the 600 MW synchronous generator model is also developed from a demo in MATLAB/SimPowerSystems named as *Steam Turbine and Governor System* -

Subsynchronous Resonance. The parameters of the 600 MW synchronous machine are from [77] and listed in Table 2.8. The generator turbine employed a more comprehensive shaft model from Chapter 15 in [78] including four turbine rotors, two low-pressure turbine rotors (LPA and LPB), an intermediate-pressure turbine rotor (IP), and a high-pressure turbine rotor (HP). Hence, this steam generator has four torsional modes which are listed in Table 2.8 as well. Note that one torsional mode (24 Hz) is very close to the 23.7 Hz oscillation in Type-4 wind with 34 Hz PLL. The following figures will show the torsional interactions when the subsynchronous-frequency mode became dominant.

Table 2.8: Parameters of steam turbine and governor

Parameter	Value (SI)
Rated power	600 MW
Power level	300 MW
Rated voltage	22 kV
Nominal frequency	60 Hz
$X_d, X_d^{'}, X_d^{''}$	1.33 Ω, 0.20 Ω, 0.16 Ω
$X_q, X_q^{'}, X_q^{''}$	1.28 Ω, 0.37 Ω, 0.16 Ω
X_l	0.11Ω
$T_{do}^{'}, T_{do}^{''}$	4.5 s, 0.04 s
$T_{qo}^{'}, T_{qo}^{''}$	0.67 s, 0.09 s
Inertial, poles	0.855 s, 2
Torsional Mode 1	16.3 Hz
Torsional Mode 2	24.1 Hz
Torsional Mode 3	30.3 Hz
Torsional Mode 4	44.0 Hz
L_{T3}, R_{T3}	5.7 mH, 4.84 Ω

During the cases in the above subsection, the steam synchronous generator was always connected to the same grid so it experienced the same dynamic events and instability issues as Type-4 wind. Fig. 2.21 presents the dynamic responses of the synchronous generator including the real power of the steam plant, speed deviations of five turbine rotors. In Fig. 2.21a, the 5 Hz also appeared in the output power of the synchronous generator and speed deviations of the generator rotor and turbine rotors. Based on the last plot of Fig. 2.20a, all torsional modes were reflected in the speed deviation of HP rotor.

In Fig. 2.21b, there were larger oscillations with a higher frequency that happened in the dynamic responses. Compared with 4 MW peak to peak oscillation in Fig. 2.21a, the synchronous generator power had a 10 MW peak to peak oscillation. Moreover, the speed deviation of HP rotor showed more obvious torsional interaction. For the 34 Hz SRF-PLL case, the peak to peak magnitude of the oscillation reaches 2 rad/s while it could be negligible for the 13 Hz SRF-PLL case. Based on the last plot of Fig. 2.20b, HP had a very large component of 23.7 Hz. It was caused by the interaction between 23.7 Hz oscillation and 24 Hz torsional mode. This is clear evidence of torsional interaction.

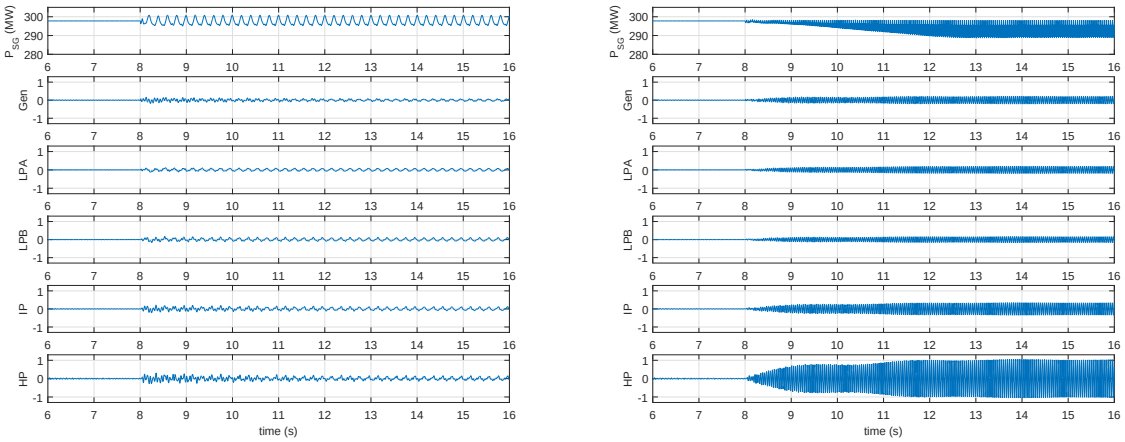

(a) (b)

Figure 2.21: The dynamic responses of the steam turbine governor. The lower ten plots are related to speed deviations in rad/s. (a) 13 Hz PLL, Case 3; (b) 34 Hz PLL, Case 6.

2.5.3 Implementation of Stability Control

Two testbeds in MATLAB/SimpPowerSystems are built up to validate the eigenvalue analysis of the systems with stability control. The testbeds align more with the real-world system with full dynamics and converter limitations modeled. One of the testbed is developed based on the MATLAB demo named as *Wind Farm - DFIG Average Model*. The topology of Type-3 testbed with stability control is shown in Fig. 2.22a and its parameters are listed in Table 2.5. Another testbed is the same as the Type-4 testbed in Fig. 2.18 but there is no steam generator. Its topology

with the stability control is shown in Fig. 2.22b and its parameters are the same with Table 2.6 and Table 2.7.

The rotor-side converter (RSC) in Type-3 wind testbed is operated in power control mode and it delivers the majority power. Hence, the stability control can be implemented in RSC of Type-3 like Model 1. On the other hand, the GSC of Type 4 wind testbed is under dc-link voltage control mode so it can be considered as Model 2.

Both testbeds use limitations to limit the converter current. In the Type-3 wind testbed, the saturation of the RSC current is $\begin{bmatrix} 0 & 0.9 \end{bmatrix}$ pu. In the Type-4 wind testbed, the range is $\begin{bmatrix} -1.1 & 1.1 \end{bmatrix}$ pu. These limitations cause that the best operating conditions of the analytical models cannot be achieved but the expected performance of stability still can be demonstrated.

2.5.3.1 Type-3 Wind

In the Type-3 wind testbed, the stability control strategies are implemented in RSC to modulate the power order. The rated output power from the Type-3 wind farm is kept at 90 MW or 0.9 pu (the base power is 100 MVA). At rated operating condition, the rotor speed is 1.25 pu so the slip equals -0.25. Due to -0.25 slip, the RSC d-axis current is 0.72 pu while the GSC d-axis current is 0.18 pu to the grid.

Fig. 2.23 presents the dynamic responses of Type-3 testbed for three scenarios: without stability control, with voltage-based control ($K_{vpll} = 0.9$), and with current-based control ($K_{id} = 10$). The feedback gains were selected based on the eigenvalue analysis in Fig. 2.13a and Fig. 2.13b. The dynamic event happened at $t = 2$ sec, X_g changed from 0.5 pu to 0.88 pu. 0.88 pu was selected because it is the marginal unstable condition for the system with power order control without the stability control. The plotted responses include wind output power P, dc-link voltage V_{DC}, PCC voltage V_{PCC}, RSC d-axis current order $i^*_{r,d}$, and the output from the stability control `Comp`.

Based on the red waves in Fig. 2.23, the system without the stability control suffered 3 Hz oscillations. This performance including the margin condition and oscillation frequency aligns with the eigenvalue analysis of the first condition in Fig. 2.13a or 2.13b. When the feedback gains are zeros, the marginal stable condition is 0.86 pu and the oscillation frequency is 3 Hz. Due to the

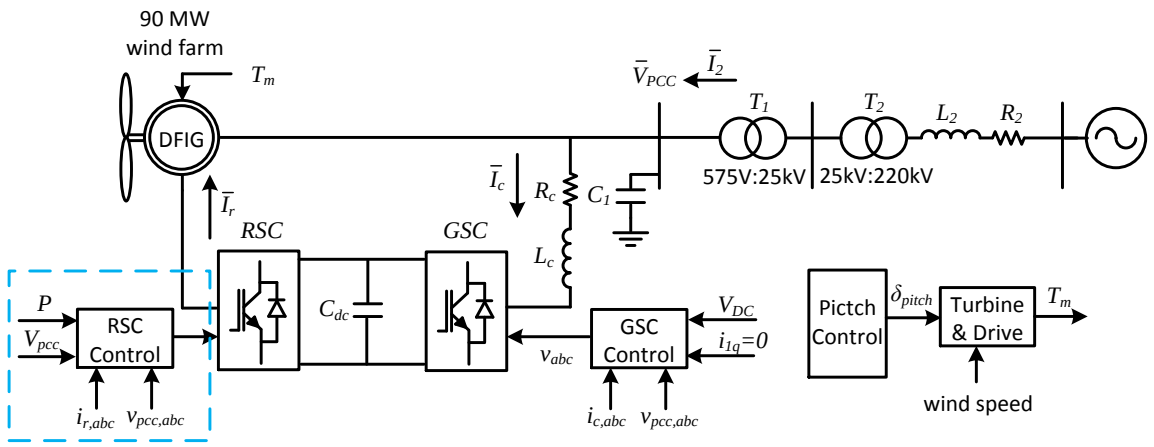

(a)

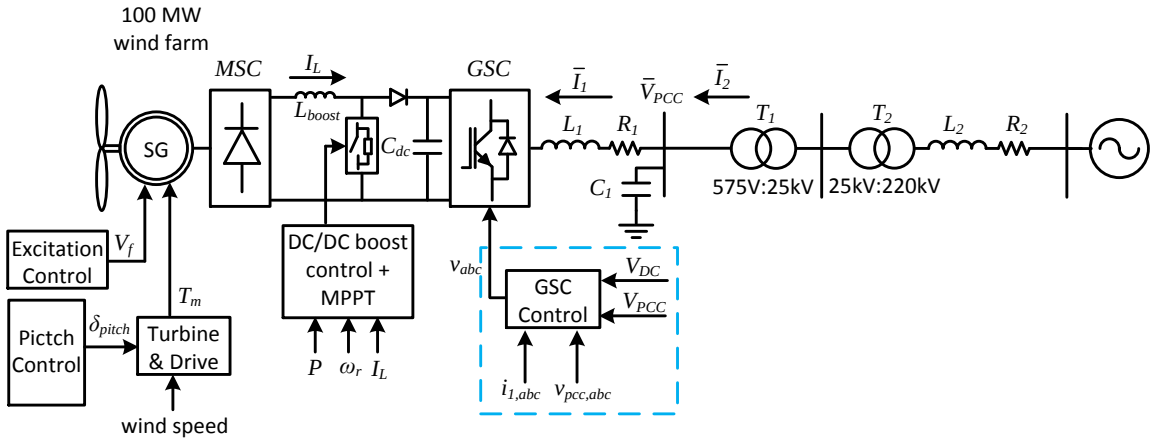

(b)

Figure 2.22: MATLAB/SimPowerSystems testbeds for Type-3 wind and Type-4 wind. (2.22a): a 90 MW Type-3 wind farm is connected to a grid through a long transmission line. (2.22b): a 100 MW Type-4 wind farm is connected to a grid through a long transmission line.

green waves, $K_{id} = 10$ did not improve the system stability because $i_{r,d}$ hit the current limitation in RSC. On the other hand, the voltage-based stability control $K_{vpll} = 0.9$ made the system stable obviously.

Further tests were conducted to find the new margin conditions of Type-3 wind testbed with the voltage-based control. We kept increasing X_g until the system became unstable. Fig. 2.24 presents the dynamic responses when $X_g = 1.0$ pu and 1.01 pu. The system was stable when $X_g = 1$ pu while unstable at $X_g = 1.01$ pu. Hence, the new marginal stable condition is $X_g = 1$ pu. This condition is lower than the eigenvalue analysis because of the limited $d-$axis of the rotor current.

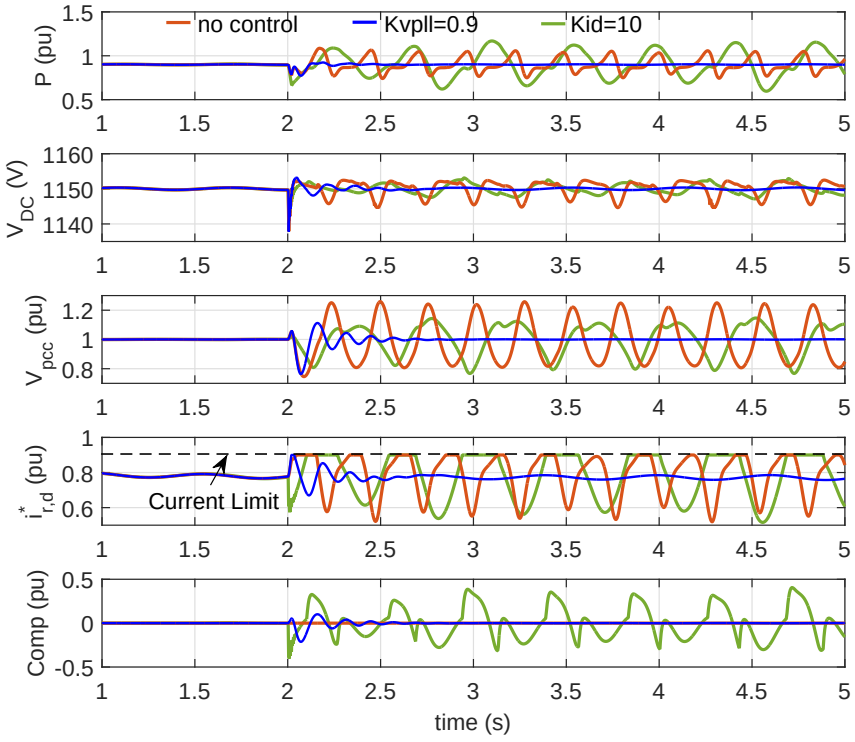

Figure 2.23: Type-3 wind testbed simulation results with $X_g : 0.5 \rightarrow 0.88$ at 2 sec. Red line: no control; Blue line: voltage-based control ($K_{id} = 0$, $K_{vpll} = 0.9$); Green line: current-based control ($K_{id} = 10$, $K_{vpll} = 0$).

2.5.3.2 Type-4 Wind

The rated output power of Type-4 wind testbed is 100 MW or 0.9 pu (the base power of the Type-4 wind is 110 MVA). The stability control strategies should be implemented in GSC of Type-4 wind to modulate V_{DC}. The first case study compared the system dynamic responses with and without voltage or current-based control. The dynamic event was still X_g which was increased from 0.5 pu to 0.61 pu at 2 seconds.

As same as power control mode, three scenarios were considered: without control, with voltage-based or current-based control. Fig. 2.25 presents the dynamic responses of Type-4 wind testbed in those three scenarios. As noted: $i_{1,d}$ is the converter current of GSC and its positive direction is from the grid to the GSC as shown in Fig. 2.22b. The values of K_{id} and K_{vpll} were selected as 4000 and 2 respectively based on Fig. 2.16a and Fig. 2.16b

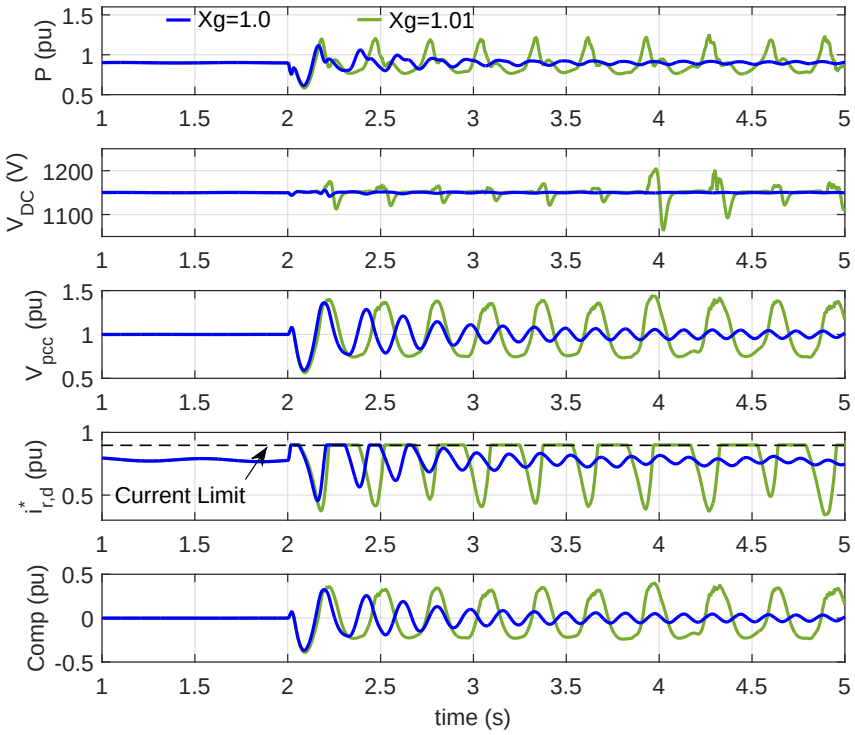

Figure 2.24: Type-3 wind testbed simulation results with $K_{vpll} = 0.9$. $X_g : 0.5 \rightarrow 1.0$ (blue line) and $X_g : 0.5 \rightarrow 1.01$ (green line).

The red waves in Fig. 2.25 showed that 3 Hz oscillations appeared in Type-4 wind without the stability control after the dynamic event. On the other hand, both voltage-based and current-based control made the system stable but the voltage-based control ($K_{vpll} = 2$) had better performance because of shorter transients and lower overshoot.

For the dc-link voltage control mode, the system operating limits were examined with both current-based control and voltage-based control.

Fig. 2.26 shows the dynamic responses of the system with current-based control for two large disturbances: $X_g : 0.5 \rightarrow 0.63$ and $X_g : 0.5 \rightarrow 0.64$. Due to the large overshoot hitting the current limits, the marginal stable condition was only improved from $X_g = 0.6$ pu to 0.63 pu. Fig. 2.27 presents the dynamic responses of the system with voltage-based control ($K_{vpll} = 2$) for two large disturbances: $X_g : 0.5 \rightarrow 0.91$, $X_g : 0.5 \rightarrow 0.92$. It was observed that the system was stable when X_g reached 0.91 pu. The marginal stable condition is increased from $X_g = 0.60$ pu to 0.91 pu.

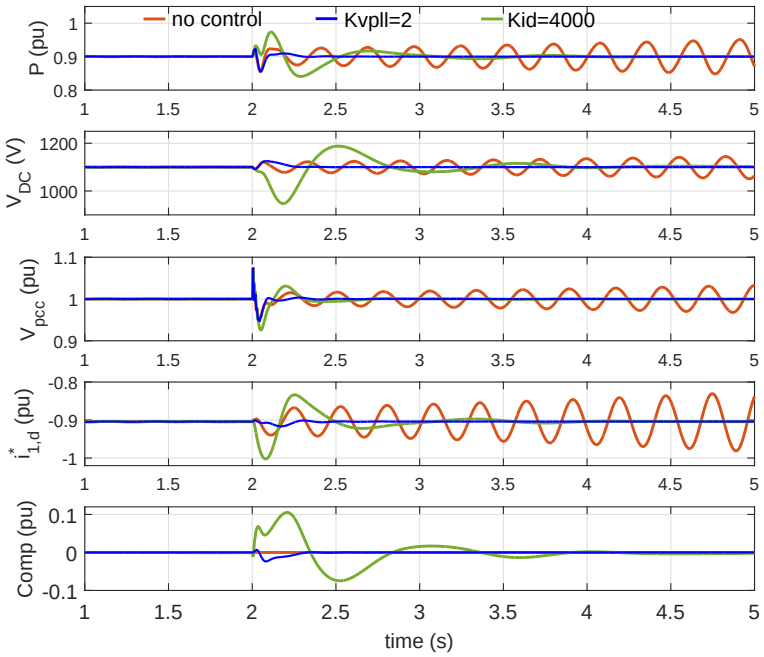

Figure 2.25: Type-4 wind testbed simulation results with $X_g : 0.5 \rightarrow 0.61$ at 2 sec. Red line: no control; Blue line: voltage-based control ($K_{id} = 0$, $K_{vpll} = 2$); Green line: current-based control ($K_{id} = 4000$, $K_{vpll} = 0$).

2.6 Implementing Stability Control in Hardware Testbed

To validate the performance of the stability control, a LabVIEW-based laboratory hardware testbed is built based on a grid-connected VSC system with the vector control. The detailed procedures on how to build this hardware testbed and experiment results will be presented in these sections.

2.6.1 Configuration of Laboratorial Testbed

The topology of the hardware testbed is shown in Fig. 2.28. The hardware testbed includes two voltage sources, one three-phase DC/AC inverter, and two passive circuits (the LC filters and transmission lines). All devices and components are at the laboratory level. One of the voltage source is a regulated DC voltage supply which supplies the 40V DC voltage at the DC side of the inverter. Another voltage source is a balanced three-phase 60-Hz AC voltage source and it is

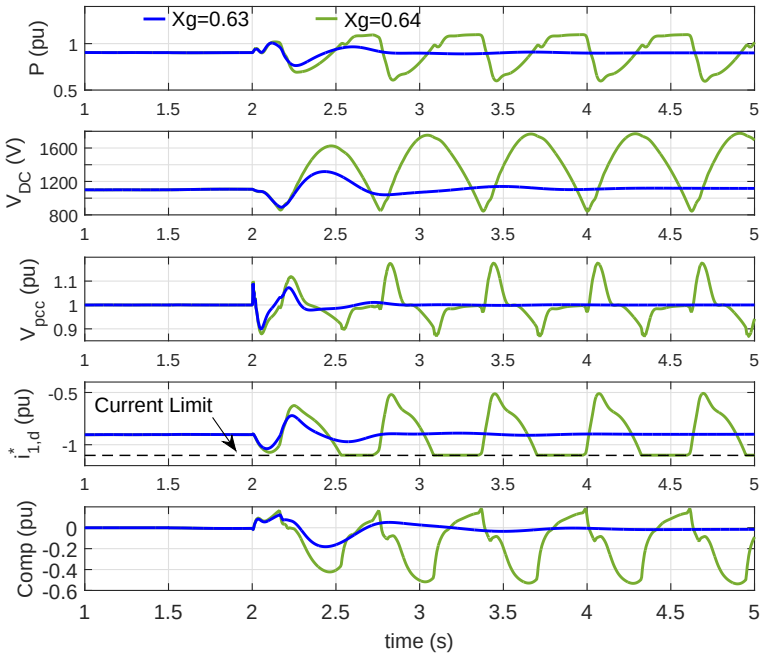

Figure 2.26: Type-4 wind testbed simulation results with $K_{id} = 4000$. $X_g : 0.5 \rightarrow 0.63$ (blue line), $X_g : 0.5 \rightarrow 0.64$ (green line).

used as the main grid whose RMS value of line-to-line voltage is 14.7 V. The three-phase DC/AC inverter contains two IGBTs on each phase. The PWM signals for the inverter are generated by an FPGA-based controller. The details of the control strategy which is programmed on the controller will be introduced in the next section.

Two passive parts are the three single-phase LC filters and three single-phase inductive transmission lines. The LC filters are used between the inverter and the PCC bus to filter the harmonics which are generated by the inverter. A single-phase LC filter contains four inductors, one capacitor (47μ F), and the resistance of the wire (0.5Ω). Four 5.6 mH inductors are connected like the way shown in Fig. 2.28 to extend the current limitation of the filter but the total inductance of each filter (L_1) is still 5.6 mH. From the PCC bus to the grid, there are three single-phase transmission lines that consist of multiple same-size inductors connected in series. Hence, the length of the transmission lines can be determined by the number of inductors and the total inductance is represented by L_g. The resistance of each transmission line (R_g) is from two wires used for the

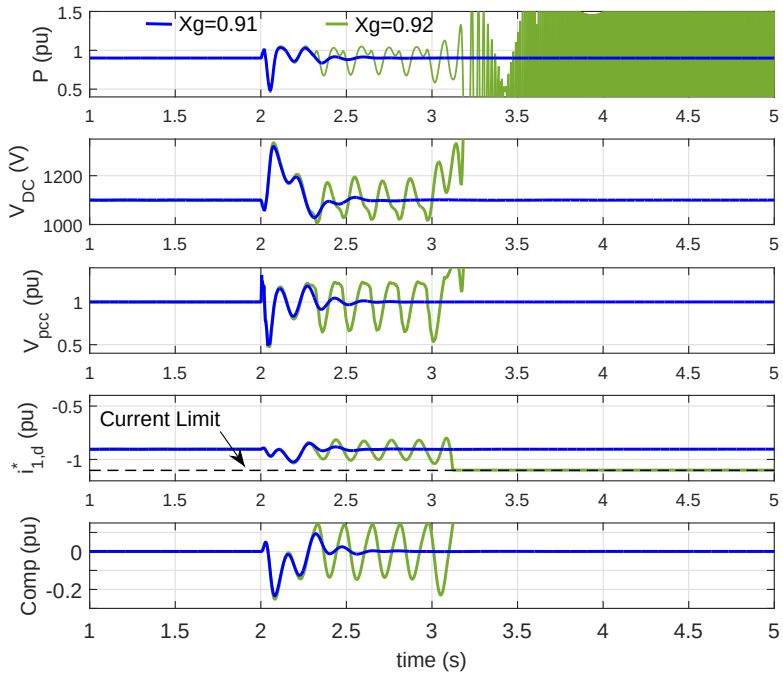

Figure 2.27: Type-4 wind testbed simulation results with $K_{vpll} = 2$. $X_g : 0.5 \rightarrow 0.63$ (blue line), $X_g : 0.5 \rightarrow 0.64$ (green line).

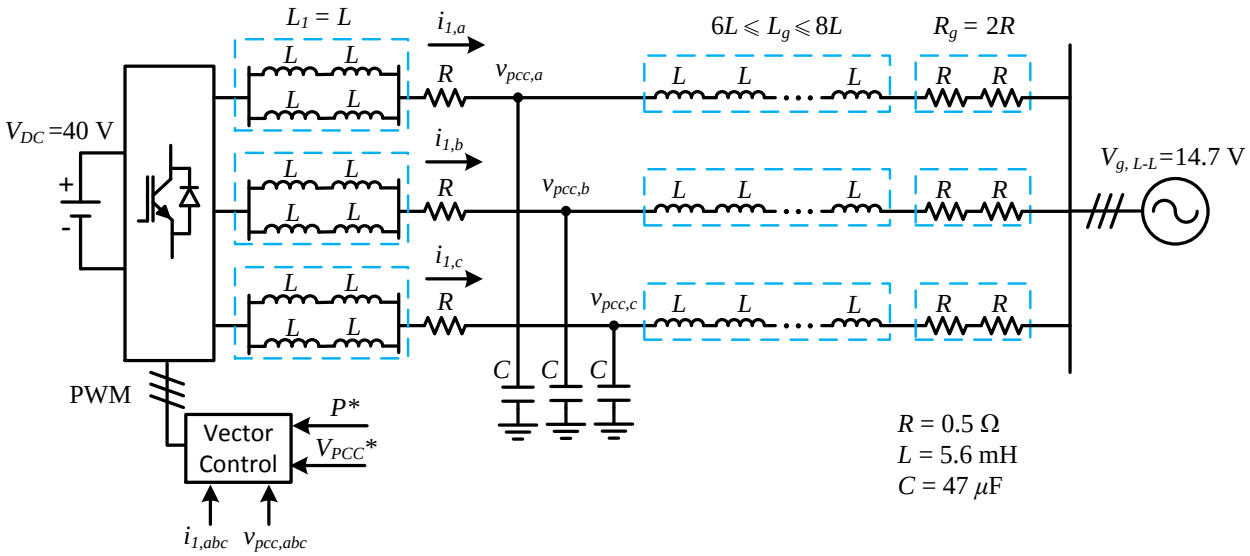

Figure 2.28: Topology of the hardware testbed.

connections. The parameters used in the hardware testbed and the corresponding per-unit analysis used for the analytical model are listed in Table 2.9.

Table 2.9: Parameters of experiment testbed

Parameter	Value (SI)	Per-unit (pu)
Rated power	20 W	1
DC-link voltage	40 V	
Rated voltage (p-p rms)	14.7 V	1
Nominal freq.	60 Hz	1
$L_1(X_1)$, R_1	5.6 mH, 0.5 Ω	0.195, 0.046
$C_1(B_1)$	47 μF	0.19
$L_g(X_g)$, R_g	33.6 – 44.8 mH, 1 Ω	1.17 – 1.56, 0.09
Current control		$K_{pi} = 0.4$, $K_{ii} = 4$
Power control		$K_{pp} = 0.4$, $K_{ip} = 40$
Voltage control		$K_{pv} = 0.2$, $K_{iv} = 20$
PLL		$K_{p\mathrm{PLL}} = 60$
		$K_{i\mathrm{PLL}} = 1400$

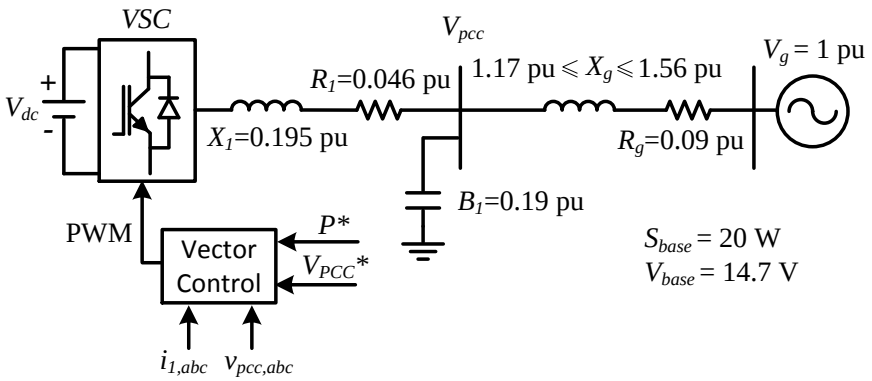

Figure 2.29: Topology of a grid-integrated VSC system.

The topology is shown in Fig. 2.28 and used to build the hardware testbed so the parameters are in physical units. To design the control system and investigate the performance, the per-unit analysis is preferred. First, the base power S_{base} and base voltage (V_{base}) need to be determined. Based on the current and voltage limitations of devices and elements, S_{base} is selected as 20 W while V_{base} is 14.7 V. Then, the per-unit analysis can be conducted based on the physical values in Fig. 2.28. By aggregating the passive element, the single-line diagram of the above system is shown in Fig. 2.29 including the per-unit values. X_1 and X_g represent the reactance in per-unit of the aggregation of multiple inductors. R_1 and R_g are the per-unit values of R and $2R$ respectively.

B_1 indicates how much reactive power in per-unit is generated by the three-phase capacitors. The linear analysis will be conducted based on this single-line diagram.

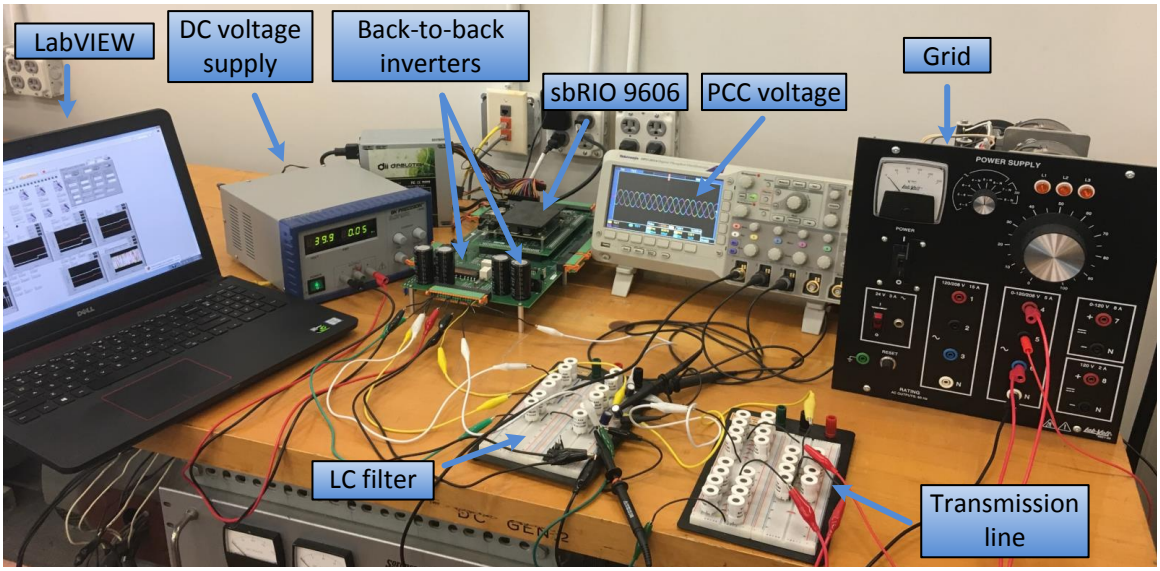

Figure 2.30: LabVIEW-based experiment testbed.

Fig. 2.30 is the picture of the physical hardware testbed which is built in our lab. All devices in this picture are labeled by the names corresponding to elements in Fig. 2.28. The dc voltage supply is Bk Precision 1666 whose voltage range is from $0-42$ V and the rated power is 200 W. Due to the design, it supplies the 40V DC voltage at the DC side of the inverter. The grid is emulated by a balanced three-phase 60-Hz AC voltage source (Lab-Vot 8821-20). Its voltage range is $0-120$ V and the maximum current is 5 A. In this testbed, its RMS value of line-to-line voltage is 14.7 V because of the determined V_{base}. Two circuits designed on the breadboards are the LC filter and the inductive transmission line respectively. Fig. 2.31 shows their details and the dashed blue lines circle the elements on each phase. We can find that connections are the same as Fig. 2.28.

The voltage source converter (VSC) with the vector control strategy was achieved by a three-phase back-to-back inverter research board. It actually includes three pieces. The lower piece is named as mini-scale SKiiP3 Replica Back-to-Back Converter and contains two embedded inverters (A and B). We used Inverter A as the VSC in the testbed. Each inverter has three voltage sensors and three current sensors at the converter side. Hence, the current sensors of Inverter A are used

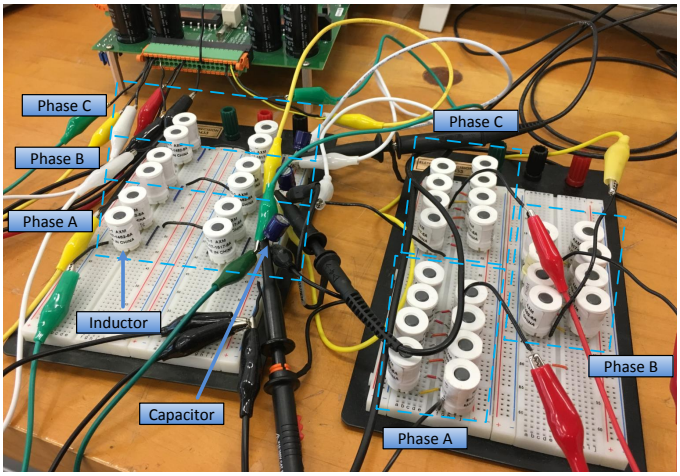

Figure 2.31: The passive components (LC filter and transmission line) are designed on the breadboard.

to measure the converter currents while the voltage sensors of Inverter B are used to measure PCC bus voltage. The board also has the temperature protection to avoid burning with the embedded temperature sensors. The upper piece is the single-board RIO 9606 from NI including both FPGA-based digital controller and NI general purpose inverter controller (GPIC). They are used to control the inverters, sensors, and all the inputs and outputs on the lower piece. The controller can be programmed by NI application LabVIEW. It is installed in a host PC which is located at the left-most of Fig. 2.30. The communication between PC and sbRIO is Ethernet.

2.6.2 Vector Control Designed in LabVIEW

The control system for VSC is based on the P/V vector control. Due to the different functions, the control systems are divided into three different modules (loops). They are presented in the following figures. The module in Fig. 2.33 has the functions of the PLL and Park transformations. It synchronizes all the measurements with the PCC voltage and converts them from *abc* frame to *dq* frame. For the vector control, the PCC voltages and the converter currents in *dq* frame are required. The readings from the voltage and current sensors are in physical units, V_{u_B}, V_{v_B}, V_{w_B}, I_{u_A}, I_{v_A}, and I_{w_A}. As the aforementioned, the voltage sensors of Inverter B are used to measure PCC voltages while current sensors of Inverter A are used to measure the converter current. Before any

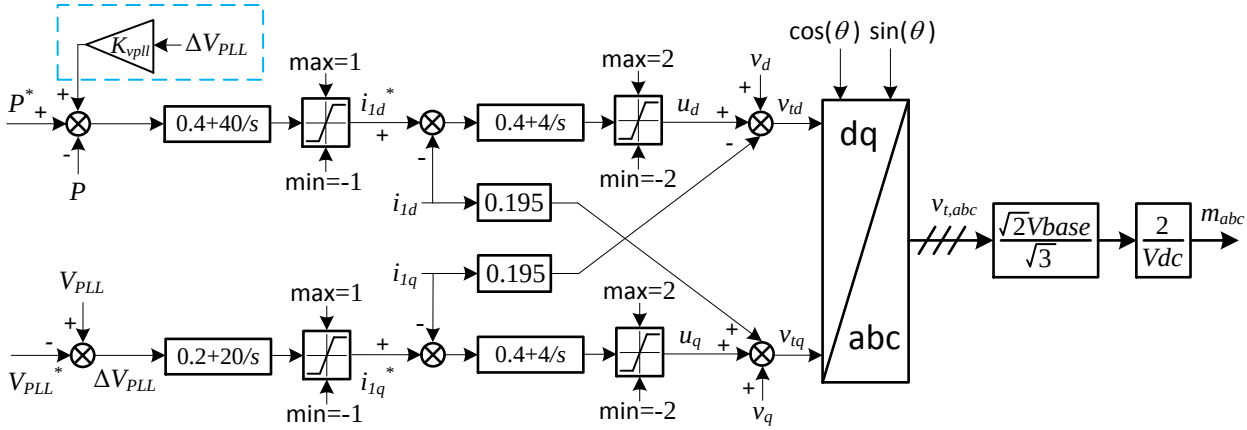

Figure 2.32: The module of the stability control.

calculation and transformation, all required measurements need to be converted to per-unit values $v_{pcc.abc}$ and $i_{1,abc}$. The scaling gains are $\frac{\sqrt{3}}{\sqrt{2}V_{base}}$ and $\frac{\sqrt{3}V_{base}}{\sqrt{2}S_{base}}$ for the voltage and current respectively. Fig. 2.34 shows the detailed structure of PLL in the testbed. Then, two synchronization signals $\cos(\theta)$ and $\sin(\theta)$ from PLL are used for Park transformation. In this control system, the dq frame is $d+jq$. After obtaining the dq components of the PCC voltage and converter current, we can use them to calculate the power measurement and the magnitude of PCC voltage.

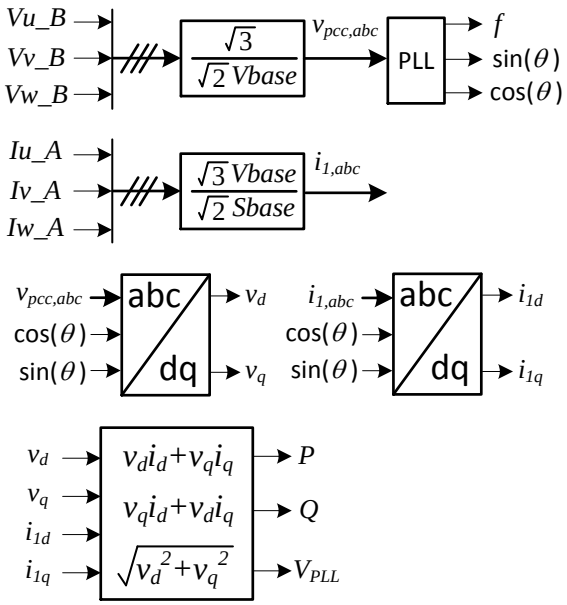

Figure 2.33: The module of PLL and frame transformations.

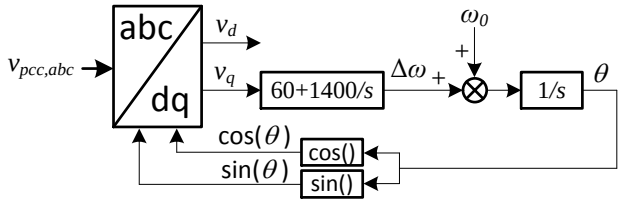

Figure 2.34: Structure of phase-locked-loop.

Fig. 2.32 shows the power order vector control including the outer loop, inner loop with decoupling and feedforward. The saturations are added to protect the power electronic device from over current. The values are selected based on the demo of MATLAB named as *400-kW Grid-connected PV Famr*. In the outer loop, the deviation of the magnitude of PCC voltage is supplemented to the power measurement through the feedback gain, K_{vpll}. The stability control and conventional power order control can be switched by changing the value of K_{vpll}. When $K_{vpll} = 0$, the vector control is conventional. Otherwise, the stability control is activated. To generate the three-phase control voltages m_{abc}, the converter voltages v_t needs to be converted from the dq frame to abc frame. Then, the gain $\frac{\sqrt{2}V_{base}}{3}\frac{2}{V_{dc}}$ is require to scale down $v_{t,abc}$.

Fig. 2.35 shows the module which generates Pulse Width Modulation (PWM) signals and sends them to the switches of Inverter A directly. Compared with the above two modules, the module for the PMW-signal generator has a higher iteration rate because it is FPGA-based and uses the clock of the FPGA controller (40 MHz). The three-phase control voltages m_{abc} are from Fig. 2.32 and the carrier frequency is set at 4 kHz. Hence, the switching frequency is 4 kHz.

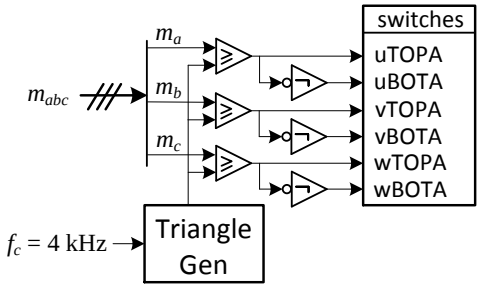

Figure 2.35: 40 MHz FPGA-based module of PWM-signal generator.

2.6.3 Experiment Results on Conventional Control

We implement the above vector control in the hardware testbed and investigate its performance. The control parameters of the hardware testbed are the same as Fig. 2.32. Because the event of the tripping line cannot be implemented in our hardware testbed, the step changes in the following cases were increments of the power transfer level. Hence, the performance of the control is determined by the power transfer level of the system with the specific length of the transmission line. In this section, the six-inductors transmission line was used ($X_g = 1.17$ pu). During the experiments, the dynamic responses of real power generated by VSC, converter current in d-axis, and PCC voltage magnitude were monitored. The experimental results were plotted by MATLAB using the data exported from LabVIEW GUI which is shown in Fig. 2.36. In LabVIEW GUI, we cannot only change the information of control systems but also monitor the dynamics of different measurements.

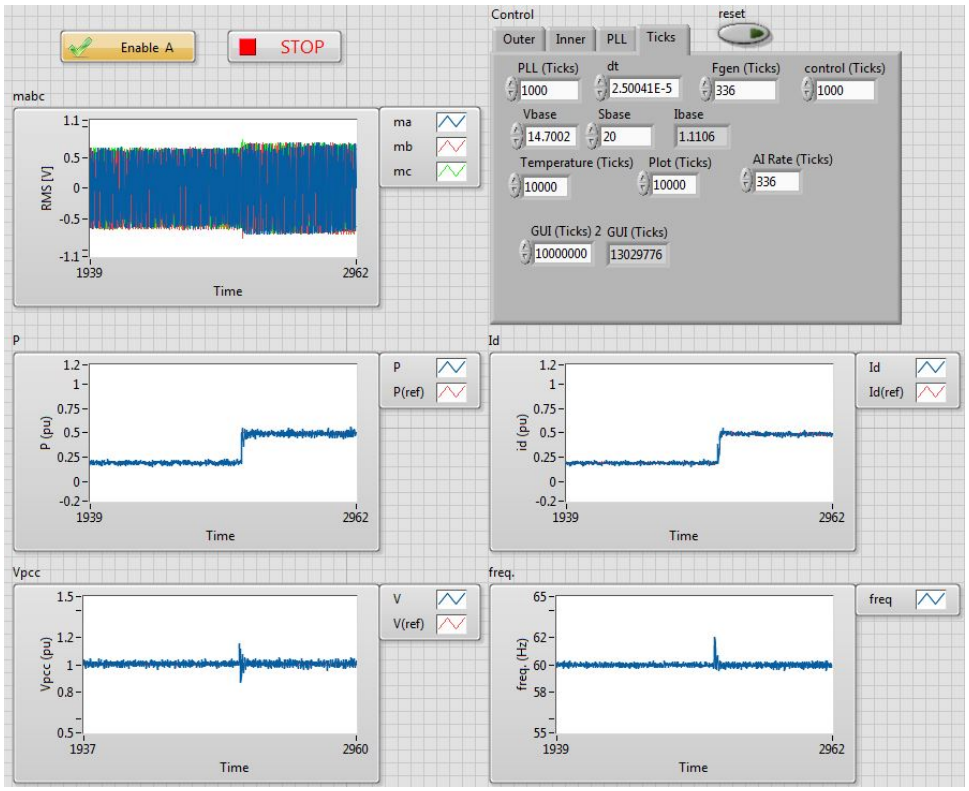

Figure 2.36: Overall of LabVIEW GUI.

To find the power transfer capability of this VSC-based system, the power reference P^* was increased from 0.2 pu to the higher power conditions at 5 sec. Then, we found the marginal unstable condition happened when P^* was increased from 0.2 pu to 0.65 pu. Hence, two conditions of $P^* = 0.60$ and $P^* = 0.65$ pu were selected and the corresponding experiment results were plotted in Fig. 2.37. The blue lines represent the measurements for the case of $P = 0.60$ pu while the red lines are for the case of $P = 0.65$ pu. It is observed that the system returned to be stable after P was increased to 0.60 pu while it became unstable after P was increased to 0.65 pu. Based on the oscillation waves in Fig. 2.37, the oscillation frequency was 3.8 Hz.

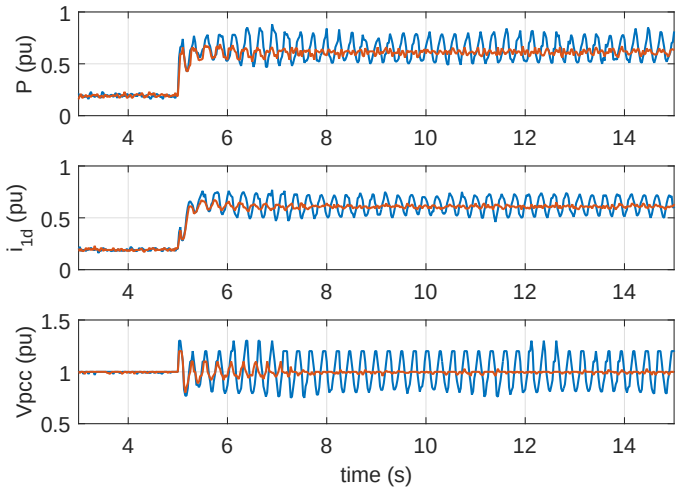

Figure 2.37: With the conventional control, the transferred power level of the system was increased from 0.2 pu to 0.60 pu (red lines) and 0.65 pu (blue lines).

The oscilloscope was used to monitor the three-phase instantaneous voltages at the PCC bus. Fig. 2.38 shows the transient dynamics of V_{pcc} when the power transfer level was changed from 0.2 pu to 0.65 pu. The low-frequency oscillations were observed in V_{pcc}.

The eigenvalue loci are also generated from the analytical model to match the experiment results. It cannot only be used to validate the margin conditions but also to validate the oscillation frequency. The analytical model is based on the per-unit analysis of the hardware testbed. Hence, the topology of the analytical model is based on the one-line diagram shown in Fig. 2.29. One VSC with power order vector control is connected to the infinite bus. In addition, the control parameters

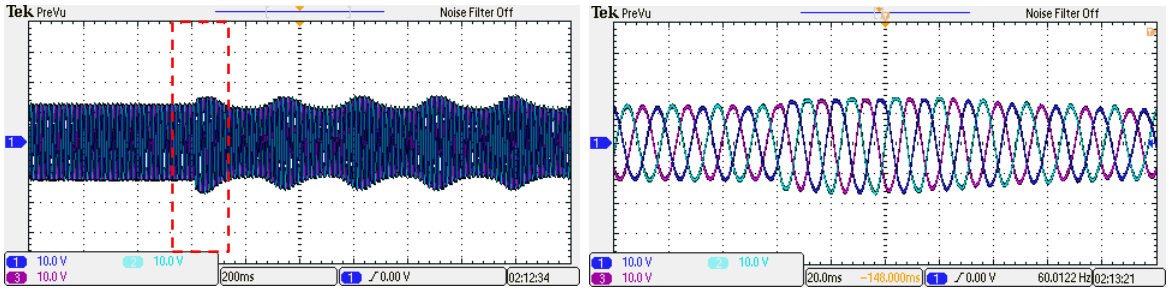

(a) (b)

Figure 2.38: Three-phase PCC voltage were shown in oscilloscope for the system with the conventional control. (2.38a): PCC voltages showed the instability after P was increased from 0.2 pu to 0.65 pu. (2.38b): zoom in to show the details.

are the same as the hardware testbed. Fig. 2.39 shows the eigenvalue loci which is generated based on the system with the conventional control.

With the six-inductors transmission line ($X_g = 1.17$ pu), the dominant mode moves to the right half-plane (RHP) with the real power P increased from 0.1 to 0.9 pu. The increment is 0.05 pu. According to Fig. 2.39, when P is larger than 0.64 pu, the low-frequency mode moves to the RHP. In other words, when the transferred real power is larger than 0.64 pu, the system will lose the stability and the oscillation around 4 Hz will appear. This conclusion matches the experiment results.

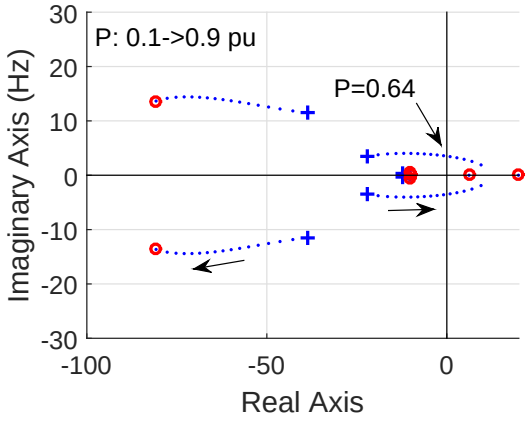

Figure 2.39: Eigenvalue loci: the power transfer level of the system with the conventional control is increased through a six-inductors transmission line ($X_g = 1.17$ pu).

2.6.4 Experiment Results on Stability Control

According to [29], there are two approaches to reduce the coupling between the PCC voltage and real power. One is adding the feedback of ΔV_{pll} to the real power. Another one is adding Δi_{1d} to the real power. The proportional gains are required between the feedback and the real power. Because [71] investigates that ΔV_{pll} has better performance than Δi_{1d}, this testbed only focuses on ΔV_{pll}. To validate its performance, the stability control was also implemented in the hardware testbed. The feedback part is circled by the dashed blue line in Fig. 2.32 and it can be activated by giving non-zero values to K_{vpll}. In this section, besides P, i_{1d}, and V_{pcc}, we also monitored the value of feedback gain K_{vpll} and the compensated power from the feedback control.

2.6.4.1 Six-inductors Transmission Line

How to select best values for K_{vpll} is discussed in [71]. The selection of K_{vpll} is the tradeoff between two modes. With the increment of K_{vpll}, one mode around 4 Hz moves to the left while another mode around 10 Hz moves to RHP. After the analysis, the best value of K_{vpll} should be equal to the power transfer level. Although a small K_{vpll} can improve the system stability, $K_{vpll} = P$ has a better performance. Hence, we designed two cases to investigate the different effects of $K_{vpll} = 0.2$ and $K_{vpll} = P^*$. Both cases had the same events. The power transfer level was increased from 0.2 pu to 0.65 pu at 5 sec and the stability control was activated at 10 sec by giving values to K_{vpll}. In Fig. 2.40, K_{vpll} was given by a constant value 0.2 and it can be presented by the first sub-plot. After the step change on P^* at 5 sec, the system became unstable with a 3.8 Hz oscillation. When the stability control was activated, the system returned to be stable after a short transient around 1.5 sec. In Fig. 2.41, K_{vpll} was equal to P^*. Before 10 sec, the system had the same dynamic responses as Fig. 2.40. However, the stability control with $K_{vpll} = P^*$ used less time to stabilize the system after it was activated at 10 sec. After comparing the dynamics after 10 sec in Fig. 2.40 and Fig. 2.41 , we can claim that the stability control with $K_{vpll} = P^*$ has the better performance.

To find how much the stability control with $K_{vpcc} = P^*$ can improve the system capability, the power transfer level was kept increasing. Then, it was found that when P was increased to 0.72

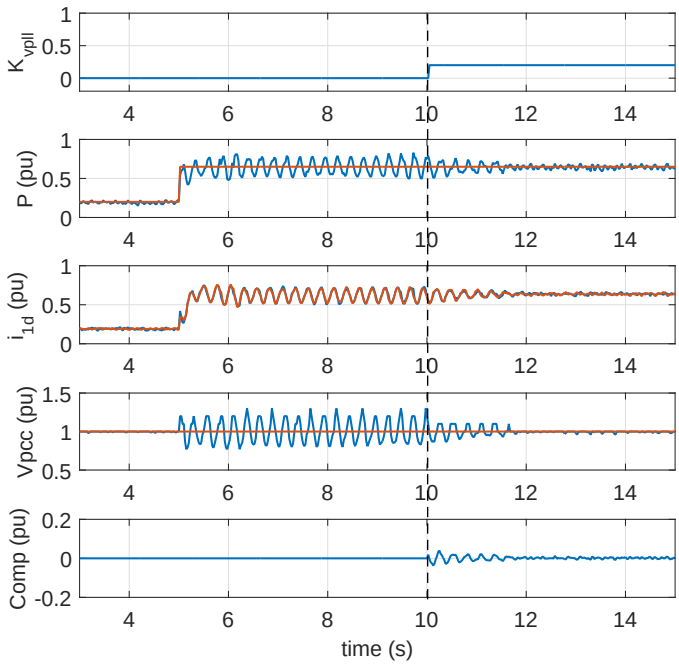

Figure 2.40: The power transfer level was increased from 0.2 pu to 0.65 pu at 5 sec; then, the stability control ($K_{vpll} = 0.2$) was activated at 10 sec. References (red lines); measurements (blue lines).

pu, the system kept stable with a short transient. However, when P was increased from 0.2 pu to 0.75 pu, the system lost the stability with the stable oscillations around 7.5 Hz. Fig. 2.42 show the corresponding dynamics of the system. The power transfer level was increased at 5 sec. The blue lines represent the measurements corresponding to $P = 0.72$ pu while the red lines are related to the case of $P = 0.75$ pu. After comparing Fig. 2.37 and Fig. 2.42, we found that the stability control with $K_{vpcc} = P^*$ can improve the power capability of the system by 15%.

To validate the experimental results with the six-inductors transmission line, two eigenvalues loci are generated for $K_{vpll} = 0.2$ and $K_{vpcc} = P^*$ respectively. Fig. 2.43a shows the movement of the dominant mode with the increase of the power transfer level when $K_{vpll} = 0.2$. The last condition of the dominant mode on the left half-plane (LHP) is $P = 0.69$. Compared with the margin condition ($P = 0.64$) of the conventional control, the stability control with $K_{vpll} = 0.2$ improves the power capability of the same VSC system by 8%. In 2.43b, K_{vpll} is variable and

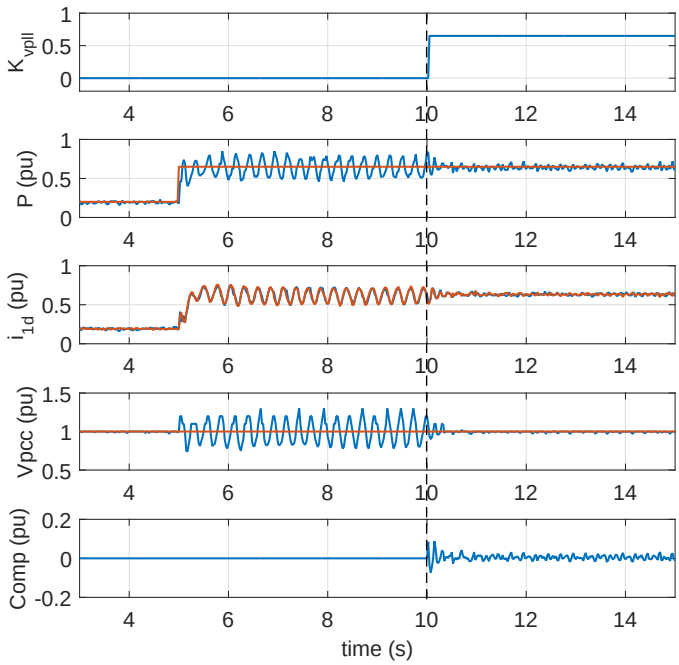

Figure 2.41: The power transfer level was increased from 0.2 pu to 0.65 pu at 5 sec; then, the stability control ($K_{vpll} = P^*$) was activated at 10 sec. References (red lines); measurements (blue lines).

equal to P^*. It is found that the new margin condition for the system with variable K_{vpll} becomes $P = 0.83$ pu. In other words, the stability control with $K_{vpll} = P^*$ improves the power capability by 29%. Therefore, it validates that the stability control with $K_{vpll} = P^*$ has a better performance than it with $K_{vpll} = 0.2$. In addition, with $K_{vpll} = P^*$, the dominant mode has the 7.5 Hz oscillation frequency which is higher than 3.8 Hz in conventional control.

Compared with the analytical model, the hardware testbeds have more noise which is caused by the switching dynamics and the sensors. Therefore, the larger K_{vpll} will also bring more noise from the voltage measurement to the power measurement. The large noise will reduce the performance of the stability control. Hence, stability control is able to improve the power capability of the hardware testbed but its performance is not good as the analysis results shown in Fig. 2.43b.

Besides P, the length of the transmission line X_g is another factor to cause the weak grid. To investigate the performance of the stability control on different X_g, the eigenvalue loci is generated

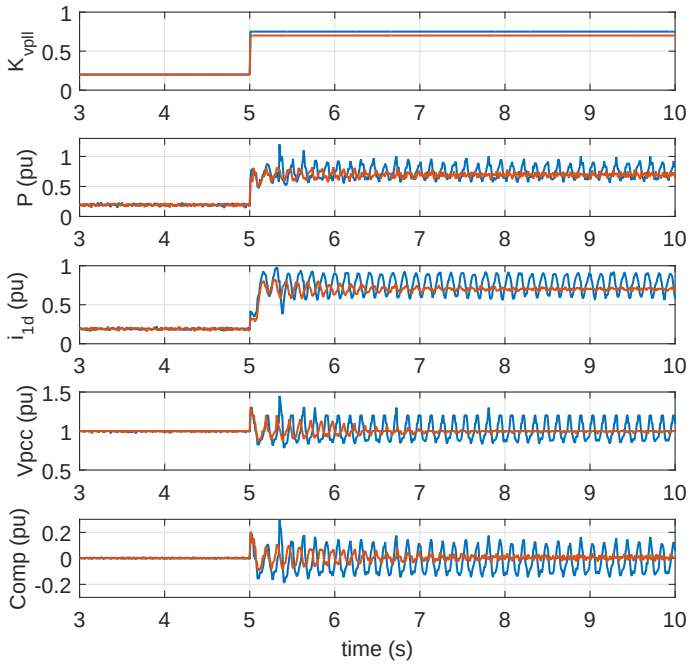

Figure 2.42: With the stability control, the transferred power level of the system was increased from 0.2 pu to 0.72 pu (red lines) and 0.75 pu (blue lines).

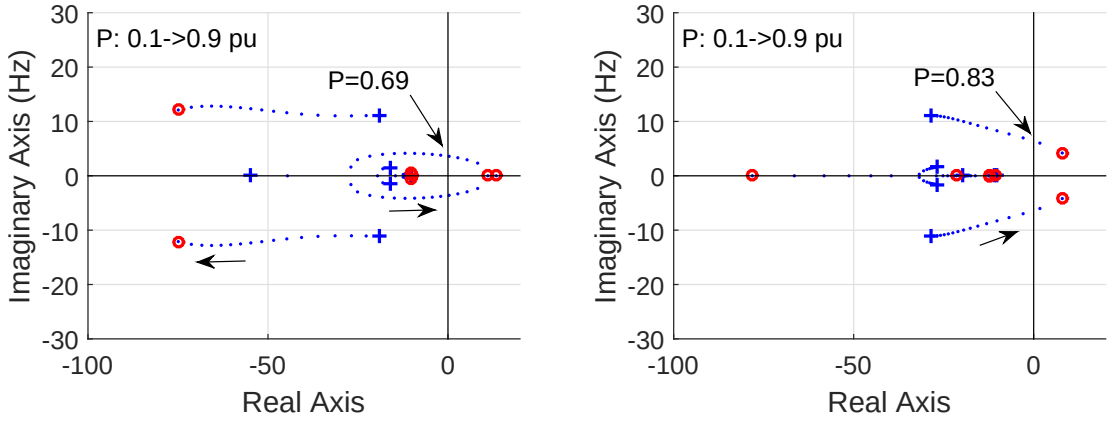

(a) (b)

Figure 2.43: Eigenvalue loci: the power transfer level of the system with $K_{vpll} = 0.2$ is increased for the six-inductors transmission line. (2.43a): stability control with $K_{vpll} = 0.2$. (2.43b): stability control with $K_{vpll} = P^*$.

by increasing X_g. Fig. 2.44 shows the eigenvalue loci based on the system with $K_{vpll} = P^* = 0.65$. The analytical model is designed based on the hardware testbed so the per-unit value of X_g is

calculated based on the number of inductors used for the transmission line. The number of inductors on each phase is changed from 1 to 8 so the per-unit value of X_g is increased from 0.195 to 1.56 pu. Based on Fig. 2.44, the VSC with the stability control ($K_{vpll} = P^*$) can transfer 0.65 pu real power through seven inductors on each phase ($X_g = 1.37$ pu) while it cannot transfer it through eight inductors ($X_g = 1.56$ pu).

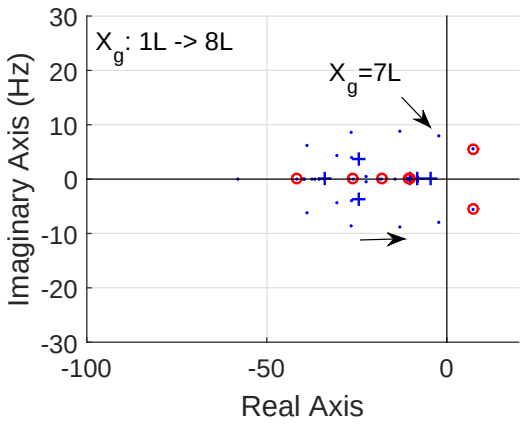

Figure 2.44: Eigenvalue loci with $P = K_{vpll} = 0.65$ pu while X_g increased.

The time-domain simulations were carried out to present the dynamic responses corresponding to Fig. 2.44. The initial condition is that $P^* = 0.65$ pu and $X_g = 1.17$ pu (six inductors). At 5 sec, the transmission line X_g was increased to 1.37 pu (seven inductors) and the time-variable dynamics were plotted by the red lines in Fig .2.45. Blue lines represent the dynamics when X_g is increased to 1.39 pu. The dynamics include the reactance of the transmission line, transferred real power, PCC bus voltage, and the output of the stability control (or compensation on P). It is noticed that the stability control ($K_{vpll} = P^* = 0.65$) was activated during the entire simulation time. Based on Fig. 2.45, the system with the stability control could transfer 0.65 pu power through $X_g = 1.37$ pu but it lost the stability even if X_g was increased by 0.02 pu. The time-domain simulation results matched with the eigenvalue analysis in Fig. 2.44.

2.6.4.2 Eight-inductors Transmission Line

The stability control was also tested for a longer transmission line. In this subsection, the length of the transmission line was increased by adding two more inductors. In other words, X_g

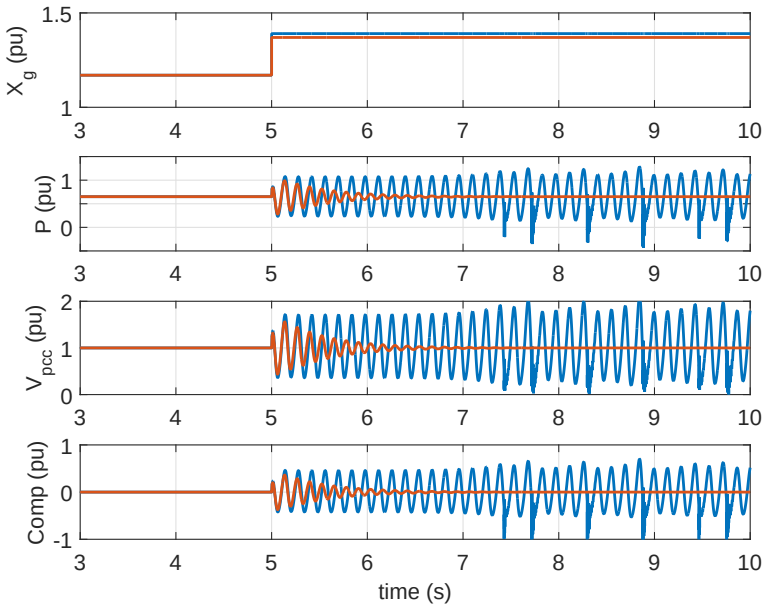

Figure 2.45: Time-variable results: the system with the stability control ($K_{vpll} = P^* = 0.65$). X_g was increased from 1.17 pu to 1.37 pu (red lines). X_g was increased from 1.17 pu to 1.39 pu (blue lines).

was increased from 1.17 pu to 1.56 pu. Through the eight-inductors transmission line, the power transfer level P^* of the system with conventional control was increased to find the margin condition. $P = 0.45$ pu was found as the margin condition of the system with conventional control. After that, P^* was increased from 0.2 pu to 0.46 pu at 5 sec. Then, the stability control was activated by giving 0.46 to K_{vpll} at 10 sec. The experiment results were plotted in Fig. 2.46. It is observed that the system returned to be stable quickly after the stability control was activated.

We kept increasing the power transfer level to check how much the stability control ($K_{vpll} = P^*$) can improve the system capability through the eight-inductors transmission line. Fig. 2.47 presents the experiment results at the marginal stable condition and marginal unstable condition of the system with $K_{vpll} = P^*$. The red lines indicated the measurements for P^* increased from 0.2 pu to 0.6 pu. After the step change at 5 sec, the oscillations appeared in the dynamic responses but its magnitude became smaller. It means that the system was around the marginal condition but it still could return to be stable. The blues lines represented the dynamics for P^* increased from 0.2

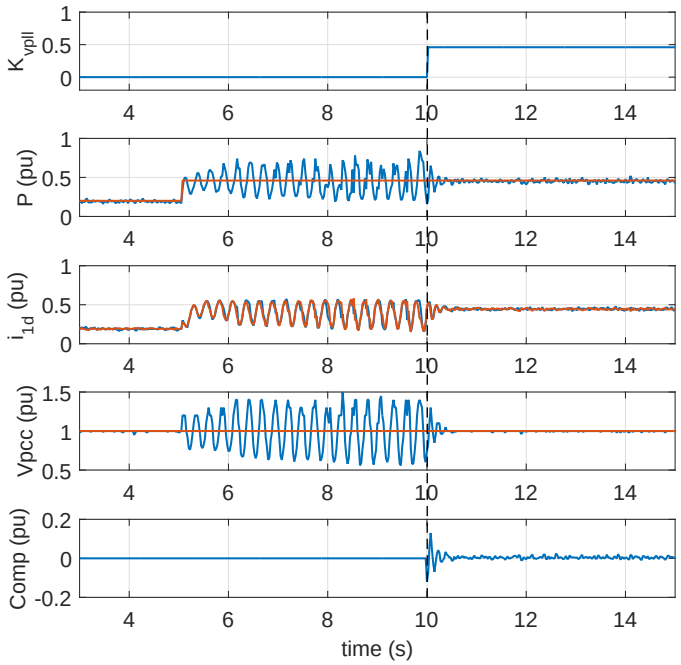

Figure 2.46: The power transfer level was increased from 0.2 pu to 0.46 pu at 5 sec; then, the stability control ($K_{vpll} = P^*$) was activated at 10 sec. References (red lines); measurements (blue lines).

pu to 0.62 pu. They illustrated that the system became unstable when the power reached 0.62 pu because of the large oscillations.

The eigenvalue loci for the eight-inductor transmission line are also generated and plotted in Fig. 2.48. Fig. 2.48a illustrates that $P = 0.45$ pu is the margin condition for the system without stability control. Fig. 2.48a indicates that with stability control, the margin condition can be increased to 0.6 pu.

2.7 Conclusion

Two real-world events in China and Texas are used to start the investigations on the stability issues of RES in the weak grid. Using the aggregated single-converter analytical models, the eigenvalue analysis is generated to show the effects of SRF-PLL dynamics and lead/lag PLL dynamics on the type of oscillation mode of RES in the weak grid. Based on the eigenvalue loci, both low-

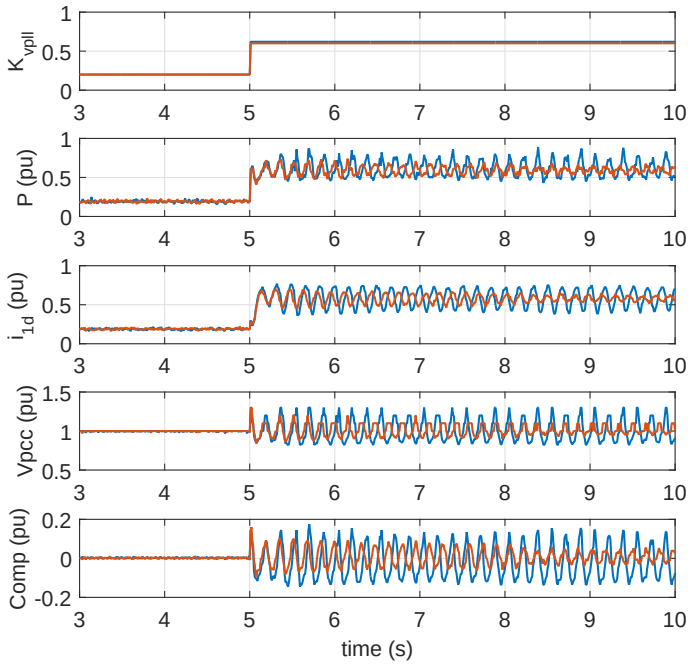

Figure 2.47: With the stability control, the power transfer level of the system was increased from 0.2 pu to 0.6 pu (red lines) and 0.62 pu (blue lines).

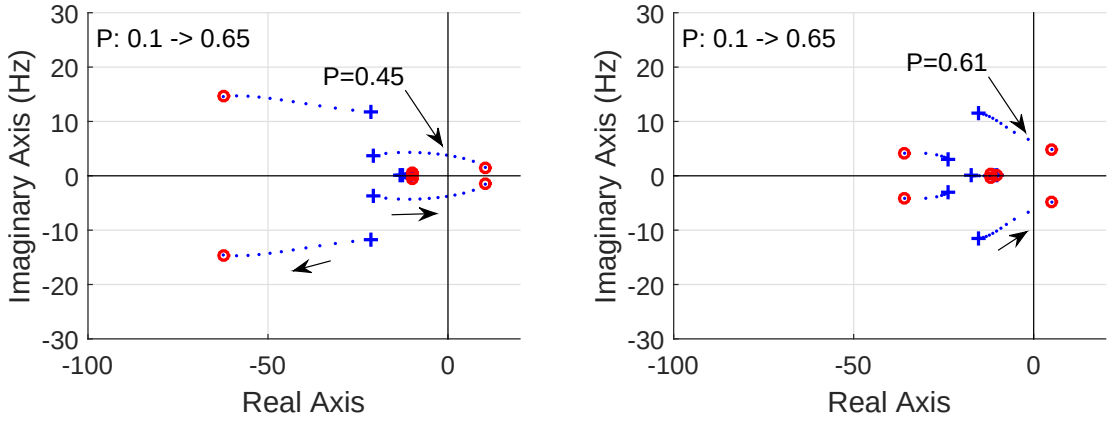

(a) (b)

Figure 2.48: Eigenvalue loci: the power transfer level of the system is increased for the eight-inductors transmission line. (2.48a): with the conventional control. (2.48b): with the stability control ($K_{vpll} = P^*$).

frequency oscillation mode and subsynchronous oscillation mode will move to the RHP when the grid strength is reduced. Which mode becomes dominant is dependent on the dynamics of PLL.

This finding is also validated by the simulation results from the EMT testbed with the full dynamics. Meanwhile, the torsional interaction between Type-4 wind and the remote synchronous generator is successfully demonstrated using the same testbed. It is verified that the subsynchronous oscillation can excite the torsional interactions if its frequency is close to a torsional mode of the synchronous generator.

Furthermore, stability control with two different strategies is analyzed and validated in this chapter. Two stability control strategies are implemented in two analytical models with two control modes respectively. Based on the eigenvalue analysis, we do not only evaluate the performance of each control strategy but also find the most suitable values for the feedback gains. To test the performance of stability control, we built up two EMT testbeds and one FGPA-based hardware testbed. The simulation results from two EMT testbeds verified that the voltage-based control strategy has better performance than the current-based control strategy. The stability control with the voltage-based strategy can significantly improve operating margins for both Type-3 and Type-4 wind. To obtain more practical validation, the stability control with the voltage-based strategy was implemented in the hardware testbed. The experiment results also showed that the stability control brought the significant improvement on the stability of RES in the weak grid.

Chapter 3: Single-inverter Aggregated Modeling of RES in Series Compensated Networks

3.1 Introduction

As aforementioned in Chapter 1, the stability issue in series compensated networks is different than the weak grid. Although [30] shows that Type-4 wind can be affected by the stability issues which are caused by the series compensated networks, most of the reported real-world events related to this kind of issue happened in Type-3 wind [33, 43, 63]. Therefore, this chapter [2] will focus on the modeling of Type-3 wind in series compensated networks. The main objective is to explore which factor or factors caused the different consequences in three SSR events in Texas in 2017. This chapter will not only replicate the real-world SSR events in Texas but also implement a practical control to mitigate SSR in the testbed. The detailed procedures on how to determine the accurate parameters in the real-world system will be introduced and the sensitivity analysis of two unknown factors will be produced.

3.2 Testbed Parameter Configuration

Before showing the replication results, I will introduce the procedures of EMT testbed configuration. The structure of the testbed can be found easily because the topology of the real transmission system was provided in [36]. Based on the topology of the real system shown in [36], the structure of the EMT testbed is determined as shown in Fig. 3.1. The testbed has six 345 kV stations and three of them are interconnected with the wind farms. Two end stations of this transmission system are San Miguel and N Edinburg which are connected to the main grid. The grid is represented by infinite bus. The base power is 100 MVA and the base voltage is 345 kV.

[2] This chapter was published in IEEE Transactions on Power Delivery [79], 2019. Permission is included in Appendix A.

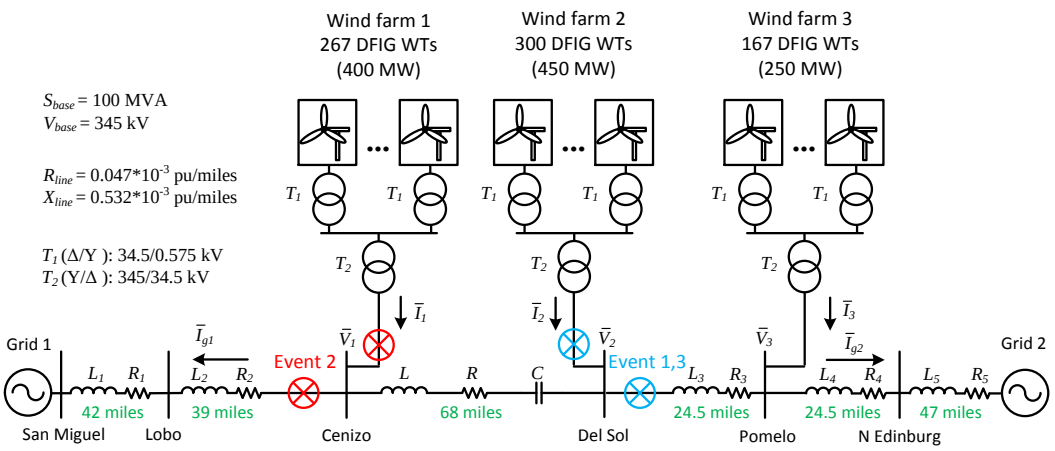

Figure 3.1: The testbed is built in MATLAB/SimPowerSystems for the replication.

3.2.1 Transmission Line Parameters

For transmission lines, their information was collected from several Electric Transmission Texas (EET) public project reports. In the report of Rio Grande Valley projects [80], the length of the transmission line from ETT's Lobo station to AEP's North Edinburg station is 156 miles.

In another report for Lower Rio Grande Valley Projects [81], this line was drawn on the map and four stations on that line were marked as well. The map can be found in [79]. Hence, the partial distance between every two stations can be estimated based on the map. The estimated lengths of transmission lines are 39 miles from Lobo station to Cenizo station, 49 miles from Del Sol station to N Edinburg station, and 68 miles from Cenizo station to Del Sol station. However, the Pomelo station between Del Sol station and N Edinburg was not marked in the map so it is assumed at the middle point. It means that L_3 is equal to L_4 if it is reflected in Fig. 3.1. In addition, there are two unknown distances because the parts out of Lobo station and N Edinburg station were not provided on the map. The distance between San Miguel station and Lobo station is found to be 42 miles from another report. The distance between N Edinburg station and the main grid is determined as 47 miles by trial and error of Event 2 simulation in the section of sensitivity analysis.

As mentioned in [80], two series capacitors are installed between Cenizo and Del sol stations and their total reactance is 48 Ω. Based on the per-unit analysis, the compensation level of the

line between Lobo station to N Edinburg station is around 49% which is a reasonable value in the Texas grid.

For the sensitivity analysis, the per-unit analysis is required. The per-unit values of line impedance are calculated based on the parameters of transmission lines in the EMT testbed. The per-unit length resistance and reactance are from the lines in a demo of MATLAB named as *Wind Farm- DFIG Average Model*. They are 0.047×10^{-3} pu/mile and 0.532×10^{-3} pu/mile. They are provided in Fig. 3.1. The per-unit values and real values for the replicated system are summarized in Table 3.1 including the transmission lines and the transformers. As noted, the total resistance and reactance of T_1 are indicated by X_{T1} and R_{T1} for the entire wind farm.

Table 3.1: Parameters of transmission system

Parameter	Value (SI)	Per-unit (pu)
S_{base}	100 MW	
V_{base}	34.5 kV	
$L_{T1}(X_{T1}), R_{T1}$	31.6 μH, 1.2 mΩ	0.002, 0.0002
V_{base}	345 kV	
$L_{T2}(X_{T2}), R_{T2}$	3.16 mH, 0.12 Ω	0.002, 0.0002
$L(X_L), R, C(X_C)$	114 mH, 4.76 Ω, 55 μF	0.0362, 0.004, 0.041
$L_1(X_1), R_1$	69 mH, 2.26 Ω	0.022, 0.0019
$L_2(X_2), R_2$	66 mH, 2.26 Ω	0.021, 0.0019
$L_3(X_3), R_3$	41 mH, 1.43 Ω	0.013, 0.0012
$L_4(X_4), R_4$	41 mH, 1.43 Ω	0.013, 0.0012
$L_5(X_5), R_5$	79 mH, 2.63 Ω	0.025, 0.0022

3.2.2 Wind Farm Parameters

In the public project reports from utilities and manufacturers, only the names of those wind plants can be found. In [81], it is mentioned that two wind plants, Javelina I and II, are interconnected to Cenizo station. Two wind plants interconnected to Del Sol station are Los Vientos III and IV. [82] mentioned that the wind plants Los Mirasoles are interconnected to Pomelo station. Then, we searched their names in the public wind power database. In the database, we can find the detailed information of the specific wind plant including capacity, the number of wind turbines, and types. For example, the type of wind turbine in those wind farms is Type-3 DFIG and their

rated wind speeds are around 11 $\sim$ 12 m/s. For the capacities, the total power of wind plants Javelina I and II is 450 MW; the total power of wind plants Los Vientos III and IV is 400 MW; the total power of wind plants Los Mirasoles is 250 MW.

To simplify the structure, the wind plants interconnected at the same station are aggregated as one Type-3 wind. Information of wind turbines, such as parameters and control systems, is confidential from each manufacturer. Thus, the DFIG wind farm demo in MATLAB/SimPowerSystems is adopted by our EMT testbed. The Type-3 wind farm in that demo is aggregated as one DFIG wind turbine module which is built by the GE team based on their 1.5 MW wind turbine-generator. The detailed information of this DFIG module is reported in GE's paper [83]. This DFIG module has been widely used in research because this demo has 143 paper citations and 4 patent citations. Hence, it is believed that the demo uses realistic control systems, control parameters, and machine parameters. The DFIG module is the same as it used in the Type-3 testbed in the above chapter so it uses the same parameters in Table 2.5. Moreover, the total numbers of wind turbines on the three wind farms are computed to be 267, 300, and 167 respectively because the size of each GE DFIG wind turbine in that DFIG module is 1.5 MW.

3.3 Sensitivity Analysis

In the public reports, the information of transmission lines and wind farm capacities can be found. However, there is no report to provide the operating conditions during events such as the number of online wind turbines and wind speed. To investigate the effects of these two factors on the SSR stability, the sensitivity analysis on these two factors is conducted in this section using the eigenvalue loci and the time-domain simulation results. The eigenvalue loci are generated from the DFIG analytical model which was proposed in [63] while the time-domain simulation results are produced by this replication testbed. Event 1 is used to conduct the sensitivity analysis. In Event 1, only WF2 is radially connected to the RLC circuit after the line tripped so an analytical model is derived based on the WF2 connected to the equivalent RLC network. Real values and per-unit values are listed in Table 3.1 and Table 3.2. Based on the sensitivity analysis, the number of online wind turbines and wind speed will be tuned for each SSR event in the next section.

3.3.1 Number of Online Wind Turbines

WF2 suffers the SSR because it is radially connected to the RLC circuit after the line tripping. To analyze its sensitivity, the number of online wind turbines in WF2 is increased from 10 to 300 for the various scenarios. For all the scenarios, the wind speed is always kept at 7.5 m/s while the line between Del Sol station and Pomelo station is tripped at 1 sec. Fig. 3.2 shows the simulation results for four scenarios, WT# = 10, WT# = 50, WT# = 100, and WT# = 200. For each scenario, the upper plot shows the three-phase instantaneous currents of WF2 while the lower plot shows the FFT analysis on the phase a of this current. Based on FFT analysis, there are two components in all scenarios but the SSR magnitude is much larger than the nominal component except WT# = 10. It indicates that the system becomes less stable with more online wind turbines.

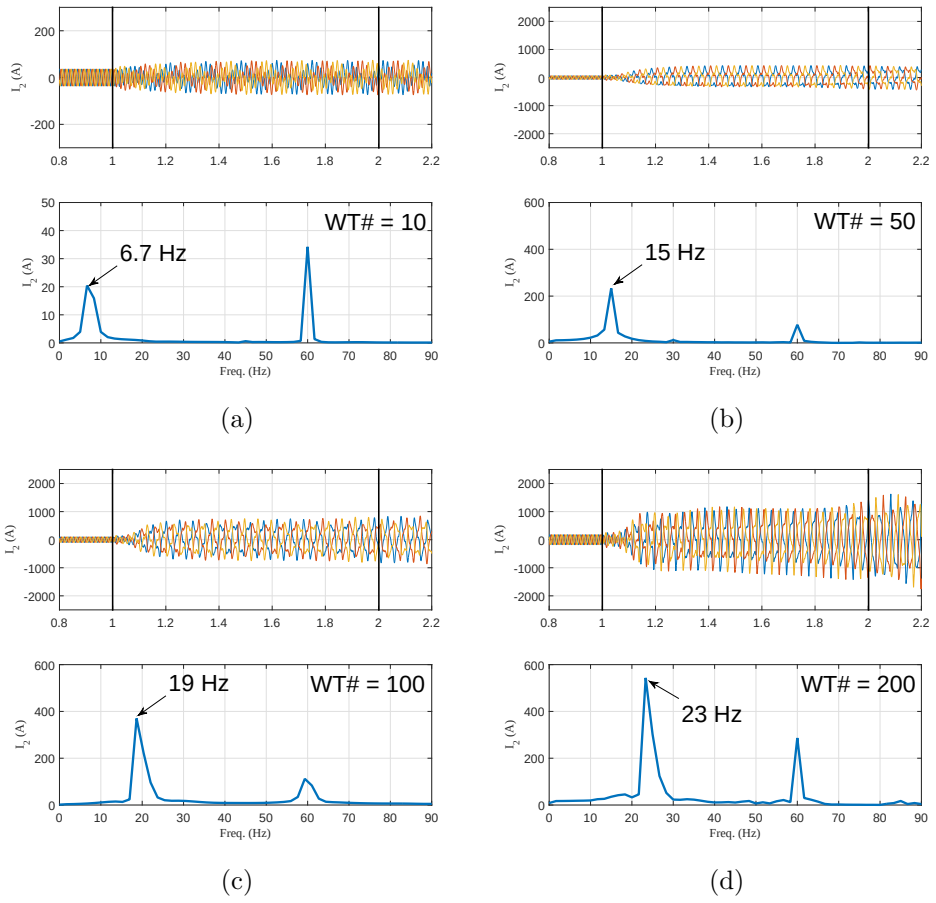

Figure 3.2: Effect of # of online wind turbines in WF2. (3.2a) 10 wind turbines; (3.2b) 50 wind turbines; (3.2c) 100 wind turbines; (3.2d) 200 wind turbines.

The corresponding SSR frequencies under seven scenarios are also concluded in Fig. 3.3 using bar plot. With WT # changed from 10 to 300, the SSR frequency is increased from 6.7 Hz to 26 Hz. Therefore, the larger number of online wind turbines will lead to a higher frequency of SSR and a less stable system.

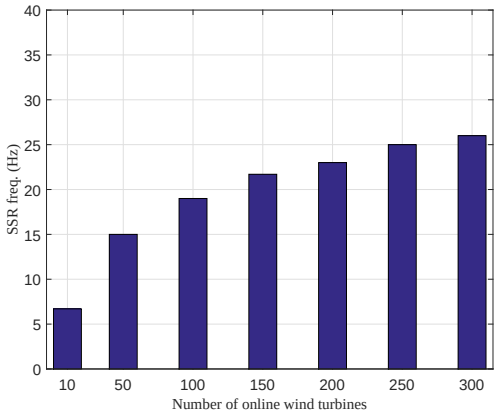

Figure 3.3: Effect of the number of online wind turbines on SSR frequency.

The eigenvalue loci with the change in the number of wind turbines is shown in Fig. 3.4. The first scenario is WT#=10 and the corresponding eigenvalues are marked by the sign of plus. The last scenario is WT#=300 and the corresponding eigenvalues are marked by the diamond. According to the dominant eigenvalue mode shown in 3.4b, the oscillation frequency is reduced from 53.5 to 34 Hz in *dq* frame with increasing the number of online wind turbines. In the *abc* frame, the oscillation frequency is changed from 6.5 Hz to 26 Hz. Therefore, the eigenvalue analysis matches the EMT simulation results shown in Fig. 3.3.

3.3.2 Wind Speed

Wind speed is one important factor to influence the wind power which is penetrated into the grid. The higher wind speed leads to more generated wind power but it also improves the SSR stability based on small-signal analysis in [63] and observation in real-world North China Type-3 wind farms [33]. In this subsection, wind speed is increased from 6 m/s to 12 m/s to generate its sensitivity analysis. It is assumed that all three wind farms have the same wind speed.

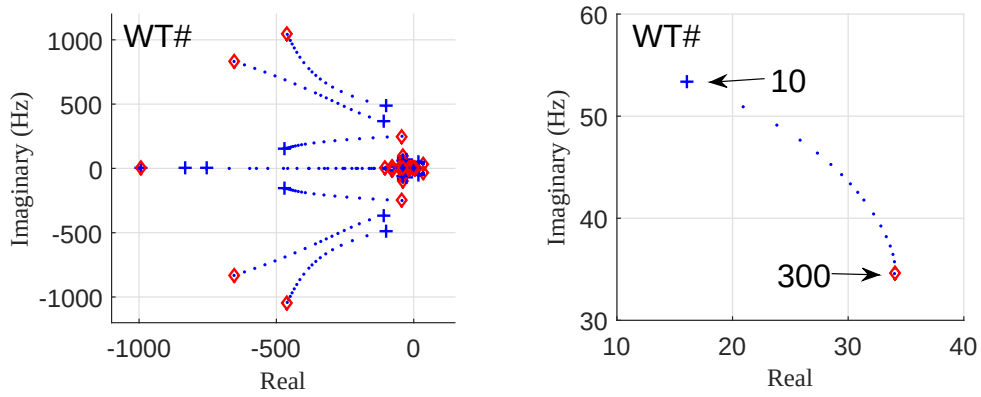

Figure 3.4: Eigenvalue loci with the number of online wind turbines changed from 10 to 300. (3.4a) shows the whole eigenvalue loci; (3.4b) zooms in dominant eigenvalues.

Fig. 3.7 shows the EMT simulation results for four different wind speeds and the corresponding FFT analysis. Based on the FFT analysis, the ratio of the SSR component to the nominal component becomes smaller with the wind speed increasing. In other words, the SSR stability of the system becomes better with the wind speed increasing. It is also reflected by the plots of instantaneous current. This fact can be used to explain that the different consequences of Event 1 and Event 3 are mainly due to different wind speeds.

Fig. 3.5 presents the SSR frequencies under different wind speed conditions. The frequency of SSR increases from 23.7 Hz to 30 Hz with wind speed increasing.

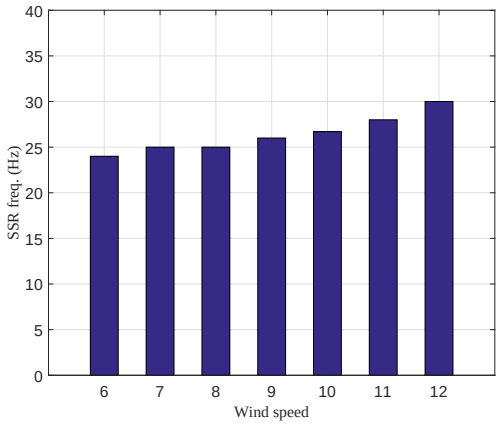

Figure 3.5: Effect of the wind speed on SSR frequency.

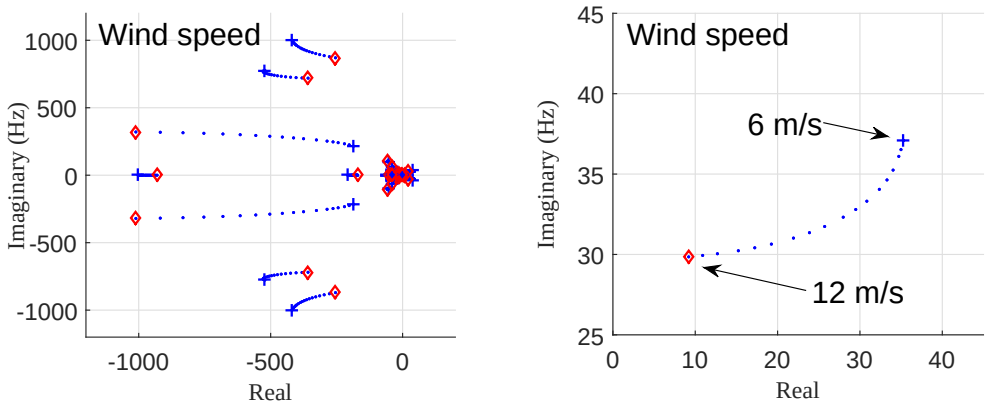

(a) (b)

Figure 3.6: Eigenvalue loci with the wind speed changed from 6 to 12 m/s. (3.6a) shows the whole eigenvalue loci; (3.6b) zooms in the dominant eigenvalues.

The corresponding eigenvalue loci is shown in Fig. 3.6. The eigenvalue moves with the increase of wind speed from 6 to 12 m/s. By focusing on the dominant mode shown in Fig. 3.6b, we can find that the oscillation frequency in *dq* frame is changed from 37 Hz to 30 Hz. It means that in the *abc* frame, the oscillation frequency is increased from 23 Hz to 30 Hz with the wind speed increasing. The eigenvalue loci also validated the bar plot shown in Fig. 3.5.

3.3.3 Grid Strength

Although the grid strength does not affect power penetration, it has effects on stability. The sensitivity analysis on the grid strength is also used to estimate the distance between the end stations to the main grid.

In this subsection, the length of the transmission line X_1 between Grid 1 and San Miguel station is changed from 0.022 pu to 0.062 pu for sensitivity analysis. The increment is 0.01 pu. The current dynamics under four conditions are presented in Fig. 3.8. The FFT spectrum shows that SSR keeps at 25 Hz with X_1 increasing. However, larger X_1 leads to a larger magnitude of the SSR component. In other words, the weaker grid causes the system to be less stable. It is noteworthy that the effect of increasing the number of online wind turbines is similar to the effect of reducing grid strength. Both lead to a less stable system.

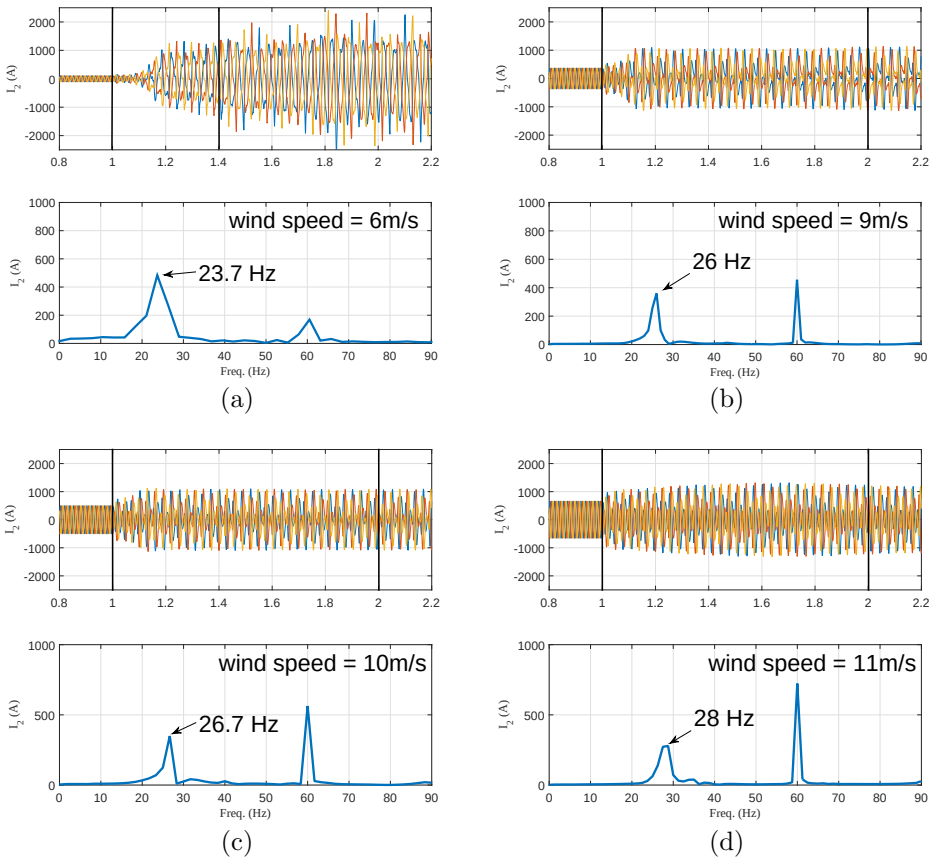

Figure 3.7: Effect of wind speed. (3.7a) 6 m/s; (3.7b) 8 m/s; (3.7c) 10 m/s; (3.7d) 11 m/s (rated).

3.4 Replications by Fine Tuning

The replication results were conducted by tuning the wind turbines online and wind speed through trial and error.

3.4.1 Location of Measurements

[36] presents the real-world records shown in Fig. 3.13 but it did not mention the location of the measurements. Before tuning those two factors, we need to determine where the measurements were recorded. First, it is assumed that all measurements were from the same location. Then, it can be determined that the location must be on the 345 kV lines because all the voltages were around 345 kV. Next, the measurements of the current are compared. Based on the current record

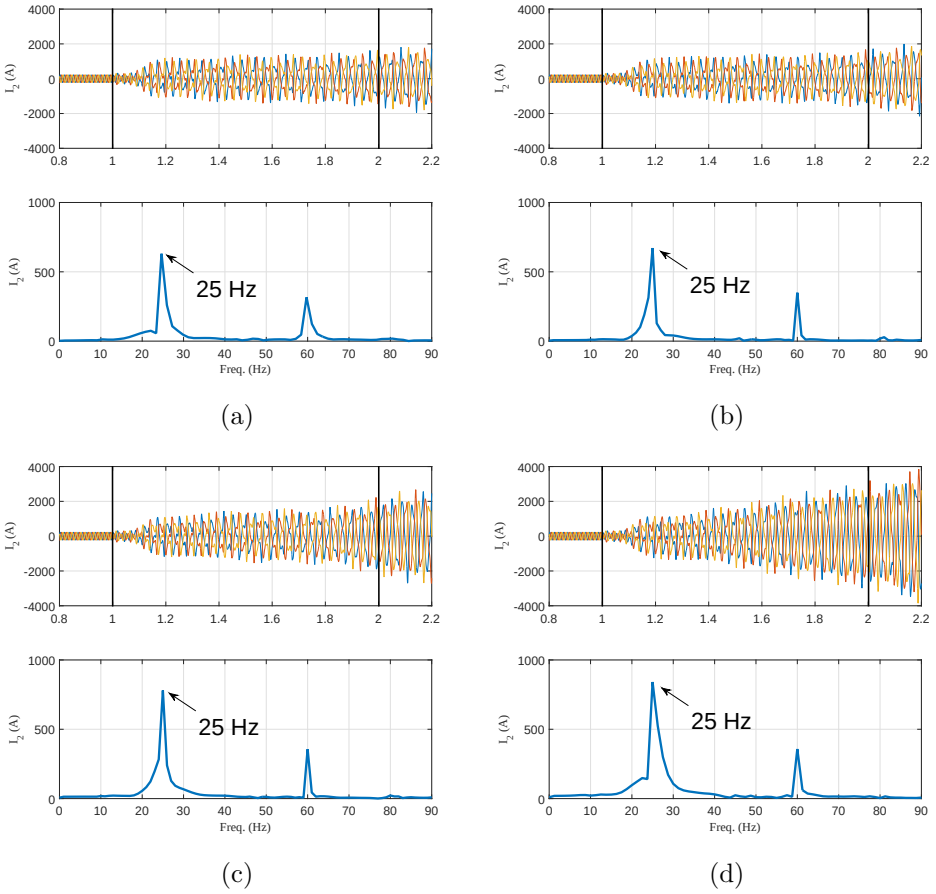

Figure 3.8: Effect of the grid strength. (3.8a) $X_1 = 0.032$ pu; (3.8b) $X_1 = 0.042$ pu; (3.8c) $X_1 = 0.052$ pu; (3.8d) $X_1 = 0.062$ pu.

in Event 1, the current became zero after WF2 tripped so the sensors should be installed at the side of WF2 or the RLC line. In Event 2, WF1 was radially connected to Grid 2 through the RLC line after Lobo to Cenizo line was tripped. However, the current record did not become zero after WF1 tripped so the sensors cannot be located on the RLC line. Hence, we assumed that the location of the measurement is at the output of WF2.

3.4.2 Fine Tuning

In this subsection, the detailed tuning procedure on the number of online wind turbines and wind speed is given. The tuning procedure is based on the sensitivity analysis in the above section. As noted again, the wind speed is assumed as the same for all wind farms.

In Event 1, WF2 is radially connected to the RLC circuit. Note that the total number of the wind turbines of WF2 is 300. We conducted experiments and found that SSR frequency has less to do with wind speed but more to do with the number of online wind turbines. Based on Event 1's SSR frequency (25.6 Hz), the number of online turbines of WF2 is tuned to be 250 through trial and error. Then the wind speed is tuned to be 7.5 m/s so that the magnitudes of the SSR component and the fundamental component can match the recorded data.

The same line was tripped in Event 1 and Event 3, which left WF2 radially connected to the RLC circuit. While the 60 Hz component of WF2 current is 340 A in Event 1, this number is 430 A in Event 3 according to the recorded data shown in Fig. 3.13. The increase in WF2 current is possibly due to the increase in wind speed or the number of wind turbines online. However, the system was more stable in Event 3. Small-signal analysis in [46] indicates that higher wind speed leads to a more stable system while the small-signal analysis in Fig. 3.2 indicates that more online wind turbines lead to a less stable system. Hence, we reasoned that the increase in WF2 current is due to wind speed increase rather than online wind turbine number increase. Once the wind speed is increased to be 10.5 m/s, the 60 Hz component's magnitude becomes much higher than 430 A while the SSR component's magnitude becomes less than 350 A (recorded data). We then reduce the number of online wind turbines in WF2 from 250 to 200 to match the 60 Hz component magnitude. This reduction also causes the SSR component magnitude getting further reduced. On the other hand, WF1 is not radially connected the RLC circuit. Increasing the power from WF1 will make the overall system more stable while decreasing the power from WF1 will make the overall system less stable. By reducing the number of wind turbines in WF1 from 267 to 200, the SSR component magnitude gets slightly increased to match 340 A.

In Event 2, WF1 iss radially connected to the RLC circuit and the SSR frequency is 22.5 Hz. Our experiments indicate that the number of online wind turbines influences the SSR frequency. More turbines lead to higher SSR frequency. If we assume all 267 turbines are online, the SSR frequency is 25 Hz. Reducing the number to 110 leads to a 22.5 Hz SSR component. Further, wind speed is tuned to be 7.9 m/s to match the SSR component magnitude (320 A). As the final

step, since the measured current is WF2 current and to match the 60 Hz fundamental component current at 230 A, the number of online turbines in WF2 is tuned to be 220.

Table 3.2: Parameters of wind farms (1.5 MW each turbine)

	Capacity (MW)	Total	Event 1	Event 2	Event 3
WF1 (#WTs)	400	267	267	110	200
WF2 (#WTs)	450	300	250	220	200
WF3 (#WTs)	250	167	167	167	167
Wind Speed (m/s)		11	7.5	7.9	10.5

Two basic rules for fine-tuning are concluded by the flowchart in Fig. 3.9. After giving initial values, the number of online wind turbines needs to be tuned to match SSR frequency. Then, tune the wind speed. These rules are based on the sensitivity analysis and focus on the oscillation frequency and the ratio of $(\frac{\hat{I}_{SSR}}{\hat{I}_0})$. $\hat{I}_{SSR}$ is the magnitude of SSR component on phase a of instantaneous current from WF2 based on the FFT analysis while $\hat{I}_0$ is the magnitude of the fundamental component.

Although their effects are slight and they are not used for all three events, some other rules are used. For example, the power in other wind farms will affect stability as well. In event 3, WF2 was mainly tuned but the number of online wind turbines in WF1 was tuned as well. Another example is tuning grid strength. Finally, the estimated values for the number of online wind turbines and wind speed in each event are summarized in Table 3.2.

3.5 Improved SSR Control

The SSR control was proposed in [46]. This dissertation will improve it and implemente it in this replication testbed. In [46], there were actually three approaches that were designed to mitigate SSR. After the comparison in [46], the series capacitor voltage ΔV_c has the best performance. Fig. 3.10 shows the topology of Type-3 wind connected to the series compensated line. The SSR control

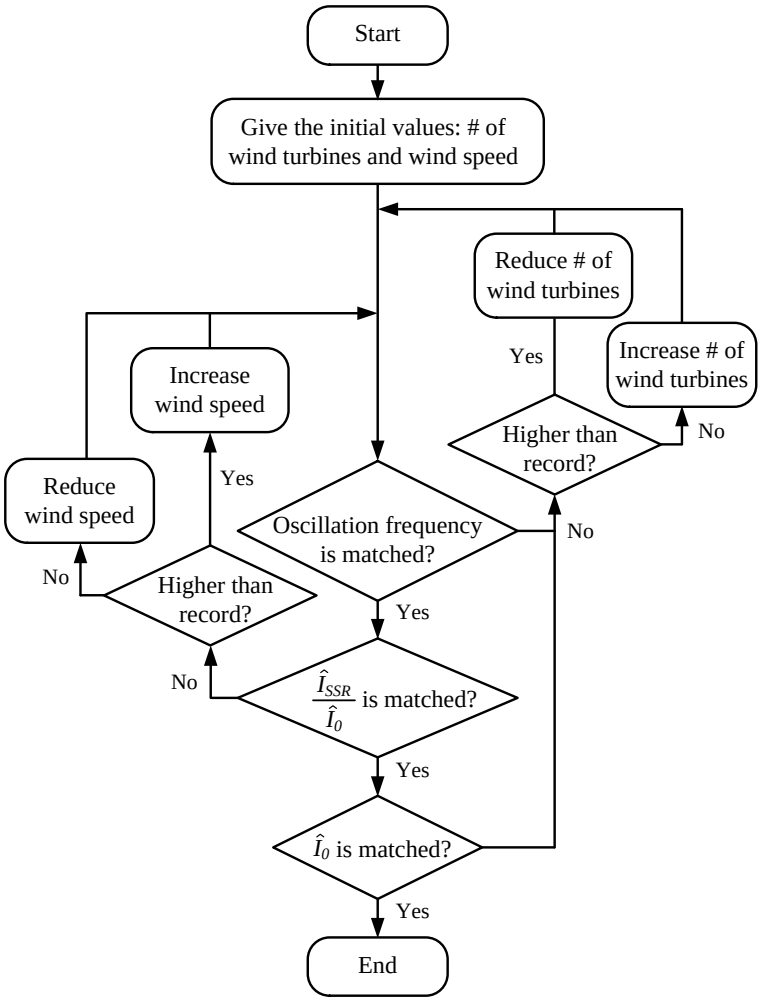

Figure 3.9: Flowchart on how to determine the number of wind turbines the wind speed by trial and error.

needs to be implemented in the control loop of GSC of Type-3 wind and it is marked by the blue dashed line in Fig. 3.10. Compared with Fig. 2.22a, the GSC with the SSR control requires one more signal, the three-phase currents through the series capacitor.

In the previous scheme of SSR control, the input of the supplementary part is ΔV_c. It is a remote signal for the wind farm so a long communication link needs to be established to transfer ΔV_c to the wind farm. [46] proposed to obtain ΔV_c using the wind farm current $i_{c,abc}$ to avoid the infrastructure cost because the current can be measured at the side of wind farm when it is radially connected to the series compensated line. Then, the capacitor voltages $v_{c,abc}$ can be estimated

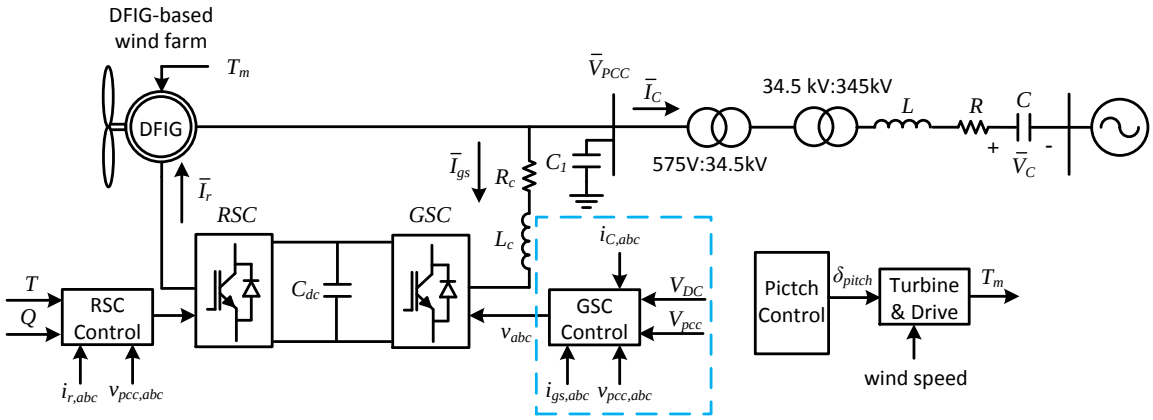

Figure 3.10: Topology of the Type-3 wind connected to the series compensated line with the SSR.

by integrating $i_{c,abc}$ based on the relationship between the three-phase voltages and currents in *abc*-frame (3.1).

$$C\frac{dv_{c,abc}}{dt} = i_{c,abc}, \;\; v_{c,abc} = \frac{1}{C}\int i_{c,abc} \tag{3.1}$$

In [46], this approach was discussed but not analyzed and tested by the simulation. The block diagram to generate the inputs of SSR control using $i_{c,abc}$ in [46] is shown in Fig. 3.11 for the comparison.

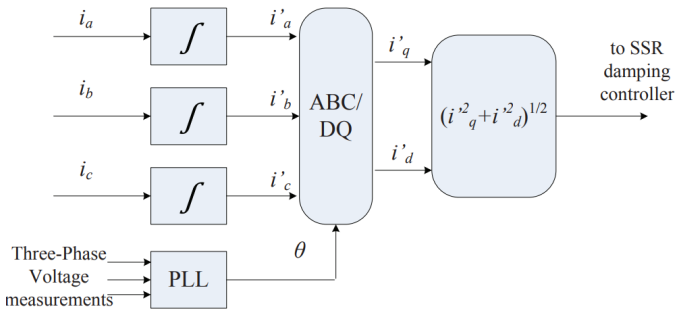

Figure 3.11: Block diagram to solve the remote signal issue. This figure is from [46]. Permission is included in Appendix A.

The improved control scheme of GSC is shown in Fig. 3.12 including the conventional vector control and the supplementary part for the SSR mitigation. The vector control of GSC employed in this testbed controls the dc-link voltage ($V_{\rm dc}$) and the PCC voltage ($V_{\rm pcc}$). The three-phase

currents are measured at the 575 V side of the transformer T_1 and sent to the integrator. The obtained signals then pass a high-pass filter ($\frac{0.1s}{1+0.1s}$) to get rid of the dc component. The signals are amplified with a gain $K_1 = 1.0757 \times 10^{-4}$ to have per unit values. The three-phase signals now emulate $v_{c,abc}$. Its magnitude V_c is computed after abc to dq transformation. To have only the deviation considered, another HPF is used to filter the constant values in V_C. The supplementary part of SSR control generates a modulation signal ΔV_{SSR} supplemented to the PCC voltage. A proportional gain K_{VC} is used to amplify the modulation signal. Hence, the value of K_{VC} has an effect on the performance of SSR control. Compared with Fig. 3.11, the improved SSR control has two more components, the high-pass filter (HPF) and K_1.

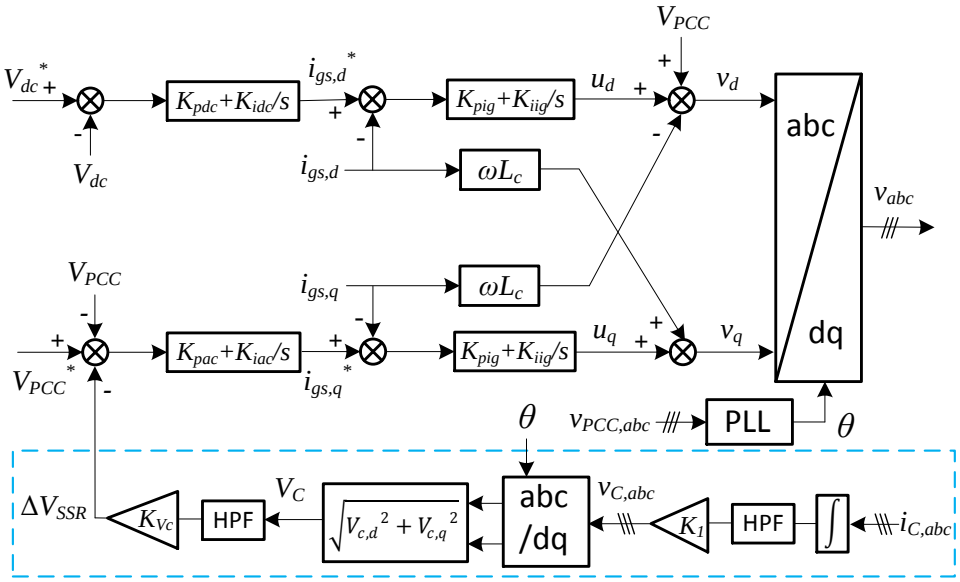

Figure 3.12: Topology of the improved SSR control.

3.6 Case Study

In this section, the EMT testbed will be used to replicate the real-world SSR events based on the found and estimated parameters. It will be found that the replication results match the real-world records very well. Then, the improved SSR control will be implemented in this EMT testbed to mitigate SSR. Event 1 and Event 3 are used to test its performance under different conditions.

3.6.1 Replication Results

Fig. 3.14 shows the replication results including instantaneous currents from WF 2 and its FFT spectrum. During the replications, the same sequence of tripping operations in real-world events was used. The first tripping operation was the transmission line and happened at 1 sec for all three events. The second tripping was the wind farm at 2 seconds. In Event 1 and Event 2, WF2 and WF1 were tripped respectively while there was no wind farm tripped in Event 3 according to [36].

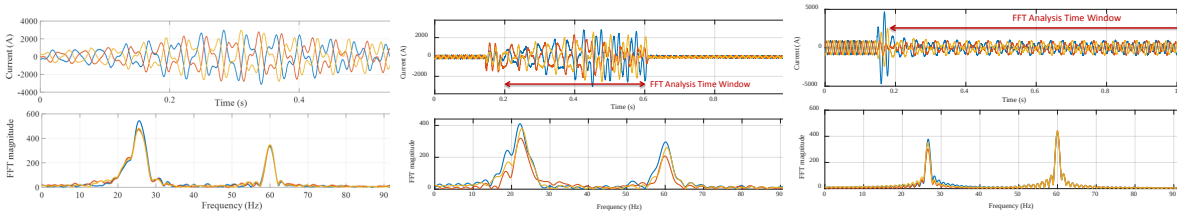

(a) (b) (c)

Figure 3.13: Real-world data. Event 1 (3.13a): 25.6 Hz. Event 2 (3.13b): 22.5 Hz. Event 3 (3.13c): 26.5 Hz.

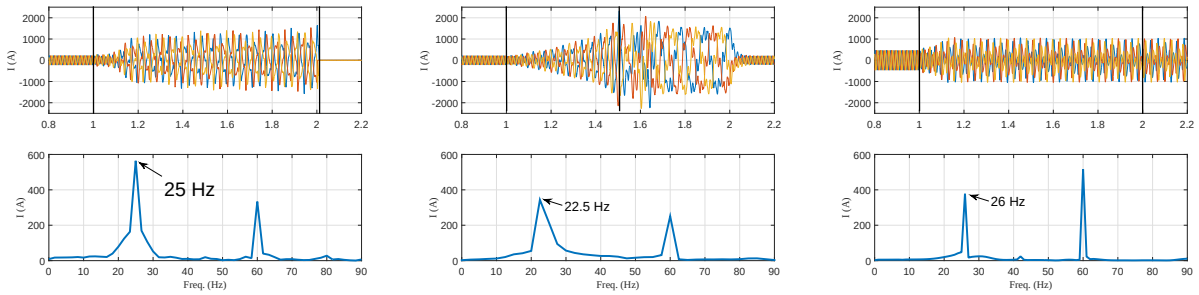

(a) (b) (c)

Figure 3.14: Simulation results based on the testbed. Event 1 (3.14a); Event 2 (3.14b); Event 3 (3.14c).

Compared with the recorded data, the replication results had very similar frequencies and magnitudes of the SSR and fundamental components. In addition, the replication results for Event 1 and Event 3 explained that the different wind speeds caused different consequences in these two events.

3.6.2 SSR Mitigation

In Event 1 and Event 3, WF2 suffered SSR because it was radially connected to the RLC circuit after the line tripping so the SSR mitigation control was implemented in GSC of WF2. Different than replication, there was only one tripping operation, line tripped at 1 sec.

3.6.2.1 Event 1

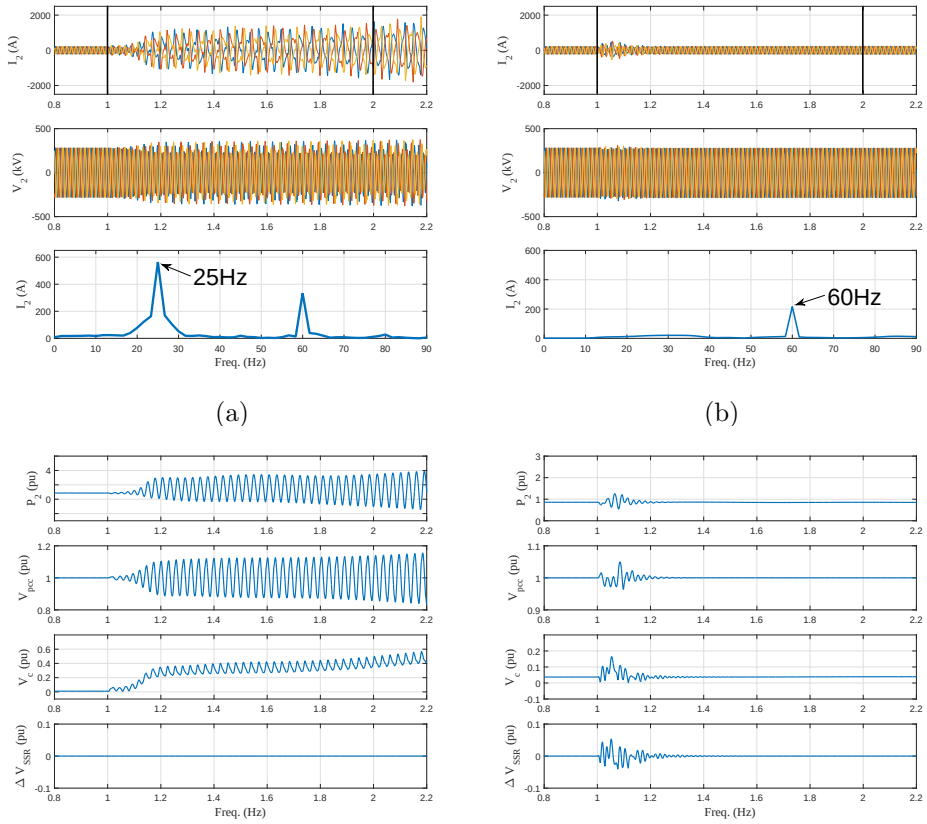

Figure 3.15: SSR control was implemented in Event 1. Without SSR control: (3.15a) and (3.15c); with SSR control: (3.15b) and (3.15d).

Fig. 3.15 shows dynamic responses in Event 1 with and without the SSR control. The left two plots show the simulation results of the system without the SSR control while the right column presents the results of the system with the SSR control. The upper two plots are in real values and show the three-phase currents at 345 kV side of T_2, the three-phase voltages at 345 kV level, and

FFT analysis of the current on phase a. The lower two plots are in per-unit values and show the power from WF2, the magnitude of PCC voltage, the magnitdue of the series capacitor voltage, and the SSR modulation signal ΔV_{SSR}.

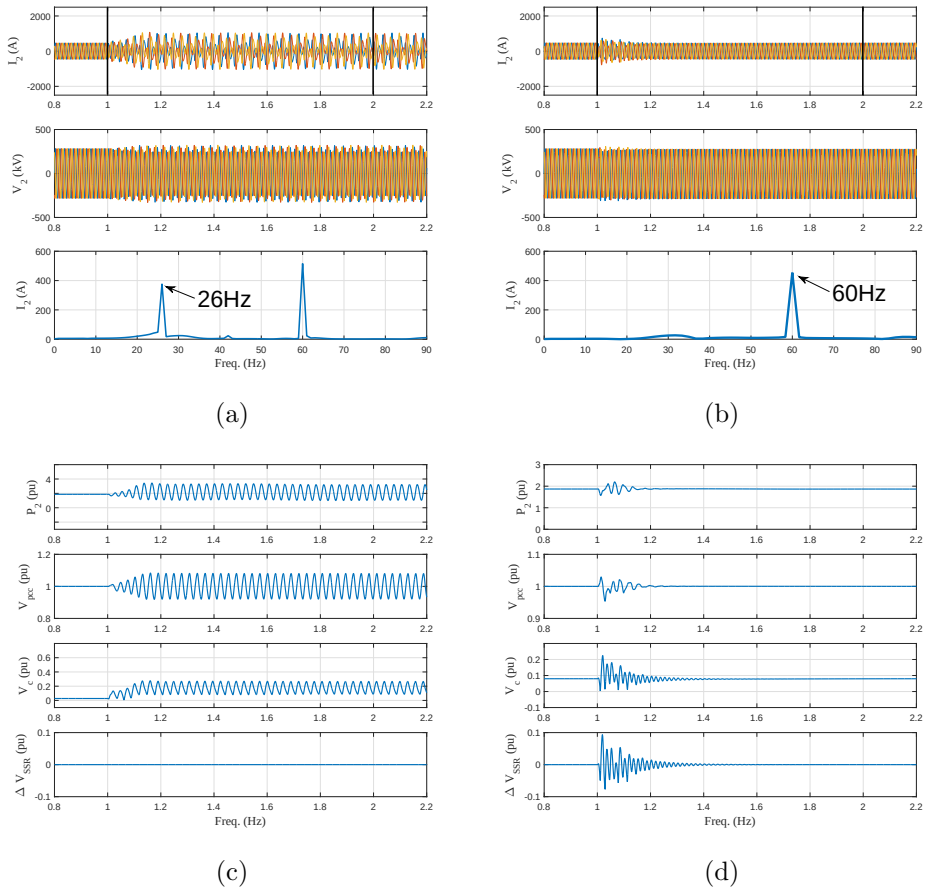

Figure 3.16: SSR control was implemented in Event 3. Without SSR control: (3.16a) and (3.16c); with SSR control: (3.16b) and (3.16d).

Based on Fig. 3.15a and Fig. 3.15c, the SSR appeared in the system without the SSR control (by setting $K_{VC} = 0$) after the line tripped at 1 sec. According to the FFT analysis, the frequency of the SSR component was 25 Hz and its magnitude was much larger than the fundamental component at 60 Hz.

After the SSR control activated by setting $K_{Vc} = 0.8$, the system returned to be stable quickly after the line tripping. In Fig. 3.15b and Fig. 3.15d, it was obviously observed that the SSR was

damped well and the transient after the line tripping was a period of about 0.3 sec. In the FFT spectrum, the SSR component could be ignored compared with the 60 Hz component. Therefore, SSR control can mitigate the SSR in Event 1 significantly.

3.6.2.2 Event 3

Event 1 and Event 3 had the same line tripping but had different operating conditions such as the wind speed and the number of online wind turbines. Hence, the SSR control was implemented in Event 3 to test its performance under different conditions. Because of the faster wind speed, Event 3 had a higher wind power from WF2 (around 2 pu).

Fig. 3.16 shows dynamic responses in Event 3 with and without the SSR control. Due to the higher power, SSR control used a longer time to make the system stable but the SSR was still mitigated completely after 0.5 sec after the line tripped.

We also tested the SSR control in Event 1 with 300 online wind turbines in WF2. The testbed simulation results again show SSR control can effectively mitigate SSR. These case studies used the simulation results to validate the performance of SSR control in Type-3 wind connected to the series compensated networks.

3.7 Conclusion

In this chapter, three real-world Type-3 wind SSR events were replicated successfully using the EMT testbed which is built in Matlab/SimPowerSystems. The testbed structure can be completed easily but the challenge for the replication is to find the accurate parameters with very limited information. Hence, the contributions of this research topic are not only to investigate the SSR stability of Type-3 wind in series compensated networks but also to share a feasible procedure on how to build a complex EMT testbed with the limited information. Besides the replication results, this chapter also provides an approach to mitigate SSR instability. The SSR control is implemented in GSC and is improved from a previously proposed method.

Chapter 4: Multi-inverter Modeling of RES and BESS in Microgrid

4.1 Introduction

Due to the specific characteristics of microgrids, the stability issues in microgrids are different than the conventional grid but the same approaches in the above chapters can be used to analyze the stability of the microgrid. The analytical model is derived to generate the eigenvalue analysis while the testbeds are built for the validation.

In 2015, an advanced droop control was proposed to coordinate DERs [53]. In 2016, I implemented this relatively new control strategy in a medium-voltage level microgrid testbed which is built in MATLAB/SimPowerSystems. During the simulation, an obvious oscillation occurred in the system under the islanded mode when I selected the smaller droop coefficients. To analyze this stability issue, a multi-inputs-multi-outputs (MIMO) model was derived to produce the eigenvalue analysis. In the eigenvalue loci, the oscillation mode can be found when the droop coefficients become smaller. This finding verified the instability phenomena in the detailed testbed. Furthermore, the grid-connected mode is analyzed as well. This chapter will present the principles of V-I droop and how the MIMO model is derived in Section 4.2 [3]. Then, the eigenvalue analysis and simulation results will be presented to match each other.

As another type of DER in the microgrid, the battery energy storage system (BESS) contains the similar dynamics of RES and the dynamics of battery. Different than RES, the power of BESS is not dependent on the nature factors so its power can be controlled more widely for other objectives. As aforementioned in Chapter 1, the consensus on the power and energy of multiple BESS is an effective method for microgrids and devices. After the stability analysis for V-I droop, another section will introduce the principles of consensus control. Then, a three-inverters analytical model

[3] Section 4.2 was published in IEEE Transactions Power Delivery [84], 2017. Permission is included in Appendix A.

is derived and used to test consensus control. Finally, a controller-hardware-in-the-loop (CHIL) testbed is presented with detailed information and experimental results.

4.2 Stability Analysis in Microgrid with V-I Droop

4.2.1 Microgrid with V-I Droop

As mentioned in [53], the system frequency in the microgrid with V-I droop should be kept as a constant using the global positioning system (GPS) signals. In other words, all the measurements should be synchronized by a fixed frequency, ω_0. In this section, the system frequency is fixed at 60 Hz and the reference frame is $d+jq$. In addition, V_{PCC} is assumed to be aligned at the d-axis ($V_{PCCd} = V_{PCC}, V_{PCCq} = 0$) for the initial condition.

4.2.1.1 Topology of Circuit

The system with V-I droop is a microgrid with two parallel DERs and two fixed loads. The system topology is shown in Fig. 4.1. Each DER has a vector-control based VSC and an RLC filter. There is a small purely inductive transmission line (L_L) installed between each DER and the point of common coupling (PCC). It is added because of the principles of V-I droop and its value is very small compared with the inductance in the RLC filter. Two DERs share the same parameters except for the droop coefficients.

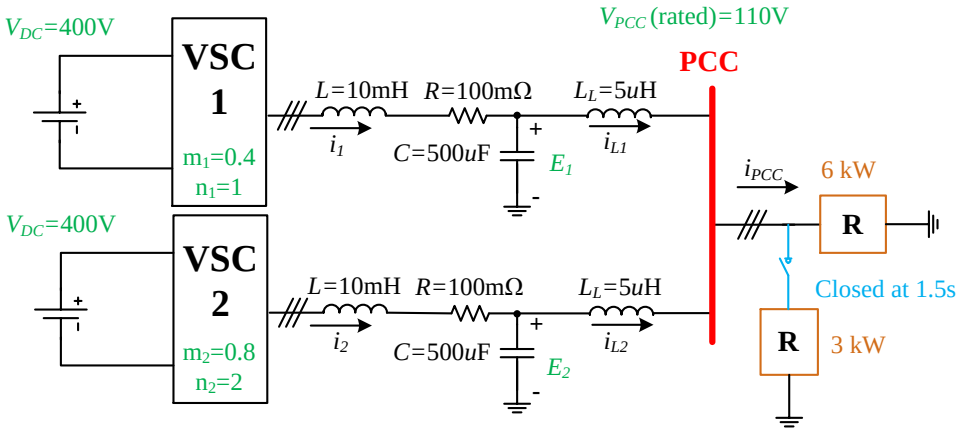

Figure 4.1: Two DERs support one load through parallel VSCs.

4.2.1.2 Principles of V-I Droop

In the microgrid, the complex power generated by kth DER at the PCC bus is expressed by S_k. This power can be delivered to the load or the grid corresponding to the connection mode of the microgrid. In this section, $k = 1, 2$. It is assumed that the d-axis is aligned with the PCC voltage space vector. In other words, $v_d = |\overrightarrow{v}_{PCC}|$. Then, the complex power based on the voltage and current in the dq frame can be simplified by the following.

$$S_k = \frac{3}{2} v_d (i_{Ldk} - j i_{Lqk}) = \frac{3}{2} (v_d i_{Ldk} - j v_d i_{Lqk}) \tag{4.1}$$

Then, we can separate S into real and reactive power:

$$P_k = \frac{3}{2} v_d i_{Ldk} \tag{4.2a}$$

$$Q_k = -\frac{3}{2} v_d i_{Lqk} \tag{4.2b}$$

Based on (4.2b), the real power sharing is dependent on the current sharing on d-axis while the reactive power sharing can be determined by the current sharing on q-axis. It is assumed that each DER is connected to the PCC bus through a line whose impedance is $R_k + jX_k$. The following equation expresses the relationship among the converter voltage, PCC voltage and the output current at steady-state.

$$\begin{bmatrix} R_k & -X_k \\ X_k & R_k \end{bmatrix} \begin{bmatrix} i_{Ldk} \\ i_{Lqk} \end{bmatrix} = \begin{bmatrix} E_{kd} \\ E_{kq} \end{bmatrix} - \begin{bmatrix} v_d \\ 0 \end{bmatrix} \tag{4.3}$$

After V-I droop is implemented in the microgrid, an additional term related to V-I droop will be added in (4.3). The new expression is (4.5). m_k is the droop coefficient for the current on d-axis while n_k is the droop coefficient for current on q-axis. It is assumed that R_k and X_k can be negligible compared with the droop coefficients. Hence, R_k and X_k can be removed from (4.5). Because $E_0 = v_d$, (4.5) can be simplified as (4.6).

$$\begin{bmatrix} E_{kd} \\ E_{kq} \end{bmatrix} - \begin{bmatrix} v_d \\ 0 \end{bmatrix} = \begin{bmatrix} E_0 \\ 0 \end{bmatrix} - \begin{bmatrix} m_k & 0 \\ 0 & n_k \end{bmatrix} \begin{bmatrix} i_{Ldk} \\ i_{Lqk} \end{bmatrix} - \begin{bmatrix} v_d \\ 0 \end{bmatrix} \tag{4.4}$$

$$\Rightarrow \begin{bmatrix} R_k + m_k & -X_k \\ X_k & R_k + n_k \end{bmatrix} \begin{bmatrix} i_{Ldk} \\ i_{Lqk} \end{bmatrix} = \begin{bmatrix} E_0 \\ 0 \end{bmatrix} - \begin{bmatrix} v_d \\ 0 \end{bmatrix} \tag{4.5}$$

$$m_1 i_{Ld1} = m_2 i_{Ld2} \tag{4.6a}$$

$$n_1 i_{Lq1} = n_2 i_{Lq2} \tag{4.6b}$$

Based on (4.6), the current sharing on the $d-$axis between two DERs can be determined by the ratio of $1/m_k$ while the current sharing on $q-$axis is equal to the ratio of $1/n_k$. In other words, the real power sharing is proportional to $1/m_k$ and the reactive power sharing is proportional to $1/n_k$. However, if R_k and X_k cannot be negligible compared with the droop coefficients m_k and n_k, the above proportional relations between power and droop coefficients cannot be obtained. It will cause accurate power sharing not achieved. On another hand, large droop coefficients may also lead converter voltages to drop below the range during heavy load conditions [53]. Hence, the selection of the droop coefficient is a tradeoff between the above two factors.

4.2.1.3 Control Strategy

V-I droop control is developed from the voltage/frequency (V/F) control which controls the PCC voltage on dq axis in the outer loop and the frequency is fixed. The gains of the controllers in V-I droop are designed based on the following equations.

As a kind of vector control, V-I droop has the inner current loop to control the output current in the dq axis. Fig. 4.2 shows the block diagram of the closed inner loop. Although it is simplified by ignoring the parts of decoupling and feedforward, it is usually used to design PI controllers in the inner current loop [85]. The block of $\frac{1}{Ls+R}$ represents the plant model of the filter. i_d and i_q

indicate the output currents on the dq axis while u_d and u_d are the intermediate variables expressed by (4.7).

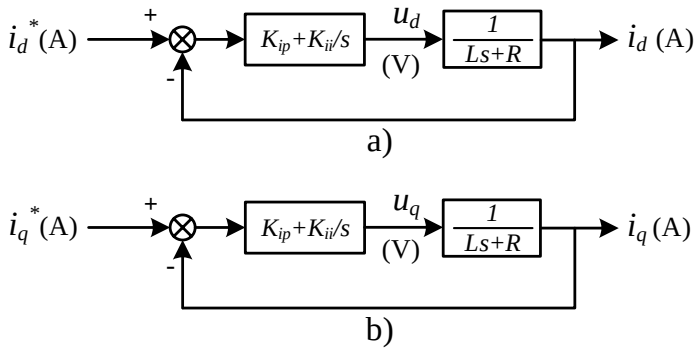

Figure 4.2: The block diagram for the inner loop transfer function.

$$\begin{cases} u_d = V_{td} - E_d - \omega L i_q \\ u_q = V_{tq} - E_q + \omega L i_d \end{cases} \tag{4.7}$$

where V_{td} V_{tq} are the converter output voltages and E_d E_q are the PCC voltages. The block of $K_{ip} + \frac{K_{ii}}{s}$ is PI controller whose proportional gain and integrator gain are designed based on (4.8) [85].

$$K_{ip} = \frac{L}{\tau_i}, K_{ii} = \frac{R}{\tau_i} \tag{4.8}$$

where τ_i is the inner loop time constant. After substituting (4.8) into the block diagram in Fig. 4.2, the inner loop can be expressed by the first-order closed-loop transfer function.

$$G_{ic} = \frac{i_d}{i_d^*} = \frac{G_{io}}{1 + G_{io}} = \frac{1}{\tau_i s + 1} \tag{4.9}$$

The outer loop controls the dq components of PCC voltage. Fig. 4.3 shows the block diagram including the outer loop, the simplified inner loop, and the plant model of a shunt capacitor. The gains of controllers in the outer loop can be designed based on the following two equations which are from [85, 86].

$$K_{vp} = C\omega_c = \frac{C}{\sqrt{\tau_i \tau_v}}, \quad K_{vi} = \frac{K_{vp}}{\tau_v} \tag{4.10}$$

where ω_c is the cut-off frequency and τ_v is the outer loop time constant. Because τ_i has been determined in the inner loop, the gains K_{vp} and K_{vi} can be calculated after the cut-off frequency is selected.

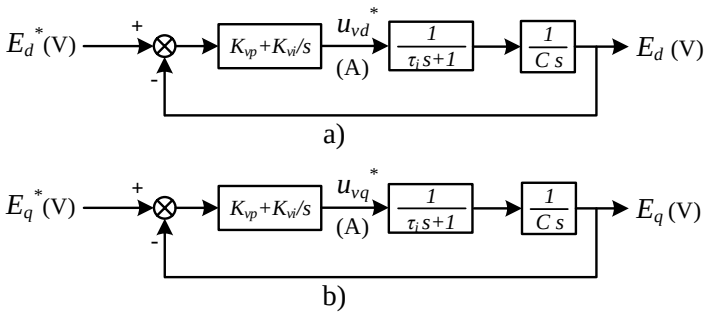

Figure 4.3: The block diagram for the outer loop transfer function.

The droop control strategy usually relies on the outer loop of vector control. In V-I droop, the function of power sharing is achieved by the droop relation between voltage and current. Therefore, the compensated voltages on the $d-$axis and $q-$axis from the droop control are calculated based on the current feedback. Fig. 4.4 shows the entire control scheme of V-I droop for one DER in the microgrid. The parts of decoupling and feedforward are considered. As noted, the V-I droop in this dissertation has two differences with the one in [53]. First, transformers are not used in our microgrid so that the terms of (X_T and R_T) in the droop formulation are also not considered. Second, [53] considers droop functions piecewise linear while this dissertation considers them linear.

4.2.2 Stability Analysis Using MIMO Model

4.2.2.1 MIMO Model Derivation

To conduct linear analysis, an analytical model needs to be derived and linearized with the flat run. Different than the analytical model mentioned in the above chapters, the analytical model for V-I droop does not include the dynamics of PLL. In addition, it is designed in physical values and uses a multiple-input-multiple-output (MIMO) matrix to model the transmission network. Fig. 4.5 shows the block diagram of the entire MIMO model including three dynamic blocks. G_1

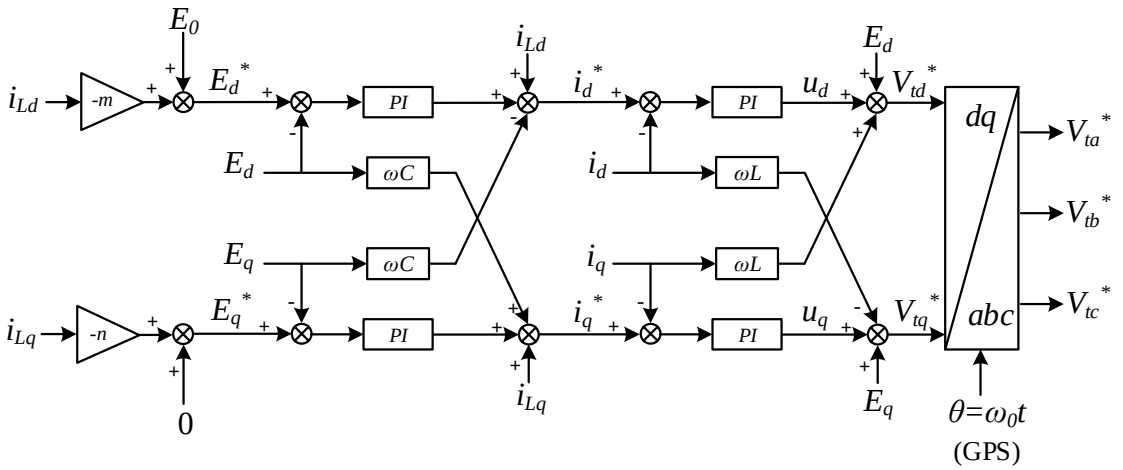

Figure 4.4: Control block diagram for V-I droop.

presents the dynamics of VSCs with the control loop, G_2 is the matrix to show the dynamics of the transmission network, and G_3 illustrates the power sharing or the droop control loop.

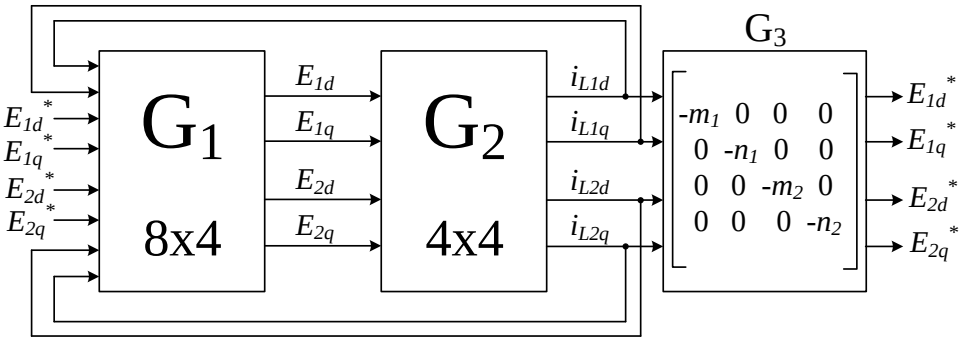

Figure 4.5: The block diagram of the MIMO model of the system with two VSCs and V-I droop.

Fig. 4.6 shows the block diagram for the single DER with the control strategy. Compared with Fig. 4.4, the block diagram in Fig. 4.6 does not only include the V/f control strategies but also the plant models of the RLC filter. G_1 contains two of these block diagrams for two DERs respectively.

According to Fig. 4.6, each DER requires four inputs (voltage references (E_d^* and E_q^*) and load current measurements (i_{Ld}, i_{Lq})) and two outputs (the capacitor voltages E_d and E_q). Hence, G_1 has eight inputs and four outputs because of two DERs in microgrid.

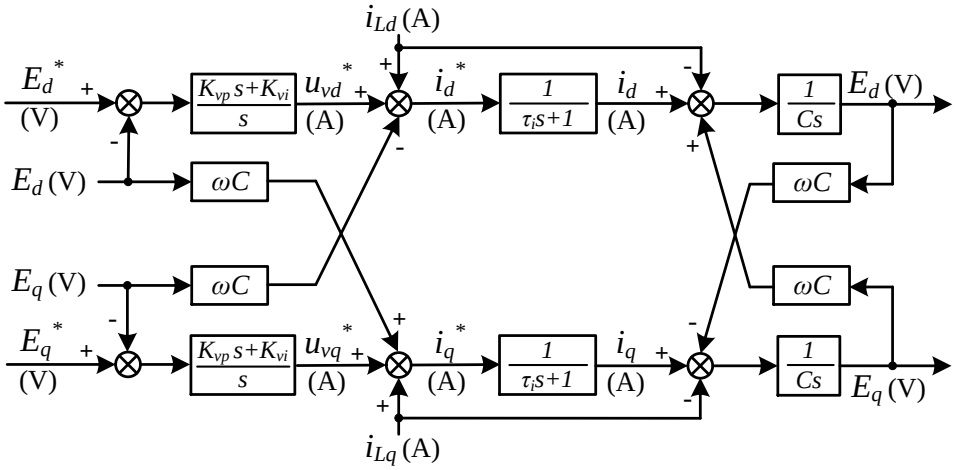

Figure 4.6: The block diagram of a VSC with an RLC filter.

G_2 represents the dynamics of the transmission network using a MIMO matrix which is derived based on the islanded network shown in Fig. 4.7. Due to V/f control, two DERs can be considered as two voltage sources and support a purely resistive load. Using superposition, the currents i_{L1}, i_{L2} can be expressed by the converter voltages E_1, E_2 and impedance of network.

$$\begin{cases} i_{L1} = & E_1 \frac{1}{R_{lo}\|L_L s+L_L s} - E_2 \left(\frac{1}{R_{lo}\|L_L s+L_L s} \frac{R_{lo}}{R_{lo}+L_L s} \right) \\ i_{L2} = & E_2 \frac{1}{R_{lo}\|L_L s+L_L s} - E_1 \left(\frac{1}{R_{lo}\|L_L s+L_L s} \frac{R_{lo}}{R_{lo}+L_L s} \right) \end{cases} \tag{4.11}$$

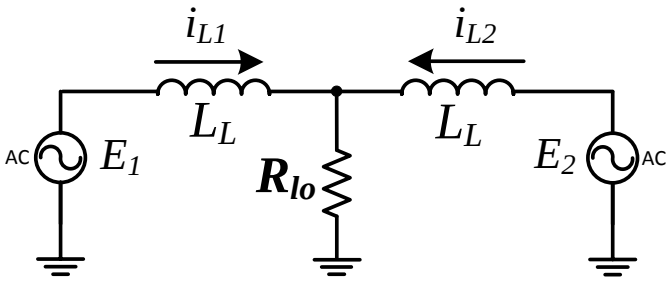

Figure 4.7: The system without the VSC dynamics.

(4.11) is in *abc* frame but the control loop is modeled in *dq* frame. Hence, (4.11) needs to be converted to *dq* frame by replacing s using $s + j\omega$. $\omega = 377$ rad/s if the dominant frequency is 60 Hz. This is due to the fact that a space vector in the *abc*-frame is related to a vector in the

dq-frame as follows.

$$\overrightarrow{f}_{abc} = \overline{f}_{dq} e^{j\omega t}. \tag{4.12}$$

After replacing s using $s + j\omega$ in (4.11), the transfer function will be divided into two terms, real term and imaginary term. (4.13) illustrates that four inputs of G_2 are PCC voltages of two DERs and four outputs are currents from DERs which are also sent back to G_2.

$$\begin{bmatrix} i_{L1d} \\ i_{L1q} \\ i_{L2d} \\ i_{L2q} \end{bmatrix} = \underbrace{\begin{bmatrix} G_{21r} & -G_{21i} & G_{22r} & -G_{22i} \\ G_{21i} & G_{21r} & G_{22i} & G_{22r} \\ G_{22r} & -G_{22i} & G_{21r} & -G_{21i} \\ G_{22i} & G_{22r} & G_{21i} & G_{21r} \end{bmatrix}}_{G_2} \begin{bmatrix} E_{1d} \\ E_{1q} \\ E_{2d} \\ E_{2q} \end{bmatrix} \tag{4.13}$$

where G_{21r}, G_{21i}, $G_{22r}$and G_{22i} are the transfer functions and expressed in (4.14).

$$\begin{aligned}
G_{21r} &= \frac{L_L^3 s^3 + 3L^2 R_{lo} s^2 + (L_L^3 + \omega^2 + 2L_L R_{lo}^2)s + L_L^2 R_{lo}\omega^2}{G_{21D}} \\
G_{21i} &= \frac{L_L^3 \omega s^2 + 2L_L^2 R_{lo}\omega s + (L_L^3\omega^3 + 2L_L R_{lo}^2\omega)}{G_{21D}} \\
G_{22r} &= \frac{L_L^4 R_{lo} s^4 + 4L^3 R_{lo}^2 s^3 + 5L_L^2 R_{lo}^3 s^2 + 2LR_{lo}^4 s - (L_L^2 R_{lo}^3\omega^2 + L_L^4 R_{lo}\omega^4)}{G_{22D}} \\
G_{22i} &= \frac{L_L^4 R_{lo} s^4 + 4L_L^3 R_{lo}^2 s^3 + 5L_L^2 R_{lo}^3 s^2 + 2LR_{lo}^4 s - (L_L^2 R_{lo}^3\omega^2 + L_L^4 R_{lo}\omega^4)}{G_{22D}}
\end{aligned}$$

where

$$\begin{aligned}
G_{21D} &= L_L^4 s^4 + 4L^3 R_{lo} s^3 + (2L^4\omega^2 + 4L_L^2 R_{lo}^2)s^2 + 4L_L^3 R_{lo}\omega^2 s + (L_L^4\omega^4 + 4L_L^2 R_{lo}^2\omega^2) \\
G_{22D} &= L_L^6 s^6 + 6L_L^5 R_{lo} s^5 + (3L_L^6\omega^2 + 13L_L^4 R_{lo}^2)s^4 + (12L_L^5 R_{lo}\omega^2 + 12L_L^3 R_{lo}^3)s^3 \\
&\quad + (3L_L^6\omega^4 + 18L_L^4 R_{lo}^2\omega^2 + 4L_L^2 R_{lo}^4)s^2 + (6L_L^5 R_{lo}\omega^4 + 12L_L^3 R_{lo}^3\omega^2)s \\
&\quad + (L_L^6\omega^6 + 5L_L^4 R_{lo}^2\omega^4 + 4L_L^2 R_{lo}^4\omega^2)
\end{aligned} \tag{4.14}$$

Based on the four output currents from G_2, four references of the PCC voltages can be calculated using the droop control loop shown in Fig. 4.4. The no-load voltage or rated PCC voltage E_0 is the same for two DERs while the droop coefficients are different for unequal power sharing.

4.2.2.2 *Linear Analysis for Autonomous Mode*

To generate the poles and zeros, *Control Design Toolbox* in MATLAB is used to linearize the MIMO model shown in Fig. 4.5. The parameters used in the MIMO model are listed in Table 4.1 and Table 4.2. After merging the poles and zeros for different droop coefficients in one plot, the movement of dominant poles can be obtained. Based on the movements of the dominant poles, the effects of droop coefficients on the system stability can be found. Fig. 4.8 shows the movement of poles and zeros with the changes of m_1 and m_2. Because the ratio of power sharing is $2:1$, m_1 is increased from 0.004 to 0.4 while m_2 is increased from 0.008 to 0.8. n_1 and n_2 are kept as the constants 1 and 2 respectively.

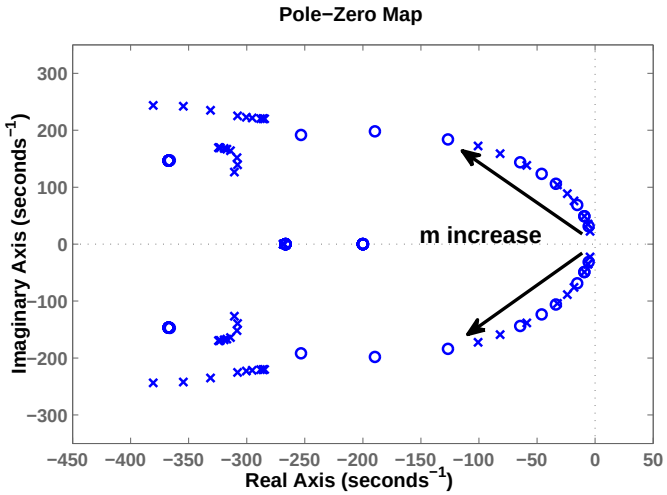

Figure 4.8: The values of m_1 and m_2 affect the continuous movement of dominant eigenvalues.

Fig. 4.8 shows the map of poles and zeros with the changes of n_1 and n_2. In this case, $m_1 = 0.4$ and $m_2 = 0.8$ while n_1 is increased from 0.01 to 1 and n_2 is increased from 0.02 to 2.

According to both eigenvalue loci, the dominant poles become more closed to the imaginary-axis with decreasing either m_k or n_k. It means that the smaller droop coefficients will lead to slower dynamics and smaller damping ratio but they are still in the left half-plane (LHP). In other words, the microgrid with V-I droop will suffer the oscillation issue with either small m_k or n_k but it is still stable.

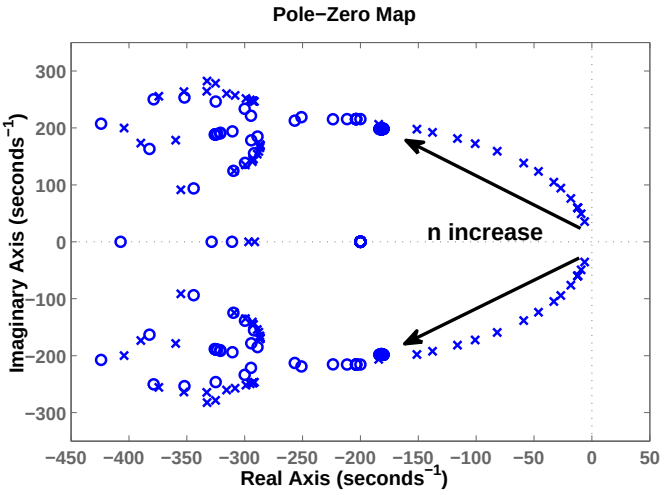

Figure 4.9: Increasing n_1 and n_2 leads to the dominant poles moving to the left half plane (LHP).

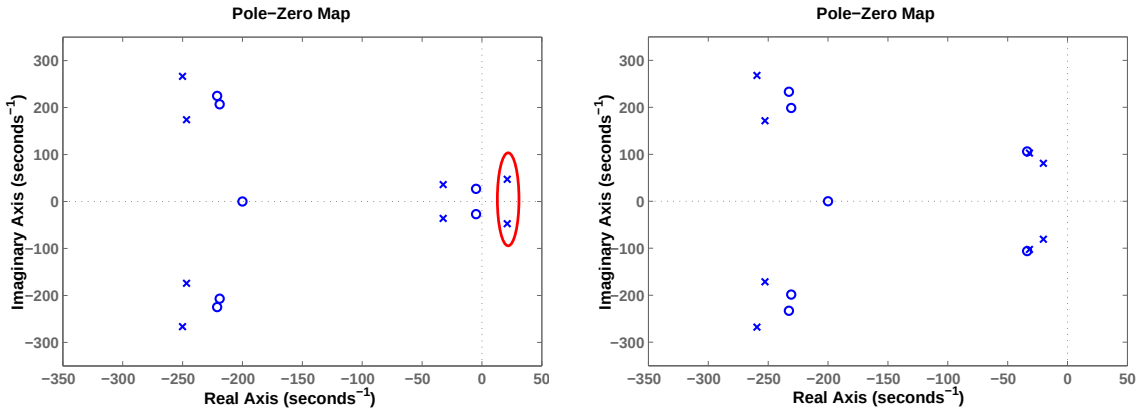

(a) (b)

Figure 4.10: Eigenvalue loci with different droop coefficients. (a) shows poles and zeros when $m_1 = 0.004$, $m_2 = 0.008$, $n_1 = 0.01$, and $n_2 = 0.02$; (b) shows poles and zeros when $m_1 = m_2 = 0.004$, $n_1 = n_2 = 0.01$.

If the small values are selected for both m_k and n_k, the system will be unstable. Fig. 4.10a shows the poles and zeros for this specific case with $m_1 = 0.004$, $m_2 = 0.008$, $n_1 = 0.01$, and $n_2 = 0.02$. In Fig. 4.10a, a pair of dominant poles are located in RHP. However, there is an exception. If $m_1 = m_2 = 0.04$ and $n_1 = n_2 = 0.04$, the system will stable and will not have the oscillation issue. The corresponding poles and zeros are shown in Fig. 4.10b.

4.2.2.3 Linear Analysis for Grid-connected Mode

The MIMO model is modified based on the system shown in Fig. 4.11 to check whether the small droop coefficients may cause stability issues in the grid-connected microgrid. Compared with Fig. 4.7, another voltage source is integrated at the middle point through an inductive line L_G.

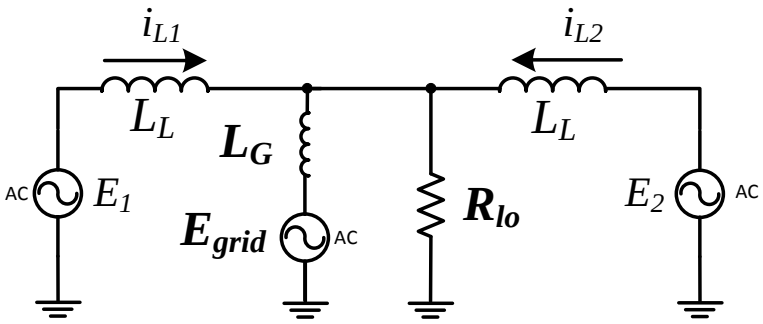

Figure 4.11: The grid-connected system without the VSC dynamics.

The new G_2 in the MIMO model is derived to include the dynamics of load and grid while G_1 and droop parts are not changed. This case will investigate the effect of grid strength on the stability issue caused by the small droop coefficients. Therefore, the smaller values (0.01 and 0.02) are selected for n_1 and n_2 while the inductance of the transmission line L_G is changed. Fig. 4.12 shows the movement of the dominant poles with the short-circuit ratio (SCR) increased from 0.5 to 5. SCR is the factor to determine the strength of the grid. Based on Fig. 4.12, the damping ratio of the dominant poles becomes larger when the grid becomes stronger.

In conclusion, the droop coefficient with a small value may lead the oscillation issues in the microgrid with V-I droop. When both droop coefficients are small, the system will lose stability. When both droop coefficients are equal, the system will be stable even if they are very small. In addition, this stability issue will not happen in the microgrid connected to the strong grid.

4.2.3 Case Study

As aforementioned in the introduction of this chapter, the stability issue in the microgrid with V-I droop was found after I implemented V-I droop in the detailed simulation testbed. The simulation

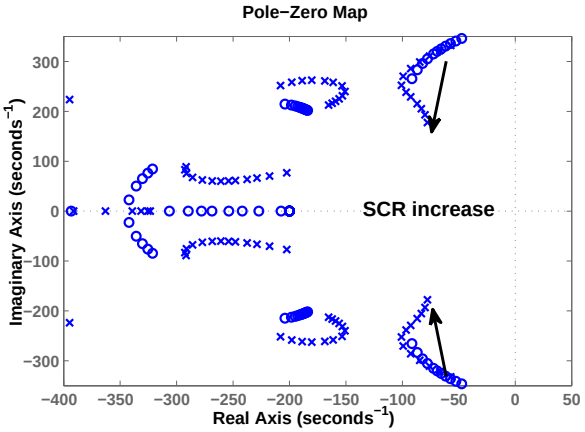

Figure 4.12: When a grid is connected, the value of SCR affects the continuous movement of dominant eigenvalues.

Table 4.1: Circuit parameters

Parameter	Values
DC voltage	400 V
No-load voltage, E_0	102 V
Rated voltage on load	110 V (rms, L-L)
Nominal frequency, ω_0	377 rad/s
Switching frequency	3060 Hz
R of RLC filter	100 mΩ
$L$of RLC filter	10 mH
$C$of RLC filter	0.5 mF
L_L of transmission line	5 μH

results in this section will not only verify the capability of V-I droop control's power sharing but also verify the stability analysis in the above subsections.

This testbed includes the dynamics of power electronic switching. Its topology in autonomous mode is shown in Fig. 4.1. The control scheme for each DER is the same as Fig. 4.4. The parameters are listed in Table 4.1 while the gains of the PI controllers are listed in Table 4.2. As mentioned, the reactance of L_L is 0.0019Ω so the droop coefficients should be selected much larger than 0.0019 to achieve the accurate power sharing. A purely resistive load was considered in the case studies.

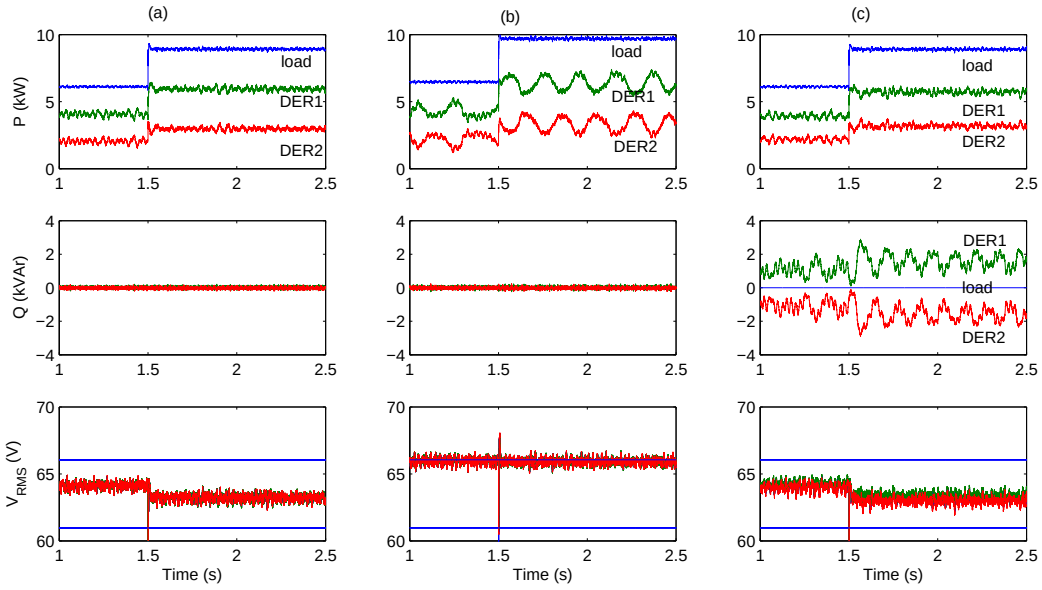

Figure 4.13: Simulation results: Case (a) $m_1 = 0.09, m_2 = 0.18, n_1 = 1, n_2 = 2$; Case (b) $m_1 = 0.004, m_2 = 0.008, n_1 = 1, n_2 = 2$; Case (c) $m_1 = 0.09, m_2 = 0.18, n_1 = 0.01, n_2 = 0.02$. The two straight lines in voltage plots indicate $\pm 4\%$ range.

4.2.3.1 Effect of Droop Coefficients

Fig. 4.13 shows the dynamic responses for different sets of droop coefficients which are mentioned in the caption. The dynamic responses include real power and reactive power for DER 1, DER 2, and load. The PCC voltage was plotted as well.

In Case (a), the relatively large values were selected for m_k and n_k so there was no oscillation issue that happened in the dynamic responses. In Case (b), m_1 and m_2 were reduced to 0.004 and 0.008 while n_1 and n_2 were not changed. The obvious oscillations around 5 Hz were observed in the real power from DERs as shown in (b). In Case (c), m_1 and m_2 returned to be the initial values while n_1 and n_2 were reduced to 0.01 and 0.02. Then, oscillations around 7 Hz happened in the reactive power. In all three cases, the PCC voltage was always within the range of $\pm 4\%$.

4.2.3.2 Effect of Network Resistance

The factor causing oscillations in reactive power is considered as the circulating currents which are basically q-axis currents going back and forth between the DER units. They increased the

stress on and losses in transmission lines. To verify this point, the sensitivity analysis of the network parameters was conducted. An RL line was used to replace the purely inductive line L_L. The resistance of RL line r was selected as 0.1Ω and 0.01Ω while its inductance X_L was not changed. Fig. 4.14 shows the dynamics of reactive power for three different transmission lines. In plot (a), the transmission line was RL circuit with $r = 0.1\Omega$ and there was no oscillation in reactive power. In plot (b), $r = 0.01\Omega$ and the oscillation could be observed but its magnitude was smaller than the plot (c). The dynamic responses in the plot (c) were the same as Case (c) in Fig. 4.13 because the transmission line was purely inductive. Based on Fig. 4.14, it was found that the network resistance or R/X ratio of the line has a significant effect on the oscillation issue.

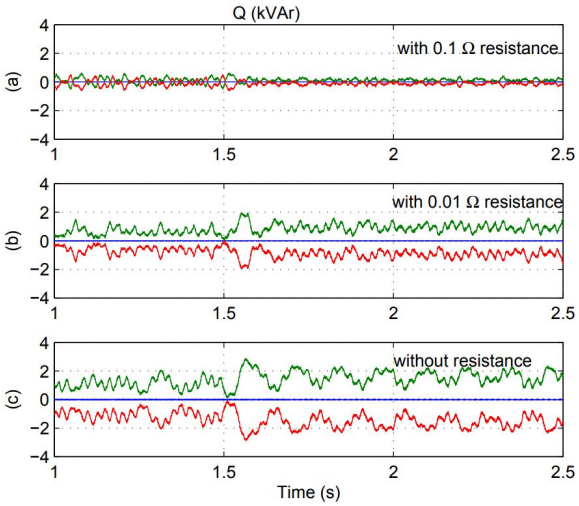

Figure 4.14: Effect of the network resistance. (a) with 0.1Ω resistance; (b) with 0.01Ω resistance; (c) without resistance.

4.2.3.3 Sensitivity of SCR

According to stability analysis, a strong grid can make the microgrid with V-I avoid the stability issue which are caused by the small droop coefficients. In this case, two strength levels were selected for the grid, $SCR = 1$ and $SCR = 5$. The dynamic event was still the load change at 1.5 sec and the droop coefficients were the same as Case (c). Fig. 4.15 shows the corresponding dynamics. When the microgrid was connected to the weak grid ($SCR = 1$), the obvious oscillations could be

found in reactive power. However, the magnitude of oscillation was reduced when the microgrid was connected to a strong grid ($SCR = 5$).

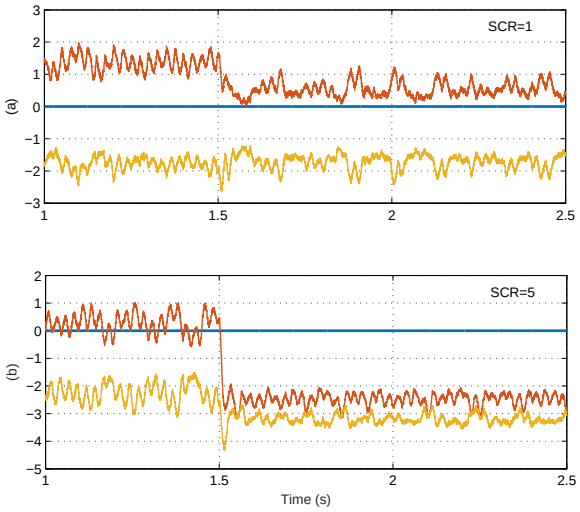

Figure 4.15: Effects of SCR. Upper plot shows effect of $SCR = 1$ on reactive power; the lower plot shows Effect of $SCR = 5$ on reactive power. In both cases, $m_1 = 0.4$, $m_2 = 0.8$, $n_1 = 0.01$ and $n_2 = 0.02$.

4.3 Consensus Control for Microgrid with BESS

4.3.1 Consensus Control Design

Before designing the consensus control, we should know the communication graph of the microgrid with multiple BESS. As the advantage, consensus control only requires each BESS to communicate with its neighbors. Fig. 4.16 shows the communication graph of the system used in this paper and it is normally expressed by Laplacian matrix L. D matrix represents the degree of each node while A matrix represents the communication link between every two nodes.

$$L = \begin{bmatrix} 1 & -1 & 0 \\ -1 & 2 & -1 \\ 0 & -1 & 1 \end{bmatrix} = \underbrace{\begin{bmatrix} 1 & 0 & 0 \\ 0 & 2 & 0 \\ 0 & 0 & 1 \end{bmatrix}}_{D} - \underbrace{\begin{bmatrix} 0 & 1 & 0 \\ 1 & 0 & 1 \\ 0 & 1 & 0 \end{bmatrix}}_{A} \tag{4.15}$$

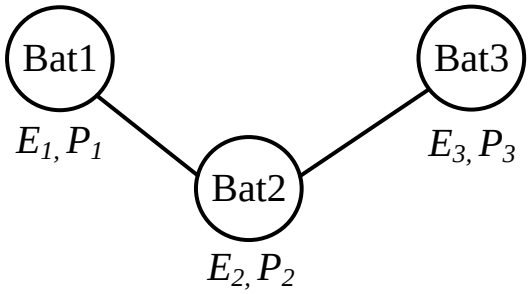

Figure 4.16: Communication graph of a system with three BESS.

Due to the relation between energy and power, the dynamics of each battery energy storage system can be written by (4.16). The energy and power are the states while the input is the power differential. Meanwhile, the energy can be represented by the state of charge (SoC).

$$\underbrace{\begin{bmatrix} \dot{E}_1 \\ \dot{P}_1 \end{bmatrix}}_{\dot{y}_i} = \underbrace{\begin{bmatrix} 0 & -1/3600 \\ 0 & 0 \end{bmatrix}}_{A_i} \underbrace{\begin{bmatrix} E_1 \\ P_1 \end{bmatrix}}_{y_i} + \underbrace{\begin{bmatrix} 0 \\ 1 \end{bmatrix}}_{B_i} u_i \tag{4.16}$$

where u_i is the control input (or control reference) for the energy storage system. x_i is the output matrix for the state space of each energy storage system.

For the multiple energy storage systems, the matrix can be expressed as:

$$\dot{\mathbf{Y}} = (I_N \otimes \mathbf{A})\mathbf{Y} + (I_N \otimes \mathbf{B})\mathbf{U} \tag{4.17}$$

where N is the number of energy storage systems in the system. In this section, $N = 3$.

To achieve the consensus on energy and power of N BESS, the control input is designed as the following equation [87]. c is a positive scalar coupling gain. K is the feedback control matrix. a_{ij} is the element of A matrix. With this design, the sum of inputs is always zero. In other words, the sum of real power of all BESS should be a constant.

$$u_i = cK \sum_{j=1}^{N} a_{ij}(x_j - x_i) \tag{4.18}$$

Linear quadratic regulator (LQR) with the infinite-horizon is used to find the feedback gain matrix K which minimizes the sum of the inputs.

$$K = R^{-1}B^{T}P_{uni} \tag{4.19}$$

$$u = -cKx \tag{4.20}$$

where P_{uni} is the unique positive definite solution of the control algebraic Riccati equation (ARE). The following equation is the continue-time ARE.

$$A^{T}P_{1} + P_{1}A + Q - P_{1}BR^{-1}B^{T}P_{1} = 0 \tag{4.21}$$

where Q and R are two weight matrices. After Q and R are given, this equation can be solved by MATLAB code *care*; then, K can be calculated. In other words, the design of R and Q will affect the performance of consensus control. According to [62], a larger Q results in faster dynamic response in x_i while a larger R penalizes the input and results in less effort in control or small values in u_i.

The scalar coupling gain c should be design to make the system stable. The following equation shows the maximum value which can be selected for c.

$$c \leq \max\left(\frac{1}{2\min Re(\lambda_i)}, 1\right) i = 2, ..., n \tag{4.22}$$

where λ_i is the eigenvalue of L matrix.

4.3.2 Analytical Model

The consensus control among the BESS normally requires a long time to converge the power and energy. The host PC cannot handle this long-time simulation task for a detailed model built in MATLAB/SimPowerSystems. Hence, the analytical model (mathematical equation-based) is a better way to save time on simulating tests and analysis. It is built in MATLAB/Simulink and

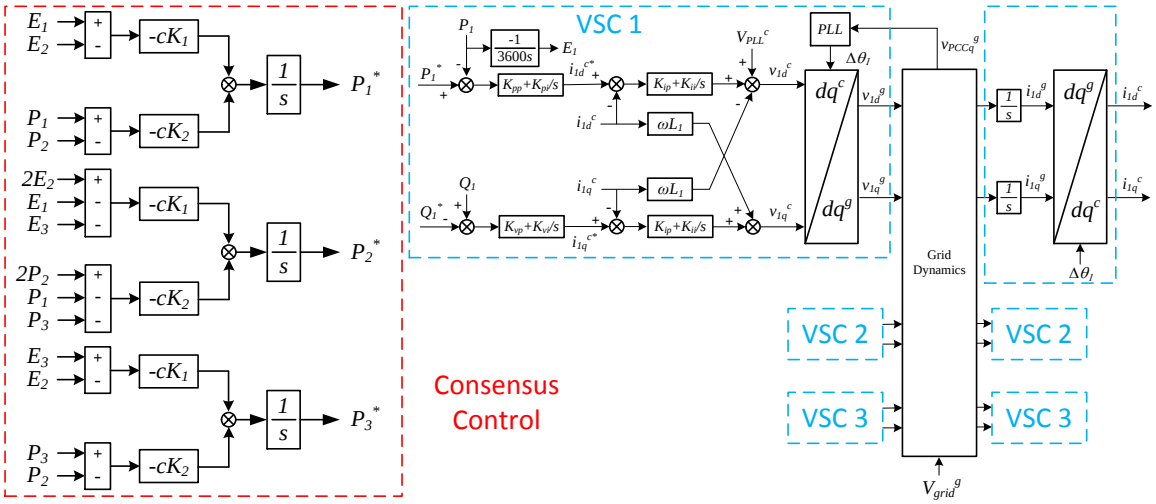

Figure 4.17: The topology of the analytical model in Simulink.

includes the essential dynamics including the vector control loop, consensus control, PLL dynamics, grid dynamics, and battery dynamics on power and energy. It can not only be used to test consensus control but also used to analyze the stability issue in the grid-connected microgrids.

Table 4.3: Parameters of the microgrid

Names	values
S_b	100 MVA
V_b at grid	230 kV
V_b in microgrid	18 kV
X, R, B	0.1, 0.02, 0.05
X_T	0.069
K_{pc}, K_{ic}	0.3, 5
K_{pv}, K_{iv}	0.25, 25
K_{ipll}, K_{ipll}	60, 1400

Table 4.4: Parameters of consensus control

Names	Values
Q	diag([50,1])
R	200
K_1	-0.5
K_2	0.073
c	0.1

In this section, the microgrid includes three vector-control based inverters integrated at the same PCC bus. The dc side of each inverter is connected to a Lithium-ion battery. The real and reactive power of BESS are controlled by vector control. The consensus control is implemented upon the outer loop to generate the references of real power P_i^*. The parameters used in the analytical model are listed in Table 4.3 and the gains for the consensus control are listed in Table 4.4. The topology of this grid-connected microgrid is shown in Fig. 4.18. The microgrid includes three BESS and a load connected at the PCC bus. A transfer $T4$ is used between the microgrid and the grid. It shifts up the voltage level from 18 kV to 230 kV and its impedance is 0.069 pu.

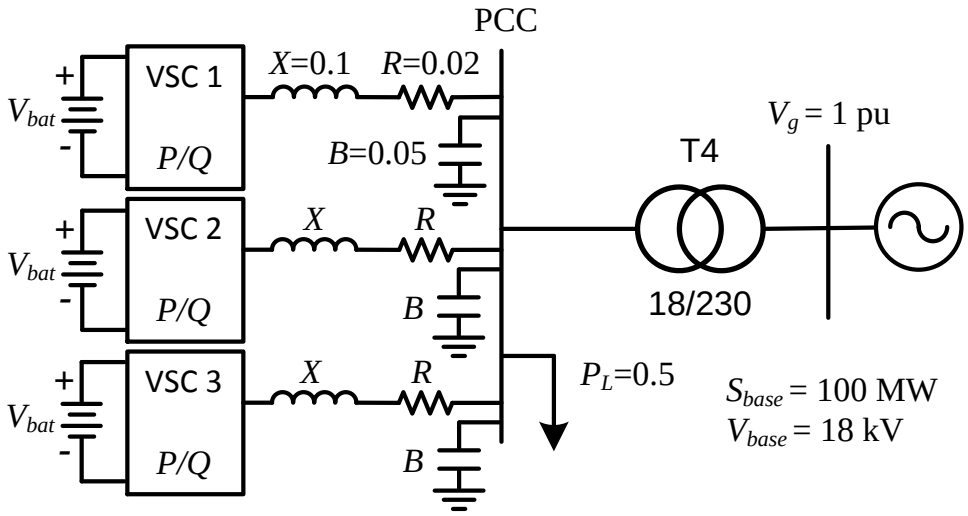

Figure 4.18: The topology of the grid-connected microgrid with three BESS.

Fig. 4.17 shows the diagram of the analytical model with control loops corresponding to Fig. 4.18. Each BESS has its own vector control system and the PLL but they use the same structure and parameters. The details of VSC 1 are presented while the insides of another two VSCs are omitted to save the space. The details on dynamic modeling can be found in [68]. The consensus control is boxed by the red dashed line. The inputs are energy (SoC) and power from each BESS while the outputs are the real power references for three BESS. The initial energy and power can be set in the integrator of $\frac{1}{s}$ and $\frac{-1}{3600s}$ in Fig. 4.17.

Fig. 4.19 shows the simulation results from the analytical model. At the beginning, the energy of three energy storage systems were 85%, 80%, and 90% respectively. Due to the fixed power

references, the first energy storage system (VSC 1) generated 0.5 pu power while another two energy storage systems (VSC 2, VSC 3) generated 0.2 pu power each. At 100 sec, the consensus control was activated. After 1600 sec, the power and energy were converged.

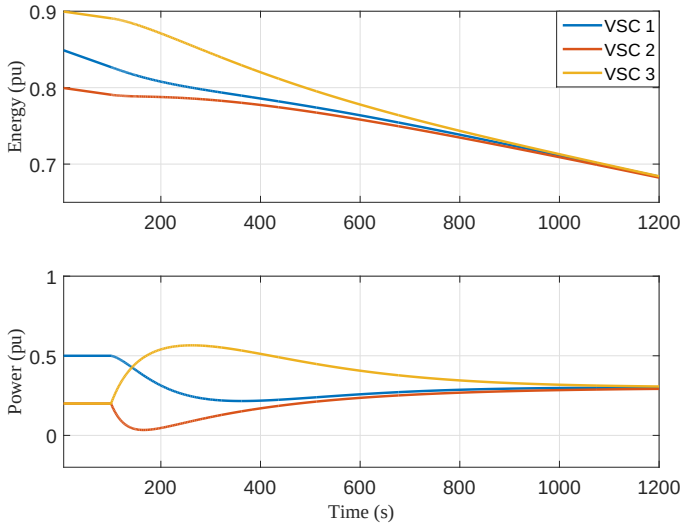

Figure 4.19: Simulation results from the analytical model.

4.3.3 CHIL Testbed

To verify the results generated by the analytical model, a detailed EMT model including an IEEE-9 bus system and three energy storage systems was built in MATLAB/SimPowerSystems. Due to the limitation of the host PC, it is simulated by the real-time simulator (RT-LAB). The circuit part was simulated by RT-LAB but three energy storage systems were controlled by the FPGA-based controllers from National Instrument (sbRIO 9606).

4.3.3.1 Topology of Testbed

The topology of the circuit is shown in Fig. 4.20. A microgrid with three energy storage systems was integrated into the grid. The grid was represented by the IEEE 9-bus system including three synchronous generators. The parameters and power flow for the IEEE-9 bus system are based on the standard 9-bus system data [88]. The parameters are listed in Table 4.6 and Table 4.5. Power

Table 4.5: Lines of IEEE 9-bus

Bus # from	Bus # to	R(pu)	X(pu)	B/2(pu)
4	5	0.010	0.085	0.088
4	6	0.017	0.092	0.079
5	7	0.032	0.161	0.153
6	9	0.039	0.170	0.179
7	8	0.0085	0.072	0.0745
8	9	0.0119	0.1008	0.1045

flows are marked in Fig. 4.20. The microgrid is integrated at Bus 9. Three energy storage systems totally generated 90 MW real power. Because of a 50 MW resistive load integrated at the PCC bus, only 40 MW power is transferred to the grid through a transformer under the initial condition. To keep the standard power flow of the IEEE 9-bus system, the real power from Generator 3 is reduced by 40 MW.

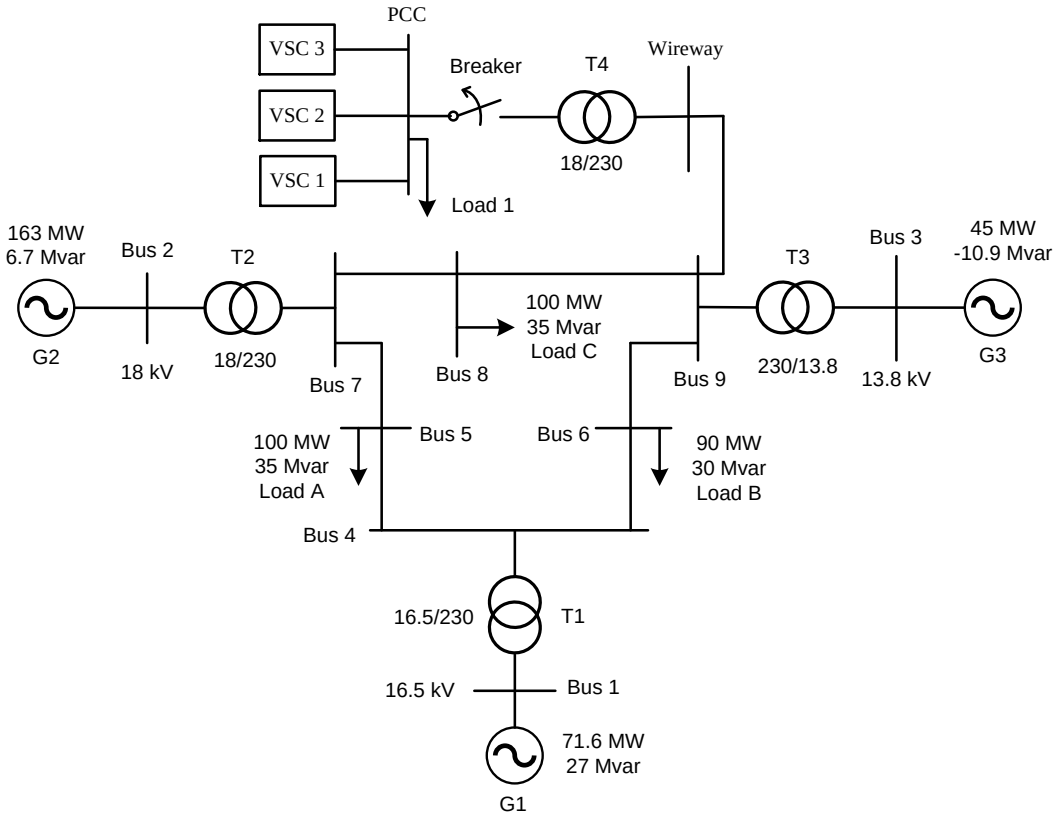

Figure 4.20: The microgrid including three BESS is integrated into IEEE 9-Bus system.

Table 4.6: Synchronous generators in IEEE 9-bus

Generator	1	2	3
Rated MVA	247.5	192.0	128.0
kV	16.5	18.0	13.8
Type	247.5	192.0	128.0
X_T(pu)	0.0576	0.0625	0.0586

4.3.3.2 Configuration of Testbed

The configuration of the CHIL testbed is shown in Fig. 4.21. The circuit which is shown in Fig. 4.20 is simulated in RT-LAB while the control loops for three energy storage systems are designed on three sbRIOs respectively using LabVIEW. The measurements for vector controls are sent to sbRIOs via the analog output channels of RT-LAB. The measurements include the SoC, three-phase voltages and currents at the PCC bus for each energy storage system. Meanwhile, sbRIOs send the control voltages back to RT-LAB to control VSCs in RT-LAB. In addition, the consensus control is implemented for energy storage systems so the communication paths need to be established between every two sbRIOs based on Fig. 4.16. The paths are used to transfer the power and energy signals for batteries. Fig. 4.22 shows the photos of the physical CHIL testbed built in our lab.

4.3.4 Experimental Results

In the case study, the consensus control was tested under two modes, grid-connected mode and islanded mode. When the grid was connected, the control loops were the same as Fig. 4.17. When the grid was disconnected, VSC 1 became the grid-forming inverter by switching the control mode from P/Q control to V/f control. Meanwhile, the consensus control for VSC 1 became deactivated and the consensus control for VSC 2 was only related to E_3 and P_3.

4.3.4.1 Grid-connected Mode

When the microgrid was connected to the IEEE-9 bus system, three energy storage systems belonged to grid-following IBRs with PQ control mode. Under the initial condition, VSC 1 generated 50 MW real power while VSC 2 and 3 generated 20 MW real power each. Fig .4.23 shows

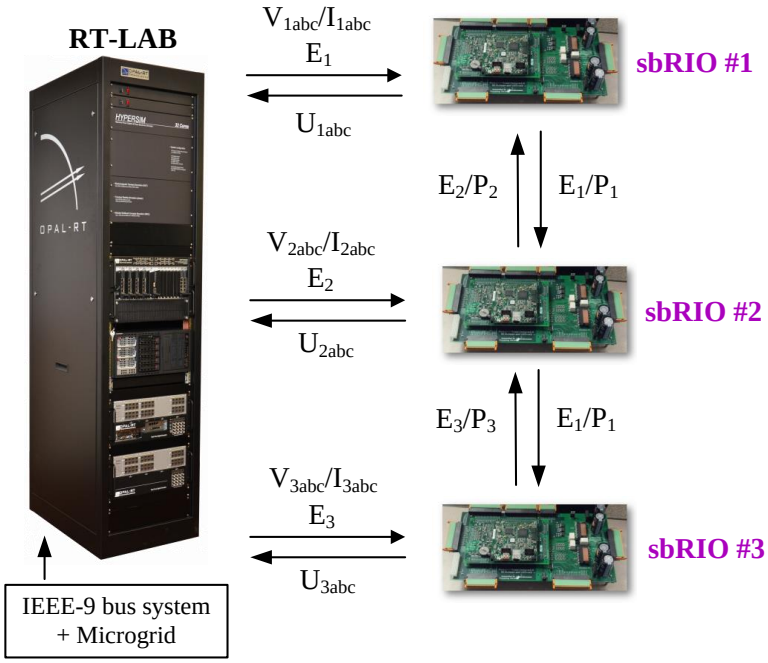

Figure 4.21: The overview of CHIL testbed.

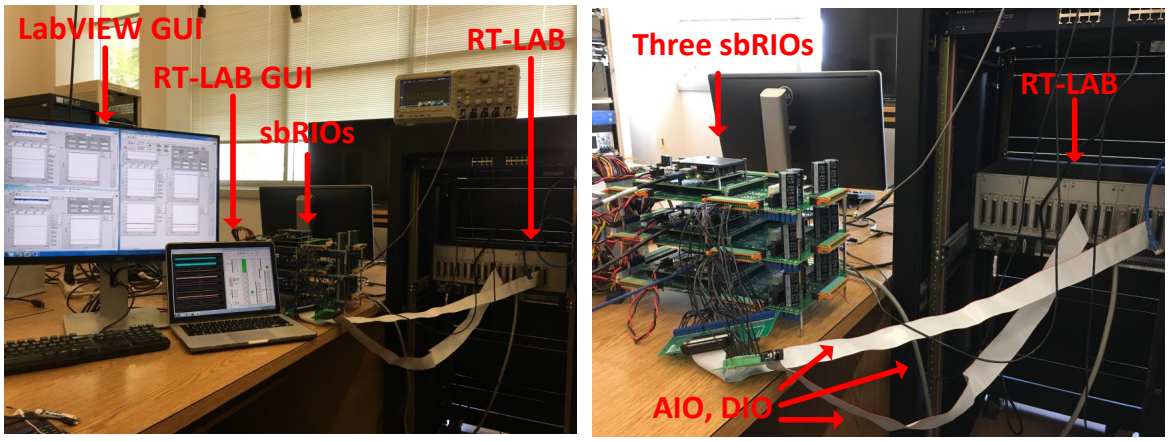

(a) (b)

Figure 4.22: (4.22a) Physical CHIL testbed built in our lab. (4.22b) zoom-in photo to show the detailed connections of RT-LAB and sbRIOs.

the dynamics of VSCs and IEEE-9 bus system. Before 60 sec, the VSCs were controlled by the controllers in RT-LAB. In other words, everything was simulated in RT-LAB before 60 sec. At 60 sec, the VSCs were controlled by sbRIOs. Because the measurements and control signals were transferred through the analog ports, the obvious noise appeared in the dynamic responses after

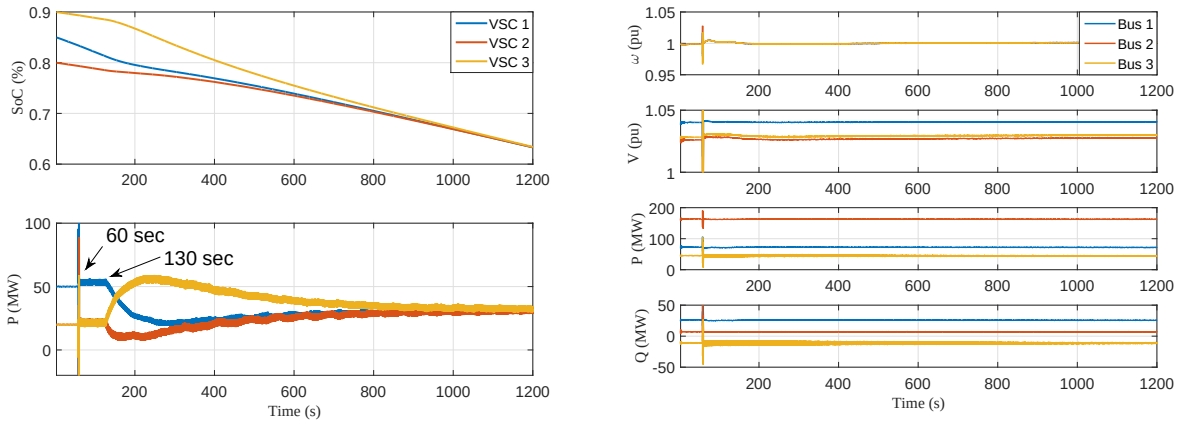

(a) (b)

Figure 4.23: Real-time results: under grid-connected mode, the energy and power of three energy storage systems were converged by the consensus control. 4.23a Dynamics of VSCs. 4.23b Dynamics of IEEE 9 bus system.

60 sec. At 130 sec, the consensus control was activated for all BESS. Around 1100 sec, the energy and power were converged by the consensus control.

4.3.4.2 Islanded Mode

Under the islanded mode, there were only VSC 2 and VSC 3 controlled by the consensus control. Fig. 4.24 shows the dynamics of the microgrid and IEEE-9 bus system. At 55 sec, sbRIOs started to control VSCs in RT-LAB. At 108 sec, the consensus control was activated for three BESS. At 225 sec, the microgrid was disconnected from the grid. It caused that IEEE 9 bus system lost 40 MW real power from the microgrid such that the frequency of the IEEE 9 bus system was reduced by 4%.

In the microgrid, three BESS supplied one 50 MW load. VSC 1 was switched to V/f mode while VSC 2 and VSC 3 were still with PQ control. Therefore, VSC 2 and VSC 3 still generated 20 MW each and VSC 1 generated 10 MW. As noted, the consensus control can only be implemented on the inverter with the power order vector control. Hence, after 220 sec, the consensus control only worked on VSC 2 and VSC 3. Based on Fig. 4.24a, we found that the energy and power of VSC 2 and VSC 3 were converged after 1100 sec.

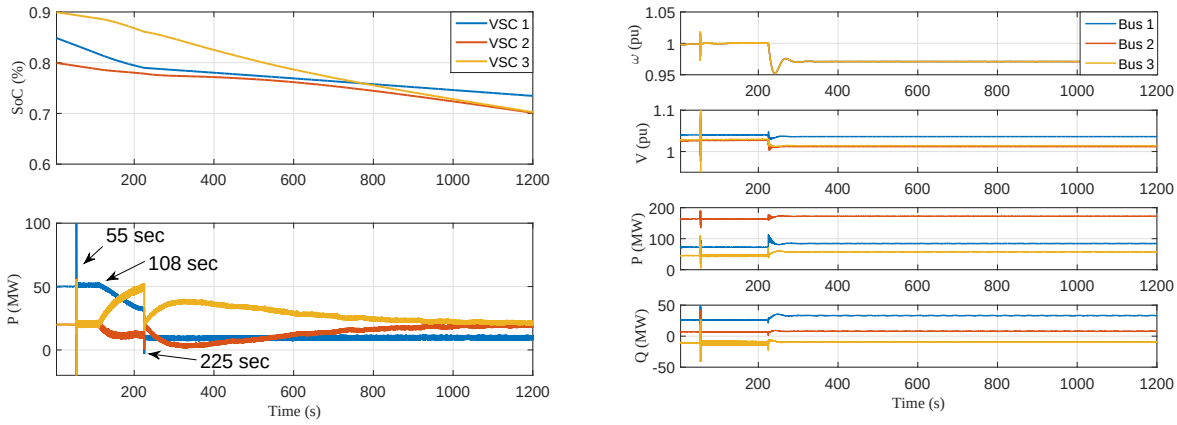

(a) (b)

Figure 4.24: Real-time results: under islanded mode, the energy and power of three energy storage systems were converged by the consensus control. 4.24a Dynamics of VSCs. 4.24b Dynamics of IEEE 9 bus system.

4.4 Conclusion

This chapter focuses on the coordinate controls for RES and BESS in the microgrid including the stability issues and the evaluation. The stability issue is conducted based on the microgrid including two DERs with by V-I droop. The corresponding analytical models are derived for both autonomous mode and grid-connected mode. Based on the eigenvalue analysis, it is identified that the small droop coefficients have a negative influence on system stability. In addition, the effect of grid strength and transmission line networks on this type of stability issue are investigated as well. The findings in the stability analysis are also validated by the detailed simulation results.

Different than V-I droop, the consensus control is designed for BESS specially. When it synchronizes the output power of each BESS, it also makes the consensus on the energy of each battery. To avoid the long simulation time of a detailed testbed, an analytical model for the grid-connected microgrid with three BESS is derived. The consensus control is implemented on it and evaluated by the time-domain simulation results. The highlight of this section is the CHIL testbed. The consensus control is tested under the grid-connected mode, autonomous mode, and the transient of mode switching. The real-time simulation results validate the performance of consensus control.

Chapter 5: Conclusion and Future Work

5.1 Conclusion

This dissertation focuses on the dynamic modeling and controls of the renewable energy sources in two main areas, conventional grid and microgrid. The conventional grid is also divided into the weak grid and the series compensated grid. For each area, the investigation is started with the stability issues of RES from the real-world records or literature review. The problems behind these stability issues are stated to excite the interests of investigations. Then, the analytical models are derived for the specific issues using the techniques of dynamic modeling. Based on the analytical models, the eigenvalue analysis is generated because it contains the critical information of the system such as oscillation modes and margin conditions. After comparing the critical information of the system with different dynamics, answers to the problems behind these stability issues can be found. Meanwhile, suitable solutions are proposed based on the answers. Moreover, the kinds of testbeds are important for the investigation of RES as well. They provide strong evidence to support the analytical results. Regardless of analytical models and testbeds, the modeling of RES in conventional grid is considered as the aggregated single inverter while the modeling of RES in the microgrid is considered as the multiple inverters rather than aggregated one. Three areas are concluded in the following paragraphs.

Chapter 2 presents my research results for RES in weak grid. Although the stability issues in weak grid have been studied widely, the SSO in Type-4 wind and torsional interaction in the western region of China are never studied. An analytical model is derived including all the essential dynamics of Type-4 wind in weak grid. According to the eigenvalue analysis from the analytical model, there are two modes that are very sensitive to the strength of the grid. Then, the participation analysis is used to determine the PLL dynamics as the critical factor. This finding is

validated by the EMT testbed which uses realistic parameters and control systems. Then, stability control is proposed based on the mechanism behind stability issues in weak grid. The stability control has two strategies corresponding to two feedback signals, current-based and voltage-based. Both strategies are evaluated using two analytical models that employ the power control mode and dc-link voltage control mode respectively. The eigenvalue analysis shows that the Type-4 wind with stability control can be stable even if $SCR = 1$. The performance is better than existing approaches. Furthermore, the stability control is also evaluated using two EMT testbeds, Type-3 wind and Type-4 wind. As noted, it is implemented in the RSC of Type-3 wind while it is implemented in the GSC of Type-4 wind. Based on the EMT simulation results, the performance of stability control in the EMT testbed is not as good as the analytical model although both models use the same parameters. The reason is the current limitations in the EMT testbed and it is presented by the simulation results. Another conclusion based on the EMT simulation results is that the voltage-based control strategy is preferred because it has the better performance. Furthermore, an FPGA-based hardware testbed is built up to test stability control. In the hardware testbed, a single inverter with the power control mode is connected to the weak grid and the voltage-based strategy is implemented. The experiment results validate the performance of stability control as well.

Chapter 3 presents the procedure of replication of real-world SSR events in Texas. The objective of this chapter is to find out which reason caused the different consequences in these three real-world events. In this chapter, the stability issues in the series compensated networks are investigated using another way. The complex EMT testbed is built first to replicate the events; then, the eigenvalue loci is generated to validate the EMT simulation results. Before showing the replication results, this chapter introduces the challenges during the replication and provides the solutions to overcome them. The sensitivity analysis contains the EMT simulation results and the eigenvalue loci from the equivalent analytical model. Using the EMT testbed with the found information and estimated parameters, the replication results are generated and match the real-world record very well. Finally, an improved SSR control is implemented in the EMT testbed to mitigate SSR. The improvement is using the local current signals to replace the remote voltage signals. The improved SSR control is

tested under different conditions and the SSR is mitigated obviously based on the EMT simulation results.

Chapter 4 presents my research results on RES and BESS in microgrids. The same microgrid may have different types and sizes of DERs. However, even if DERs have the same type and parameters, they may operate under different conditions and the coordinate controls should be considered. Hence, different from the above two chapters, the investigation in this chapter uses the multi-inverters model rather than the aggregated single-inverter model. First, the multi-inverters analytical model is used to investigate the stability issues in the microgrid including two DERs with V-I droop. The analytical model is derived using the multi-inputs-multi-outputs matrix. Based on the eigenvalue loci from the analytical model, it is found that the small droop coefficients have negative effects on the stability of microgrid under islanded mode. However, there is an exception. When two DERs have the same droop coefficients, the system will not be unstable even if they are small. Moreover, the effect of grid strength is investigated as well. When the microgrid is connected to the strong grid, the small droop coefficients will not cause the oscillation issues. The second coordinate control in this chapter is consensus control which is used to achieve the consensus on multiple BESS in the microgrid. To evaluate the consensus control, an analytical model and a CHIL testbed are built up. In the analytical model, the microgrid with three BESS is connected to the infinite bus while it is connected to the IEEE 9-bus system in the CHIL testbed. The function of consensus is validated by the analytical model and CHIL testbed.

5.2 Future Work

The above chapters do not only show my research results on stability analysis and controls of RES but also provide an approach to investigate RES in conventional grid and microgrid. Using three tools mentioned in Chapter 1, more investigations on other issues of RES can be conducted from linear analysis to the time-domain simulation results, from EMT testbeds to hardware testbeds. The following subsections will show the detailed topics I would like to continue in the future.

5.2.1 Multi-inverters Modeling of RES in Grid

In many existing studies, the interactions among RES units in the same farm are not considered to investigate the stability issues of RES in grid. However, is there any internal interaction among RES units in farms? Do these internal interactions affect the stability of farms in the weak grid? If so, how do they affect stability? My future work will try to answer these questions using the above tools. Obviously, the aggregated single-inverter model cannot be used because it omits the internal dynamics. The multi-inverters model will be used because it has more dynamics to present the interactions in the wind farm or PV farm. The analytical model based on multiple inverters has been derived for the microgrid. It can be modified by adding more characteristics of farms to generate the eigenvalue analysis. Then, the participation factor can be used to find which states are related to the dominant modes. Another method to identify the internal interactions is replacing one RES unit with a controllable current source. The current source can generate the power as the unit but it does not have the control systems so this method can be used to detect the interactions which are caused by different units' control systems.

Furthermore, EMT testbeds need to be improved by adding more wind or PV modules. The structure of the testbed should follow the analytical model. Based on the EMT testbed, we can create more complex dynamic events and generate more practical simulation results. Certainly, more RES modules in the EMT testbed may cause the tons of calculation tasks to exceed the capability of PC. Hence, the EMT testbeds will be converted into the RT-LAB model when it is too complex. The RT-LAB cannot only handle more complex EMT testbeds but also provides real-time simulation results.

5.2.2 Interactions Between Microgrids and Large-scale Systems

To improve the quality of research on renewable energy in the microgrid, more interactions between microgrids and large-scale power systems need to be studied. In most of my existing studies, the grid is always considered as the infinite bus and emulated by the constant voltage source so stability issues in the grid cannot be modeled. However, the electric grid in the real-world has more complex structure and kinds of stability issues such as cascading issues. To produce more

realistic results, the grid should be modeled using a large-scale power system including multiple synchronous generators and loads. With the large-scale power system as the grid, the microgrid will not only experience the stability issues caused by itself but also the instabilities caused by the grid. Therefore, to improve the reliability of microgrid, more questions need to be concerned such as how these stability issues in the grid affect the microgrid, what performance the coordinate control has on the instability, and how to improve the capability of the microgrid.

The CHIL testbed built for consensus control can be used to address these concerns by generating the real-time simulation results. In that testbed, the ideal grid is already replaced by the IEEE 9-bus system. The frequency responses of the large-scale system are plotted in Chapter 4. Therefore, the investigation on interactions between microgrids and large-scale systems can be started from the CHIL testbed. It provides a feasible environment to test the microgrid with kinds of DERs and coordinate controls using the real-time simulator and physical controllers. The reliability of microgrid with the consensus control has been tested under grid-connected mode and islanded mode using the CHIL testbed. In the near future, its reliability on the instability events in IEEE 9-bus system will be evaluated. Meanwhile, the droop control will be implemented in the CHIL testbed and its performance will be compared with the consensus control. Besides the CHIL testbed, the analytical model needs to be derived to explore the mechanism and critical factor behind the unstable phenomena. Currently, the analytical model includes the dynamics of multiple DERs in the microgrid. In the future, I will improve it by adding the dynamics of the synchronous generator and more complex power systems.

References

[1] M. Farrokhabadi, C. A. Canizares, J. W. Simpson-Porco, E. Nasr, L. Fan, P. Mendoza-Araya, R. Tonkoski, U. Tamrakar, N. D. Hatziargyriou, D. Lagos, R. W. Wies, M. Paolone, M. Liserre, L. Meegahapola, M. Kabalan, A. H. Hajimiragha, D. Peralta, M. Elizondo, K. P. Schneider, F. Tuffner, and J. T. Reilly, "Microgrid stability definitions, analysis, and examples," *IEEE Transactions on Power Systems*, pp. 1–1, 2019.

[2] E. Ebrahimzadeh, F. Blaabjerg, X. Wang, and C. L. Bak, "Harmonic stability and resonance analysis in large pmsg-based wind power plants," *IEEE Transactions on Sustainable Energy*, vol. 9, no. 1, pp. 12–23, Jan 2018.

[3] K. Givaki, D. Chen, and L. Xu, "Current error based compensations for vsc current control in weak grids for wind farm applications," *IEEE Transactions on Sustainable Energy*, vol. 10, no. 1, pp. 26–35, Jan 2019.

[4] K. M. Alawasa, Y. A. I. Mohamed, and W. Xu, "Modeling, analysis, and suppression of the impact of full-scale wind-power converters on subsynchronous damping," *IEEE Systems Journal*, vol. 7, no. 4, pp. 700–712, Dec 2013.

[5] H. Liu, X. Xie, J. He, T. Xu, Z. Yu, C. Wang, and C. Zhang, "Subsynchronous interaction between direct-drive pmsg based wind farms and weak ac networks," *IEEE Transactions on Power Systems*, vol. 32, no. 6, pp. 4708–4720, Nov 2017.

[6] V. Akhmatov and H. Knudsen, "An aggregate model of a grid-connected, large-scale, offshore wind farm for power stability investigationsimportance of windmill mechanical system," *International Journal of Electrical Power and Energy Systems*, vol. 24, no. 9, pp. 709 – 717, 2002. [Online]. Available: http://www.sciencedirect.com/science/article/pii/S0142061501000898

[7] S.-H. Huang, J. Schmall, J. Conto, J. Adams, Y. Zhang, and C. Carter, "Voltage control challenges on weak grids with high penetration of wind generation: Ercot experience," in *Power and Energy Society General Meeting, 2012 IEEE*. IEEE, 2012, pp. 1–7.

[8] L. Fan, "Modeling type-4 wind in weak grids," *IEEE Transactions on Sustainable Energy*, pp. 1–1, 2018.

[9] J. Hu, Q. Hu, B. Wang, H. Tang, and Y. Chi, "Small signal instability of pll-synchronized type-4 wind turbines connected to high-impedance ac grid during lvrt," *IEEE Transactions on Energy Conversion*, vol. 31, no. 4, pp. 1676–1687, Dec 2016.

[10] N. P. W. Strachan and D. Jovcic, "Stability of a variable-speed permanent magnet wind generator with weak ac grids," *IEEE Transactions on Power Delivery*, vol. 25, no. 4, pp. 2779–2788, Oct 2010.

[11] J. Z. Zhou, H. Ding, S. Fan, Y. Zhang, and A. M. Gole, "Impact of short-circuit ratio and phase-locked-loop parameters on the small-signal behavior of a vsc-hvdc converter," *IEEE Transactions on Power Delivery*, vol. 29, no. 5, pp. 2287–2296, 2014.

[12] L. Papangelis, M.-S. Debry, T. Prevost, P. Panciatici, and T. Van Cutsem, "Stability of a voltage source converter subject to decrease of short-circuit capacity: a case study," *Proceedings of the 20th PSCC*, 2017.

[13] L. Fan and Z. Miao, "Wind in weak grids: 4 hz or 30 hz oscillations?" *IEEE Transactions on Power Systems*, vol. 33, no. 5, pp. 5803–5804, Sept 2018.

[14] J. Hu, B. Wang, W. Wang, H. Tang, Y. Chi, and Q. Hu, "Small signal dynamics of dfig-based wind turbines during riding through symmetrical faults in weak ac grid," *IEEE Transactions on Energy Conversion*, vol. 32, no. 2, pp. 720–730, 2017.

[15] H. Yuan, X. Yuan, and J. Hu, "Modeling of grid-connected vscs for power system small-signal stability analysis in dc-link voltage control timescale," *IEEE Transactions on Power Systems*, vol. 32, no. 5, pp. 3981–3991, Sep. 2017.

[16] W. He, X. Yuan, and J. Hu, "Inertia provision and estimation of pll-based dfig wind turbines," *IEEE Transactions on Power Systems*, vol. 32, no. 1, pp. 510–521, Jan 2017.

[17] C. Zhan, C. Fitzer, V. K. Ramachandaramurthy, A. Arulampalam, M. Barnes, and N. Jenkins, "Software phase-locked loop applied to dynamic voltage restorer (dvr)," in *2001 IEEE Power Engineering Society Winter Meeting. Conference Proceedings (Cat. No.01CH37194)*, vol. 3, Jan 2001, pp. 1033–1038 vol.3.

[18] D. Jovcic, "Phase locked loop system for facts," *IEEE Transactions on Power Systems*, vol. 18, no. 3, pp. 1116–1124, Aug 2003.

[19] P. Rodrguez, R. Teodorescu, I. Candela, A. V. Timbus, M. Liserre, and F. Blaabjerg, "New positive-sequence voltage detector for grid synchronization of power converters under faulty grid conditions," in *2006 37th IEEE Power Electronics Specialists Conference*, June 2006, pp. 1–7.

[20] P. Rodriguez, J. Pou, J. Bergas, J. I. Candela, R. P. Burgos, and D. Boroyevich, "Decoupled double synchronous reference frame pll for power converters control," *IEEE Transactions on Power Electronics*, vol. 22, no. 2, pp. 584–592, March 2007.

[21] M. Wei and Z. Chen, "A fast pll method for power electronic systems connected to distorted grids," in *IECON 2007 - 33rd Annual Conference of the IEEE Industrial Electronics Society*, Nov 2007, pp. 1702–1707.

[22] A. Dissanayaka, J. Wiebe, and A. Isaacs. (2018, March) Panhandle and South Texas Stability and System Strength Assessment. Electranix.

[23] X. Yuan, F. Wang, D. Boroyevich, Y. Li, and R. Burgos, "Dc-link voltage control of a full power converter for wind generator operating in weak-grid systems," *IEEE Transactions on Power Electronics*, vol. 24, no. 9, pp. 2178–2192, Sept 2009.

[24] H. T. Ma, P. B. Brogan, K. H. Jensen, and R. J. Nelson, "Sub-synchronous control interaction studies between full-converter wind turbines and series-compensated ac transmission lines," in *2012 IEEE Power and Energy Society General Meeting*, July 2012, pp. 1–5.

[25] L. Zhang, L. Harnefors, and H. P. Nee, "Power-synchronization control of grid-connected voltage-source converters," *IEEE Transactions on Power Systems*, vol. 25, no. 2, pp. 809–820, May 2010.

[26] J. Alipoor, Y. Miura, and T. Ise, "Power system stabilization using virtual synchronous generator with alternating moment of inertia," *IEEE Journal of Emerging and Selected Topics in Power Electronics*, vol. 3, no. 2, pp. 451–458, 2015.

[27] K. Givaki, D. Chen, and L. Xu, "Current error based compensations for vsc current control in weak grid for wind farm applications," *IEEE Transactions on Sustainable Energy*, pp. 1–1, 2018.

[28] A. Egea-Alvarez, S. Fekriasl, F. Hassan, and O. Gomis-Bellmunt, "Advanced vector control for voltage source converters connected to weak grids," *IEEE Transactions on Power Systems*, vol. 30, no. 6, pp. 3072–3081, Nov 2015.

[29] L. Fan and Z. Miao, "An explanation of oscillations due to wind power plants weak grid interconnection," *IEEE trans. Sustainable Energy*, vol. 9, no. 1, pp. 488–490, Jan 2018.

[30] Y. Xu, M. Zhang, L. Fan, and Z. Miao, "Small-signal stability analysis of type-4 wind in series compensated networks," *IEEE Transactions on Energy Conversion*, pp. 1–1, 2019.

[31] G. Irwin, *Sub-synchronous interactions with wind turbines.* presented at the Technical Conf. CREZ System Design and Operation, 2010, vol. 27.

[32] A. Jindal, G. Irwin, and A. Woodord, *Sub-synchronous interactions with wind farms connected near series compensated ac lines.* presented at the Workshop on large scale integration of wind, 2010, vol. 14.

[33] X. Xie, X. Zhang, H. Liu, H. Liu, Y. Li, and C. Zhang, "Characteristic analysis of subsynchronous resonance in practical wind farms connected to series-compensated transmissions," *IEEE Transactions on Energy Conversion*, vol. 32, no. 3, pp. 1117–1126, Sept 2017.

[34] L. Fan, C. Zhu, Z. Miao, and M. Hu, "Modal analysis of a dfig-based wind farm interfaced with a series compensated network," *IEEE Transactions on Energy Conversion*, vol. 26, no. 4, pp. 1010–1020, Dec 2011.

[35] Z. Miao, "Impedance-model-based ssr analysis for type 3 wind generator and series-compensated network," *IEEE Transactions on Energy Conversion*, vol. 27, no. 4, pp. 984–991, Dec 2012.

[36] S. Huang and Y. Gong, *South Texas SSR.* ERCOT ROS Meeting, May, 2018, vol. 14.

[37] J. Adams, V. A. Pappu, and A. Dixit, "Ercot experience screening for sub-synchronous control interaction in the vicinity of series capacitor banks," in *2012 IEEE Power and Energy Society General Meeting*, July 2012, pp. 1–5.

[38] G. D. Irwin, A. K. Jindal, and A. L. Isaacs, "Sub-synchronous control interactions between type 3 wind turbines and series compensated ac transmission systems," in *2011 IEEE Power and Energy Society General Meeting*, July 2011, pp. 1–6.

[39] M. Sahni, B. Badrzadeh, D. Muthumuni, Y. Cheng, H. Yin, S. . Huang, and Y. Zhou, "Sub-synchronous interaction in wind power plants- part ii: An ercot case study," in *2012 IEEE Power and Energy Society General Meeting*, July 2012, pp. 1–9.

[40] M. Sahni, D. Muthumuni, B. Badrzadeh, A. Gole, and A. Kulkarni, "Advanced screening techniques for sub-synchronous interaction in wind farms," in *PES T D 2012*, May 2012, pp. 1–9.

[41] N. Karnik, D. Novosad, H. K. Nia, M. Sahni, M. Ghavami, and H. Yin, "An evaluation of critical impact factors for ssci analysis for wind power plants: A utility perspective," in *2017 IEEE Power Energy Society General Meeting*, July 2017, pp. 1–5.

[42] Y. Cheng, M. Sahni, D. Muthumuni, and B. Badrzadeh, "Reactance scan crossover-based approach for investigating ssci concerns for dfig-based wind turbines," *IEEE Transactions on Power Delivery*, vol. 28, no. 2, pp. 742–751, April 2013.

[43] Y. Cheng, S. Huang, J. Rose, V. Pappu, and J. Conto, "Subsynchronous resonance assessment for a large system with multiple series compensated transmission circuits," *IET Renewable Power Generation*, no. 3, Aug 2018.

[44] R. K. Varma, S. Auddy, and Y. Semsedini, "Mitigation of subsynchronous resonance in a series-compensated wind farm using facts controllers," *IEEE Transactions on Power Delivery*, vol. 23, no. 3, pp. 1645–1654, July 2008.

[45] M. S. El-Moursi, B. Bak-Jensen, and M. H. Abdel-Rahman, "Novel statcom controller for mitigating ssr and damping power system oscillations in a series compensated wind park," *IEEE Transactions on Power Electronics*, vol. 25, no. 2, pp. 429–441, Feb 2010.

[46] L. Fan and Z. Miao, "Mitigating ssr using dfig-based wind generation," *IEEE Transactions on Sustainable Energy*, vol. 3, no. 3, pp. 349–358, July 2012.

[47] A. E. Leon and J. A. Solsona, "Sub-synchronous interaction damping control for dfig wind turbines," *IEEE Transactions on Power Systems*, vol. 30, no. 1, pp. 419–428, Jan 2015.

[48] N. Hatziargyrious, H. Asano, R. Iravani, and C. Marnay, *Microgrids.* IEEE Power Energy Mag, 2007.

[49] A. Hirsch, Y. Parag, and J. Guerrero, "Microgrids: A review of technologies, key drivers, and outstanding issues," *Renewable and Sustainable Energy Reviews*, vol. 90, pp. 402 – 411, 2018. [Online]. Available: http://www.sciencedirect.com/science/article/pii/S136403211830128X

[50] D. E. Olivares, A. Mehrizi-Sani, A. H. Etemadi, C. A. Caizares, R. Iravani, M. Kazerani, A. H. Hajimiragha, O. Gomis-Bellmunt, M. Saeedifard, R. Palma-Behnke, G. A. Jimnez-Estvez, and N. D. Hatziargyriou, "Trends in microgrid control," *IEEE Transactions on Smart Grid*, vol. 5, no. 4, pp. 1905–1919, July 2014.

[51] A. Bernstein, J. Le Boudec, L. Reyes-Chamorro, and M. Paolone, "Real-time control of microgrids with explicit power setpoints: Unintentional islanding," in *2015 IEEE Eindhoven PowerTech*, June 2015, pp. 1–6.

[52] W. Yao, M. Chen, J. Matas, J. M. Guerrero, and Z. M. Qian, "Design and analysis of the droop control method for parallel inverters considering the impact of the complex impedance on the power sharing," *IEEE Transactions on Industrial Electronics*, vol. 58, no. 2, pp. 576–588, Feb 2011.

[53] M. S. Golsorkhi and D. D. C. Lu, "A control method for inverter-based islanded microgrids based on V-I droop characteristics," *IEEE Transactions on Power Delivery*, vol. 30, no. 3, pp. 1196–1204, Jun 2015.

[54] W. R. Issa, M. A. Abusara, and S. M. Sharkh, "Impedance interaction between islanded parallel voltage source inverters and the distribution network," in *Power Electronics, Machines and Drives (PEMD 2014), 7th IET International Conference on*, Apr 2014, pp. 1–6.

[55] C. C. Chang, D. Gorinevsky, and S. Lall, "Stability analysis of distributed power generation with droop inverters," *IEEE Transactions on Power Systems*, vol. 30, no. 6, pp. 3295–3303, Nov 2015.

[56] R. Majumder, B. Chaudhuri, A. Ghosh, R. Majumder, G. Ledwich, and F. Zare, "Improvement of stability and load sharing in an autonomous microgrid using supplementary droop control loop," in *IEEE PES General Meeting*, July 2010, pp. 1–1.

[57] Z. Miao, A. Domijan, and L. Fan, "Investigation of microgrids with both inverter interfaced and direct ac-connected distributed energy resources," *IEEE Transactions on Power Delivery*, vol. 26, no. 3, pp. 1634–1642, Jul 2011.

[58] F. Cavazzana, P. Mattavelli, M. Corradin, and I. Toigo, "Grid sensitivity considerations on multiple parallel inverters systems," in *2016 IEEE 8th International Power Electronics and Motion Control Conference (IPEMC-ECCE Asia)*, May 2016, pp. 993–999.

[59] C. N. Rowe, T. J. Summers, R. E. Betz, D. J. Cornforth, and T. G. Moore, "Arctan power x2013;frequency droop for improved microgrid stability," *IEEE Transactions on Power Electronics*, vol. 28, no. 8, pp. 3747–3759, Aug 2013.

[60] A. M. Bouzid, J. M. Guerrero, A. Cheriti, M. Bouhamida, P. Sicard, and M. Benghanem, "A survey on control of electric power distributed generation systems for microgrid applications," *Renewable and Sustainable Energy Reviews*, vol. 44, pp. 751 – 766, 2015. [Online]. Available: http://www.sciencedirect.com/science/article/pii/S136403211500026X

[61] C. A. Hill, M. C. Such, D. Chen, J. Gonzalez, and W. M. Grady, "Battery energy storage for enabling integration of distributed solar power generation," *IEEE Transactions on Smart Grid*, vol. 3, no. 2, pp. 850–857, June 2012.

[62] J. Khazaei and Z. Miao, "Consensus control for energy storage systems," *IEEE Transactions on Smart Grid*, vol. 9, no. 4, pp. 3009–3017, July 2018.

[63] L. Fan, R. Kavasseri, Z. L. Miao, and C. Zhu, "Modeling of dfig-based wind farms for ssr analysis," *IEEE Transactions on Power Delivery*, vol. 25, no. 4, pp. 2073–2082, Oct 2010.

[64] H. J. Avelar, W. A. Parreira, J. B. Vieira, L. C. G. de Freitas, and E. A. A. Coelho, "A state equation model of a single-phase grid-connected inverter using a droop control scheme with extra phase shift control action," *IEEE Transactions on Industrial Electronics*, vol. 59, no. 3, pp. 1527–1537, Mar 2012.

[65] J. M. Guerrero, L. G. de Vicuna, J. Matas, M. Castilla, and J. Miret, "A wireless controller to enhance dynamic performance of parallel inverters in distributed generation systems," *IEEE Transactions on Power Electronics*, vol. 19, no. 5, pp. 1205–1213, Sep 2004.

[66] C. K. Sao and P. W. Lehn, "Autonomous load sharing of voltage source converters," *IEEE Transactions on Power Delivery*, vol. 20, no. 2, pp. 1009–1016, Apr 2005.

[67] T. L. Vandoorn, J. D. M. D. Kooning, B. Meersman, J. M. Guerrero, and L. Vandevelde, "Automatic power-sharing modification of p / v droop controllers in low-voltage resistive microgrids," *IEEE Transactions on Power Delivery*, vol. 27, no. 4, pp. 2318–2325, Oct 2012.

[68] Y. Li, L. Fan, and Z. Miao, "Wind in weak grids: Low-frequency oscillations, subsynchronous oscillations, and torsional interactions," *IEEE Transactions on Power Systems*, pp. 1–1, 2019.

[69] J. Johnson, R. Ablinger, R. Bründlinger, B. Fox, and J. Flicker, "Design and evaluation of sunspec-compliant smart grid controller with an automated hardware-in-the-loop testbed," *Technology and Economics of Smart Grids and Sustainable Energy*, vol. 2, no. 1, p. 16, Sep 2017. [Online]. Available: https://doi.org/10.1007/s40866-017-0032-7

[70] J. Johnson, R. Ablinger, R. Bruendlinger, B. Fox, and J. Flicker, "Interconnection standard grid-support function evaluations using an automated hardware-in-the-loop testbed," *IEEE Journal of Photovoltaics*, vol. 8, no. 2, pp. 565–571, March 2018.

[71] Y. Li, L. Fan, and Z. Miao, "Stability control for wind in weak grids," *IEEE Transactions on Sustainable Energy*, pp. 1–1, 2018.

[72] Y. Li, L. Fan, and Z. Miao, "Stability enhancement for grid-following voltage-source converters in weak grids: Design and validation via a hardware testbed," *IEEE Transactions on Sustainable Energy, submitted*, Dec 2019.

[73] J. Hu, Q. Hu, B. Wang, H. Tang, and Y. Chi, "Small signal instability of pll-synchronized type-4 wind turbines connected to high-impedance ac grid during lvrt," *IEEE Transactions on Energy Conversion*, vol. 31, no. 4, pp. 1676–1687, 2016.

[74] V. Kaura and V. Blasko, "Operation of a phase locked loop system under distorted utility conditions," *IEEE Transactions on Industry Applications*, vol. 33, no. 1, pp. 58–63, Jan 1997.

[75] S. Chung, "A phase tracking system for three phase utility interface inverters," *IEEE Transactions on Power Electronics*, vol. 15, no. 3, pp. 431–438, May 2000.

[76] N. W. Miller, J. J. Sanchez-Gasca, W. W. Price, and R. W. Delmerico, "Dynamic modeling of ge 1.5 and 3.6 mw wind turbine-generators for stability simulations," in *Power Engineering Society General Meeting, 2003, IEEE*, vol. 3. IEEE, 2003, pp. 1977–1983.

[77] IEEE SSR working group and others, "Second benchmark model for computer simulation of subsynchronous resonance," *IEEE Trans. on Power Apparatus and Systems*, vol. 104, no. 5, pp. 1057–1066, 1995.

[78] P. Kundur, *Power System Stability And Control*, ser. EPRI power system engineering series. McGraw-Hill, 1994. [Online]. Available: https://books.google.com/books?id=v3RxH_GkwmsC

[79] Y. Li, L. Fan, and Z. Miao, "Replicating real-world wind farm ssr events," *IEEE Transactions on Power Delivery*, pp. 1–1, 2019.

[80] E. T. Texas, *Rio Grande Valley Projects*. Electric Transmission Texas, 2016.

[81] ——, *New ETT 345-kV lines begin delivering power to LRGV*. Electric Transmission Texas, 2016, vol. 2.

[82] B. Cassell, *250-MW Hidalo Wind project in Texas due for commercial ops on Sept 23*. GenerationHub.com, 2016.

[83] N. W. Miller, J. J. Sanchez-Gasca, W. W. Price, and R. W. Delmerico, "Dynamic modeling of ge 1.5 and 3.6 mw wind turbine-generators for stability simulations," in *2003 IEEE Power Engineering Society General Meeting (IEEE Cat. No.03CH37491)*, vol. 3, July 2003, pp. 1977–1983 Vol. 3.

[84] Y. Li and L. Fan, "Stability analysis of two parallel converters with voltagecurrent droop control," *IEEE Transactions on Power Delivery*, vol. 32, no. 6, pp. 2389–2397, Dec 2017.

[85] A. Yazdani and R. Iravani, *Voltage-sourced converters in power systems: modeling, control, and applications*. John Wiley & Sons, 2010.

[86] A. Tazay, Z. Miao, and L. Fan, "Blackstart of an induction motor in an autonomous microgrid," in *Power Energy Society General Meeting, 2015 IEEE*, Jul 2015, pp. 1–5.

[87] A. Bidram, A. Davoudi, F. L. Lewis, and J. M. Guerrero, "Distributed cooperative secondary control of microgrids using feedback linearization," *IEEE Transactions on Power Systems*, vol. 28, no. 3, pp. 3462–3470, Aug 2013.

[88] A. F. P.M. Anderson, *Power System Control and Stability*. Iowa State University Press.

Appendix A: Reuse Permissions of Published Papers

The permission below is for Figure 1.1.

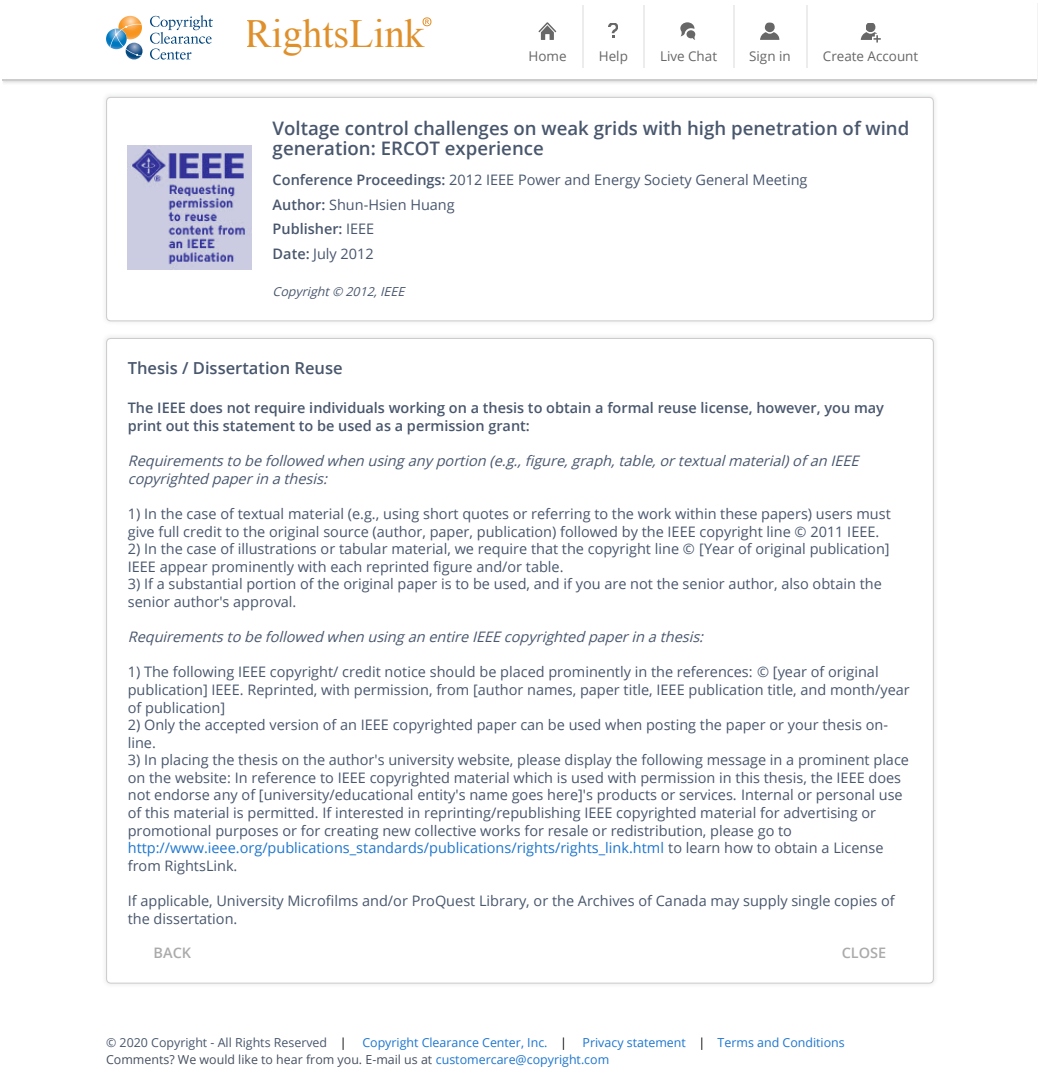

Copyright Clearance Center RightsLink®

Home | Help | Live Chat | Sign in | Create Account

IEEE Requesting permission to reuse content from an IEEE publication

Voltage control challenges on weak grids with high penetration of wind generation: ERCOT experience

Conference Proceedings: 2012 IEEE Power and Energy Society General Meeting

Author: Shun-Hsien Huang

Publisher: IEEE

Date: July 2012

Copyright © 2012, IEEE

Thesis / Dissertation Reuse

The IEEE does not require individuals working on a thesis to obtain a formal reuse license, however, you may print out this statement to be used as a permission grant:

Requirements to be followed when using any portion (e.g., figure, graph, table, or textual material) of an IEEE copyrighted paper in a thesis:

1) In the case of textual material (e.g., using short quotes or referring to the work within these papers) users must give full credit to the original source (author, paper, publication) followed by the IEEE copyright line © 2011 IEEE.
2) In the case of illustrations or tabular material, we require that the copyright line © [Year of original publication] IEEE appear prominently with each reprinted figure and/or table.
3) If a substantial portion of the original paper is to be used, and if you are not the senior author, also obtain the senior author's approval.

Requirements to be followed when using an entire IEEE copyrighted paper in a thesis:

1) The following IEEE copyright/ credit notice should be placed prominently in the references: © [year of original publication] IEEE. Reprinted, with permission, from [author names, paper title, IEEE publication title, and month/year of publication]
2) Only the accepted version of an IEEE copyrighted paper can be used when posting the paper or your thesis on-line.
3) In placing the thesis on the author's university website, please display the following message in a prominent place on the website: In reference to IEEE copyrighted material which is used with permission in this thesis, the IEEE does not endorse any of [university/educational entity's name goes here]'s products or services. Internal or personal use of this material is permitted. If interested in reprinting/republishing IEEE copyrighted material for advertising or promotional purposes or for creating new collective works for resale or redistribution, please go to http://www.ieee.org/publications_standards/publications/rights/rights_link.html to learn how to obtain a License from RightsLink.

If applicable, University Microfilms and/or ProQuest Library, or the Archives of Canada may supply single copies of the dissertation.

BACK CLOSE

The permission below is for Figure 1.2, Figure 1.3, and Figure 1.4.

Copyright Clearance Center RightsLink®

Home | Help | Live Chat | Sign in | Create Account

IEEE Requesting permission to reuse content from an IEEE publication

Subsynchronous Interaction Between Direct-Drive PMSG Based Wind Farms and Weak AC Networks

Author: Huakun Liu
Publication: Power Systems, IEEE Transactions on
Publisher: IEEE
Date: Nov. 2017

Copyright © 2017, IEEE

Thesis / Dissertation Reuse

The IEEE does not require individuals working on a thesis to obtain a formal reuse license, however, you may print out this statement to be used as a permission grant:

Requirements to be followed when using any portion (e.g., figure, graph, table, or textual material) of an IEEE copyrighted paper in a thesis:

1) In the case of textual material (e.g., using short quotes or referring to the work within these papers) users must give full credit to the original source (author, paper, publication) followed by the IEEE copyright line © 2011 IEEE.
2) In the case of illustrations or tabular material, we require that the copyright line © [Year of original publication] IEEE appear prominently with each reprinted figure and/or table.
3) If a substantial portion of the original paper is to be used, and if you are not the senior author, also obtain the senior author's approval.

Requirements to be followed when using an entire IEEE copyrighted paper in a thesis:

1) The following IEEE copyright/ credit notice should be placed prominently in the references: © [year of original publication] IEEE. Reprinted, with permission, from [author names, paper title, IEEE publication title, and month/year of publication]
2) Only the accepted version of an IEEE copyrighted paper can be used when posting the paper or your thesis on-line.
3) In placing the thesis on the author's university website, please display the following message in a prominent place on the website: In reference to IEEE copyrighted material which is used with permission in this thesis, the IEEE does not endorse any of [university/educational entity's name goes here]'s products or services. Internal or personal use of this material is permitted. If interested in reprinting/republishing IEEE copyrighted material for advertising or promotional purposes or for creating new collective works for resale or redistribution, please go to http://www.ieee.org/publications_standards/publications/rights/rights_link.html to learn how to obtain a License from RightsLink.

If applicable, University Microfilms and/or ProQuest Library, or the Archives of Canada may supply single copies of the dissertation.

BACK CLOSE

The permission below is for Chapter 2.

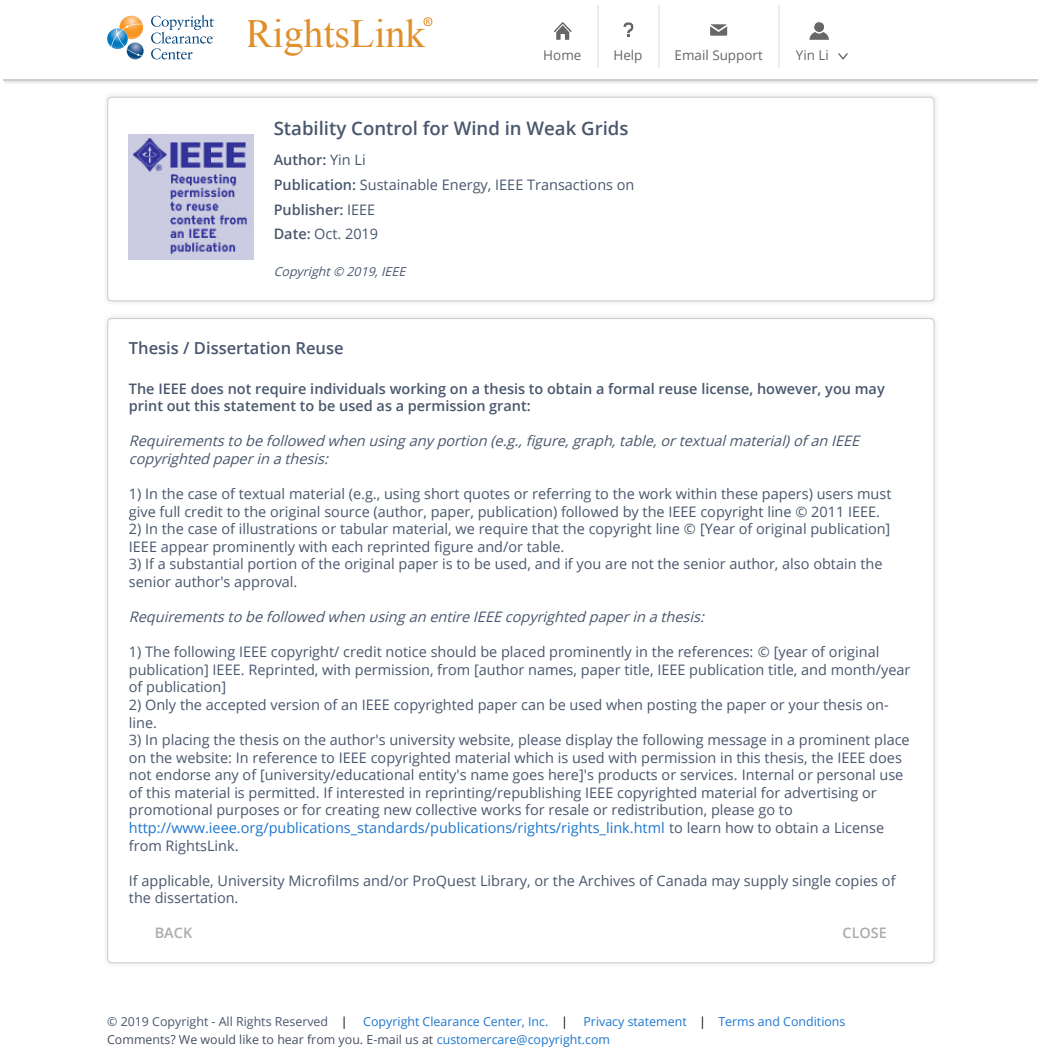

Copyright Clearance Center RightsLink®

Home | Help | Email Support | Yin Li

IEEE Requesting permission to reuse content from an IEEE publication

Stability Control for Wind in Weak Grids

Author: Yin Li
Publication: Sustainable Energy, IEEE Transactions on
Publisher: IEEE
Date: Oct. 2019

Copyright © 2019, IEEE

Thesis / Dissertation Reuse

The IEEE does not require individuals working on a thesis to obtain a formal reuse license, however, you may print out this statement to be used as a permission grant:

Requirements to be followed when using any portion (e.g., figure, graph, table, or textual material) of an IEEE copyrighted paper in a thesis:

1) In the case of textual material (e.g., using short quotes or referring to the work within these papers) users must give full credit to the original source (author, paper, publication) followed by the IEEE copyright line © 2011 IEEE.
2) In the case of illustrations or tabular material, we require that the copyright line © [Year of original publication] IEEE appear prominently with each reprinted figure and/or table.
3) If a substantial portion of the original paper is to be used, and if you are not the senior author, also obtain the senior author's approval.

Requirements to be followed when using an entire IEEE copyrighted paper in a thesis:

1) The following IEEE copyright/ credit notice should be placed prominently in the references: © [year of original publication] IEEE. Reprinted, with permission, from [author names, paper title, IEEE publication title, and month/year of publication]
2) Only the accepted version of an IEEE copyrighted paper can be used when posting the paper or your thesis on-line.
3) In placing the thesis on the author's university website, please display the following message in a prominent place on the website: In reference to IEEE copyrighted material which is used with permission in this thesis, the IEEE does not endorse any of [university/educational entity's name goes here]'s products or services. Internal or personal use of this material is permitted. If interested in reprinting/republishing IEEE copyrighted material for advertising or promotional purposes or for creating new collective works for resale or redistribution, please go to http://www.ieee.org/publications_standards/publications/rights/rights_link.html to learn how to obtain a License from RightsLink.

If applicable, University Microfilms and/or ProQuest Library, or the Archives of Canada may supply single copies of the dissertation.

BACK CLOSE

© 2019 Copyright - All Rights Reserved | Copyright Clearance Center, Inc. | Privacy statement | Terms and Conditions
Comments? We would like to hear from you. E-mail us at customercare@copyright.com

The permission below is for Chapter 2.

Copyright Clearance Center RightsLink®

Home | Help | Email Support | Yin Li

IEEE Requesting permission to reuse content from an IEEE publication

Wind in Weak Grids: Low-Frequency Oscillations, Subsynchronous Oscillations, and Torsional Interactions

Author: Yin Li
Publication: Power Systems, IEEE Transactions on
Publisher: IEEE
Date: Dec 31, 1969

Copyright © 1969, IEEE

Thesis / Dissertation Reuse

The IEEE does not require individuals working on a thesis to obtain a formal reuse license, however, you may print out this statement to be used as a permission grant:

Requirements to be followed when using any portion (e.g., figure, graph, table, or textual material) of an IEEE copyrighted paper in a thesis:

1) In the case of textual material (e.g., using short quotes or referring to the work within these papers) users must give full credit to the original source (author, paper, publication) followed by the IEEE copyright line © 2011 IEEE.
2) In the case of illustrations or tabular material, we require that the copyright line © [Year of original publication] IEEE appear prominently with each reprinted figure and/or table.
3) If a substantial portion of the original paper is to be used, and if you are not the senior author, also obtain the senior author's approval.

Requirements to be followed when using an entire IEEE copyrighted paper in a thesis:

1) The following IEEE copyright/ credit notice should be placed prominently in the references: © [year of original publication] IEEE. Reprinted, with permission, from [author names, paper title, IEEE publication title, and month/year of publication]
2) Only the accepted version of an IEEE copyrighted paper can be used when posting the paper or your thesis on-line.
3) In placing the thesis on the author's university website, please display the following message in a prominent place on the website: In reference to IEEE copyrighted material which is used with permission in this thesis, the IEEE does not endorse any of [university/educational entity's name goes here]'s products or services. Internal or personal use of this material is permitted. If interested in reprinting/republishing IEEE copyrighted material for advertising or promotional purposes or for creating new collective works for resale or redistribution, please go to http://www.ieee.org/publications_standards/publications/rights/rights_link.html to learn how to obtain a License from RightsLink.

If applicable, University Microfilms and/or ProQuest Library, or the Archives of Canada may supply single copies of the dissertation.

BACK CLOSE

The permission below is for Chapter 3.

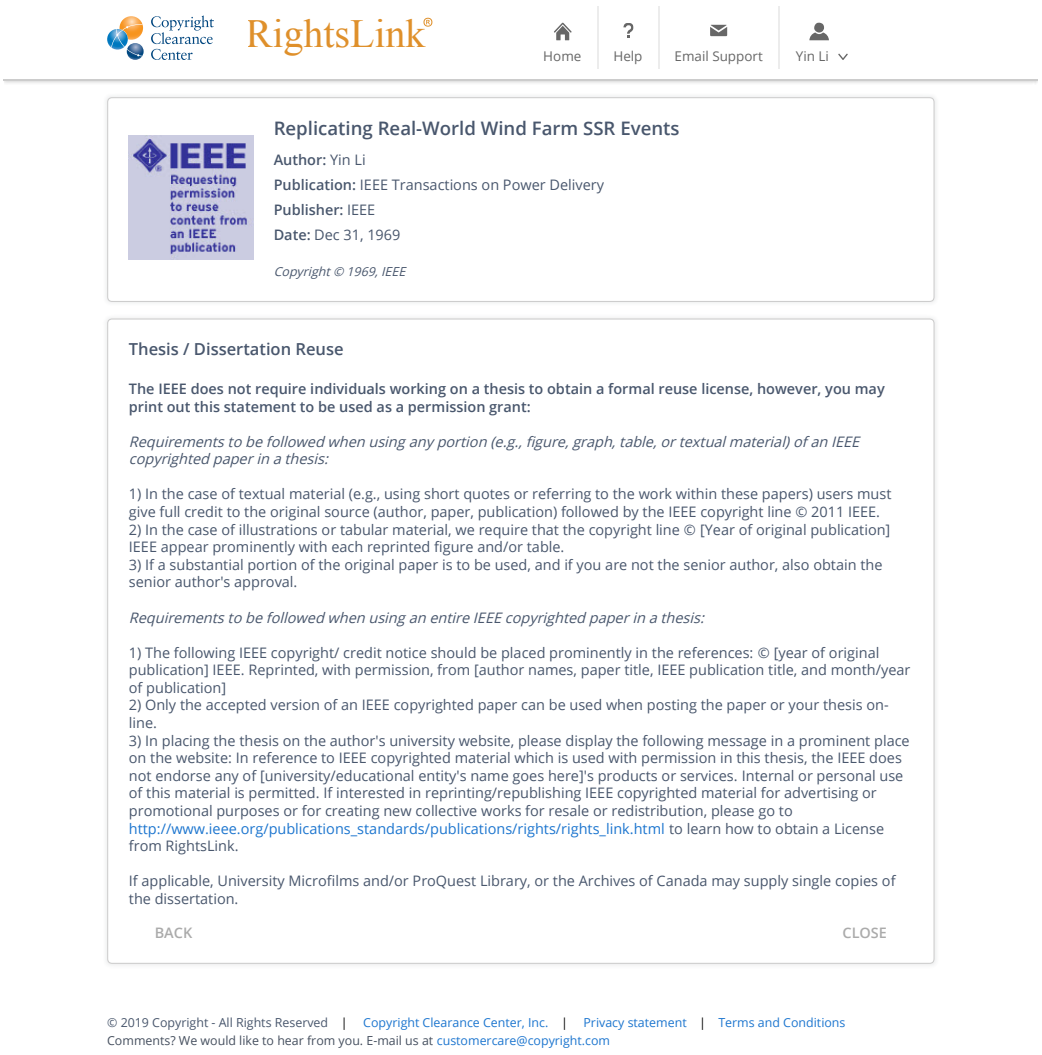

Copyright Clearance Center RightsLink®

Home | Help | Email Support | Yin Li

IEEE Requesting permission to reuse content from an IEEE publication

Replicating Real-World Wind Farm SSR Events

Author: Yin Li
Publication: IEEE Transactions on Power Delivery
Publisher: IEEE
Date: Dec 31, 1969

Copyright © 1969, IEEE

Thesis / Dissertation Reuse

The IEEE does not require individuals working on a thesis to obtain a formal reuse license, however, you may print out this statement to be used as a permission grant:

Requirements to be followed when using any portion (e.g., figure, graph, table, or textual material) of an IEEE copyrighted paper in a thesis:

1) In the case of textual material (e.g., using short quotes or referring to the work within these papers) users must give full credit to the original source (author, paper, publication) followed by the IEEE copyright line © 2011 IEEE.
2) In the case of illustrations or tabular material, we require that the copyright line © [Year of original publication] IEEE appear prominently with each reprinted figure and/or table.
3) If a substantial portion of the original paper is to be used, and if you are not the senior author, also obtain the senior author's approval.

Requirements to be followed when using an entire IEEE copyrighted paper in a thesis:

1) The following IEEE copyright/ credit notice should be placed prominently in the references: © [year of original publication] IEEE. Reprinted, with permission, from [author names, paper title, IEEE publication title, and month/year of publication]
2) Only the accepted version of an IEEE copyrighted paper can be used when posting the paper or your thesis on-line.
3) In placing the thesis on the author's university website, please display the following message in a prominent place on the website: In reference to IEEE copyrighted material which is used with permission in this thesis, the IEEE does not endorse any of [university/educational entity's name goes here]'s products or services. Internal or personal use of this material is permitted. If interested in reprinting/republishing IEEE copyrighted material for advertising or promotional purposes or for creating new collective works for resale or redistribution, please go to http://www.ieee.org/publications_standards/publications/rights/rights_link.html to learn how to obtain a License from RightsLink.

If applicable, University Microfilms and/or ProQuest Library, or the Archives of Canada may supply single copies of the dissertation.

BACK CLOSE

© 2019 Copyright - All Rights Reserved | Copyright Clearance Center, Inc. | Privacy statement | Terms and Conditions
Comments? We would like to hear from you. E-mail us at customercare@copyright.com

The permission below is for Figure 3.11.

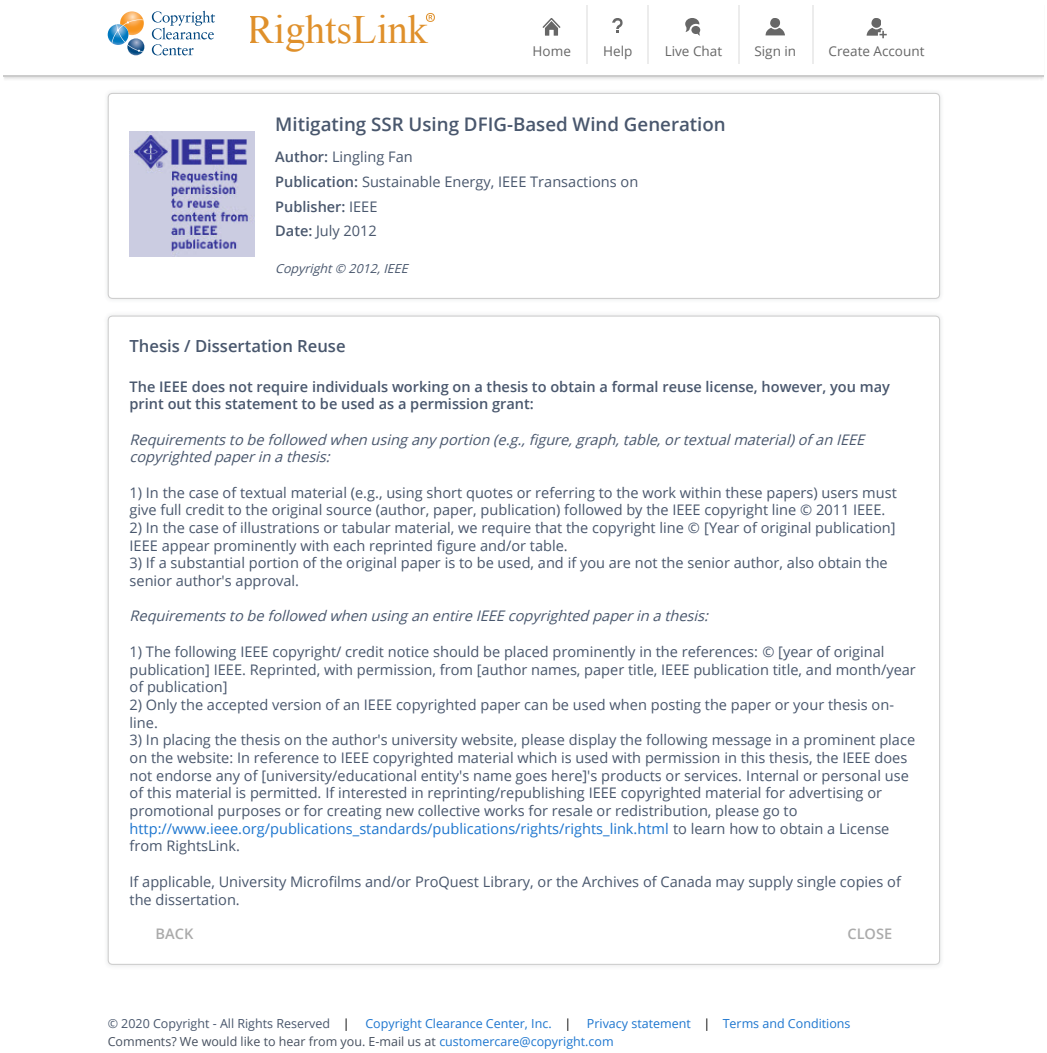

Copyright Clearance Center RightsLink®

Home | Help | Live Chat | Sign in | Create Account

IEEE Requesting permission to reuse content from an IEEE publication

Mitigating SSR Using DFIG-Based Wind Generation

Author: Lingling Fan
Publication: Sustainable Energy, IEEE Transactions on
Publisher: IEEE
Date: July 2012

Copyright © 2012, IEEE

Thesis / Dissertation Reuse

The IEEE does not require individuals working on a thesis to obtain a formal reuse license, however, you may print out this statement to be used as a permission grant:

Requirements to be followed when using any portion (e.g., figure, graph, table, or textual material) of an IEEE copyrighted paper in a thesis:

1) In the case of textual material (e.g., using short quotes or referring to the work within these papers) users must give full credit to the original source (author, paper, publication) followed by the IEEE copyright line © 2011 IEEE.
2) In the case of illustrations or tabular material, we require that the copyright line © [Year of original publication] IEEE appear prominently with each reprinted figure and/or table.
3) If a substantial portion of the original paper is to be used, and if you are not the senior author, also obtain the senior author's approval.

Requirements to be followed when using an entire IEEE copyrighted paper in a thesis:

1) The following IEEE copyright/ credit notice should be placed prominently in the references: © [year of original publication] IEEE. Reprinted, with permission, from [author names, paper title, IEEE publication title, and month/year of publication]
2) Only the accepted version of an IEEE copyrighted paper can be used when posting the paper or your thesis on-line.
3) In placing the thesis on the author's university website, please display the following message in a prominent place on the website: In reference to IEEE copyrighted material which is used with permission in this thesis, the IEEE does not endorse any of [university/educational entity's name goes here]'s products or services. Internal or personal use of this material is permitted. If interested in reprinting/republishing IEEE copyrighted material for advertising or promotional purposes or for creating new collective works for resale or redistribution, please go to http://www.ieee.org/publications_standards/publications/rights/rights_link.html to learn how to obtain a License from RightsLink.

If applicable, University Microfilms and/or ProQuest Library, or the Archives of Canada may supply single copies of the dissertation.

BACK CLOSE

© 2020 Copyright - All Rights Reserved | Copyright Clearance Center, Inc. | Privacy statement | Terms and Conditions
Comments? We would like to hear from you. E-mail us at customercare@copyright.com

The permission below is for Chapter 4.

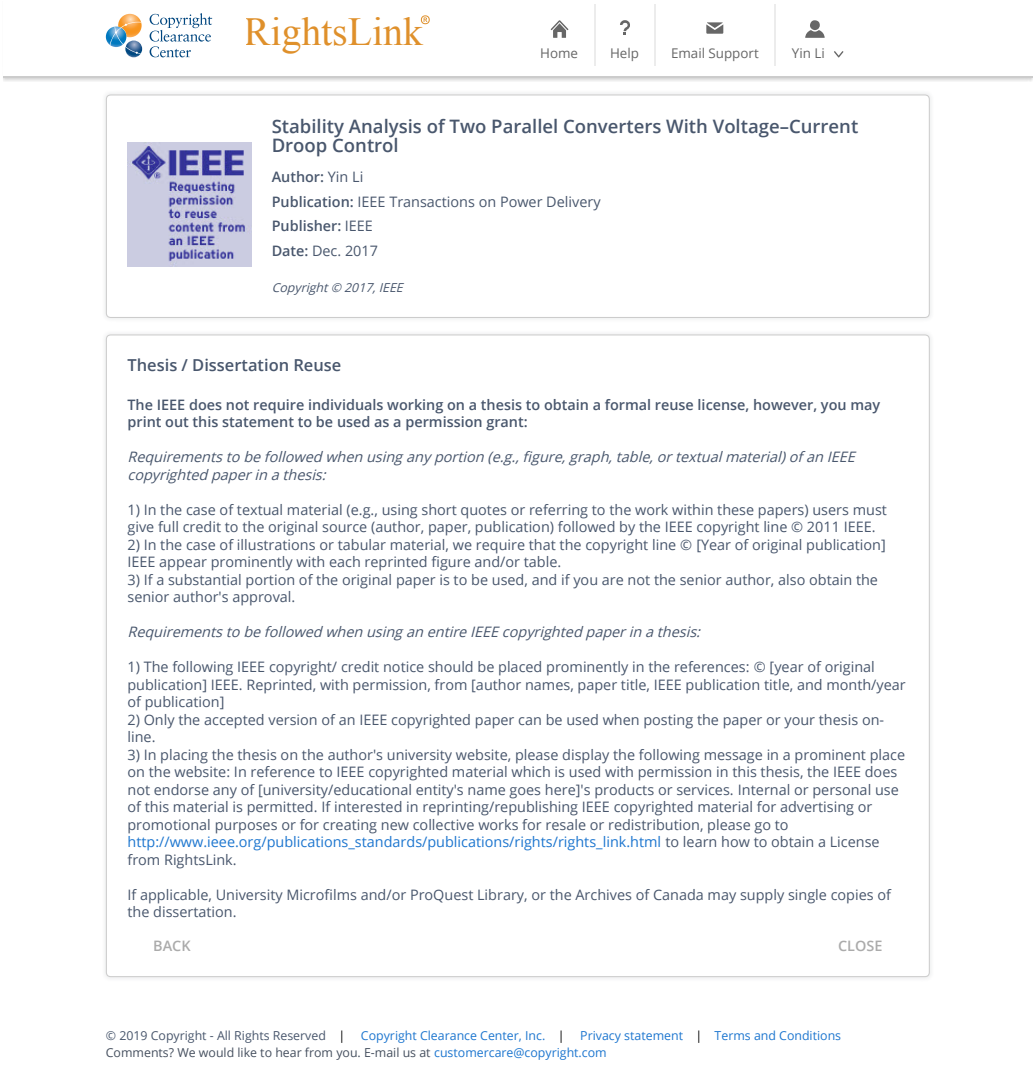

Copyright Clearance Center RightsLink®

Home | Help | Email Support | Yin Li

IEEE Requesting permission to reuse content from an IEEE publication

Stability Analysis of Two Parallel Converters With Voltage–Current Droop Control

Author: Yin Li
Publication: IEEE Transactions on Power Delivery
Publisher: IEEE
Date: Dec. 2017

Copyright © 2017, IEEE

Thesis / Dissertation Reuse

The IEEE does not require individuals working on a thesis to obtain a formal reuse license, however, you may print out this statement to be used as a permission grant:

Requirements to be followed when using any portion (e.g., figure, graph, table, or textual material) of an IEEE copyrighted paper in a thesis:

1) In the case of textual material (e.g., using short quotes or referring to the work within these papers) users must give full credit to the original source (author, paper, publication) followed by the IEEE copyright line © 2011 IEEE.
2) In the case of illustrations or tabular material, we require that the copyright line © [Year of original publication] IEEE appear prominently with each reprinted figure and/or table.
3) If a substantial portion of the original paper is to be used, and if you are not the senior author, also obtain the senior author's approval.

Requirements to be followed when using an entire IEEE copyrighted paper in a thesis:

1) The following IEEE copyright/ credit notice should be placed prominently in the references: © [year of original publication] IEEE. Reprinted, with permission, from [author names, paper title, IEEE publication title, and month/year of publication]
2) Only the accepted version of an IEEE copyrighted paper can be used when posting the paper or your thesis on-line.
3) In placing the thesis on the author's university website, please display the following message in a prominent place on the website: In reference to IEEE copyrighted material which is used with permission in this thesis, the IEEE does not endorse any of [university/educational entity's name goes here]'s products or services. Internal or personal use of this material is permitted. If interested in reprinting/republishing IEEE copyrighted material for advertising or promotional purposes or for creating new collective works for resale or redistribution, please go to http://www.ieee.org/publications_standards/publications/rights/rights_link.html to learn how to obtain a License from RightsLink.

If applicable, University Microfilms and/or ProQuest Library, or the Archives of Canada may supply single copies of the dissertation.

BACK CLOSE

© 2019 Copyright - All Rights Reserved | Copyright Clearance Center, Inc. | Privacy statement | Terms and Conditions
Comments? We would like to hear from you. E-mail us at customercare@copyright.com

About the Author

Yin Li was born in 1990 in Nanjing, China. He obtained his bachelor's degree in Electrical Engineering from the University of South Florida in 2014. He is pursuing his Ph.D. degree in Electrical Engineering from the University of South Florida from Fall 2014. His research interests include dynamic modeling of renewable energy sources, stability analysis, detailed system simulations, and hardware testbed.